Master of Science Thesis

Crashworthiness Design with Bending Optimization in the Hybrid Cellular Automata Framework

A Design Methodology for Aircraft Sub-Floor Structures

A. Bagirov

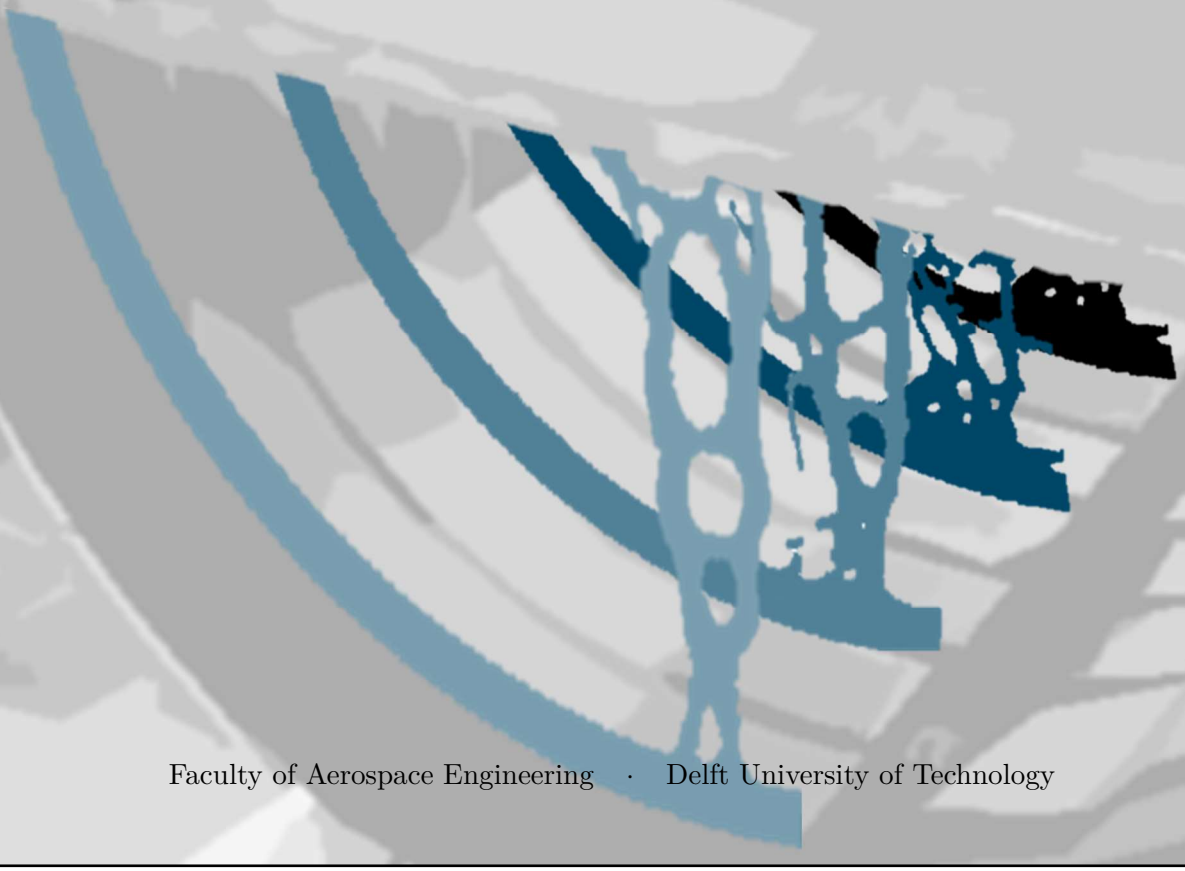

Faculty of Aerospace Engineering · Delft University of Technology

TU Delft Delft University of Technology

Crashworthiness Design with Bending Optimization in the Hybrid Cellular Automata Framework

A Design Methodology for Aircraft Sub-Floor Structures

Master of Science Thesis

For obtaining the degree of Master of Science in Aerospace Engineering
at Delft University of Technology

A. Bagirov

May 27th, 2024

Faculty of Aerospace Engineering · Delft University of Technology

Delft University of Technology
Faculty of Aerospace Engineering
Department of Aerospace Structures and Materials

GRADUATION COMMITTEE

Dated: May 27th, 2024

Chair holder:

Dr. K. Masania

Committee members:

Dr.-Ing. S.G.P. Castro

Prof.dr.ir. M. Langelaar

Abstract

Structural design for unconventional aircraft can be quite challenging and could undergo many iterations until a solution is found for all load-cases such as static sizing, stability and crashworthiness. Ultimately, all of the design aspect are integrated in the earliest design changes for which Topology Optimization (TO) could provide the solution. The Flying-V is one such aircraft with challenging crashworthiness design due to its small sub-floor volume. However, a suitable formulation for aircraft crashworthiness and TO is yet to be found.

This thesis aimed at incorporating the conventional aircraft-crashworthiness characteristic of plastic energy dissipation in plastic hinges in the energy based Hybrid Cellular Automata framework. The HCA principle is to optimize on cellular level, using information of each cell's direct neighbors. For the proposed method, the inter-cell stress and strain information is used to reconstruct the cellular bending energy throughout the non-linear dynamic crash-analysis, providing greater stability than intra-level bending energy. The bending energy formulation was based on the assumption of linearly varying stresses and strains in bending. Several formulations have been formed to manipulate this energy promoting hinge-formation.

The framework has been tested on size optimization of a small-scale slender beam impact model, representing the final design case. Results show peak force reduction and greater displacements compared to the standard HCA crashworthiness model. However, improvements can be made such as inclusion of the non-linear stress and strain variation in the bending energy formulation, to more accurately account for large plastic strain.

Before testing whether the methodology improves the crashworthiness of aircraft, verification of the voxel-mesh approach was required. An A350-like aircraft has been simplified and idealized accordingly and compared with its detailed FEM crash-assessment. Simplifications include modelling only one frame and replacing the cabin and floor with a rigid body to reduce computational cost. Results show good agreement for the required level of detail of conceptual design, although it is recommended to idealize the cabin and floor as well for better agreement. Once verified, the framework has been applied to the entire domain.

Table of Contents

List of Figures

List of Tables

Acknowledgments

This thesis is part of my final efforts in becoming an Aerospace Engineer, marking the end of all the years of studying. In this final stage, my interest in computational mechanics and structural optimization led me towards a collaboration with my supervisor. This thesis subject came in to being through his crashworthiness introduction to our shared interest in unconventional aircraft design. Therefore, in addition to the received guidance, assistance and his well known enthusiasm, I would like to thank Dr.-Ing. S.G.P. Castro

Furthermore, I would like to thank everyone close to me whom had to hear all about the obstacles during this big study.

Delft, University of Technology A. Bagirov
May 27th, 2024

Chapter 1

Introduction

With the aim of cost-effective and sustainable aviation, unconventional aircraft with promising improved efficiencies are thoroughly being explored. Such as the Flying-V promising a reduction of 20% of fuel burn compared to the Airbus A350-900 [17]. However, this unconventional design poses unique challenges, particularly in crashworthiness—a critical aspect that ensures passenger safety during impact scenarios. With the absence of a preliminary design, there are topology optimization (TO) opportunities. However, understanding of appropriate optimization formulations is minimal due to the small amount of research on aircraft crashworthiness and TO [13].

This thesis introduces a new approach to crashworthiness design within the energy based Hybrid Cellular Automata (HCA) framework, incorporating the aircraft plastic hinge characteristic of bending energy absorption. In the HCA framework, communication between neighboring cells is principle in finding the cell's field variable. This framework exploits this transfer of data in computation of the inter-level bending energy, using the inter-cell-level internal forces and deformations. On that scale, the stress and strain functions along neighbors of the non-linear and dynamic crash-analysis are assumed linear.

To conclude on the applicability of the approach to aircraft crashworthiness, several tasks had to be fulfilled. chapter 3 presents the methodology, which includes the derivation of the bending energy, its application in Finite Element Method (FEM), inter-level integration and its efforts to reduce peak forces through function manipulation. Next, the results of a small-scale representative case from literature are presented in chapter 4, including the results of the function manipulation efforts. Finally, the framework has been tested in chapter 5, which also required verification of the voxelmesh approach to aircraft crashworthiness assessment.

Chapter 2

Literature review

To contextualize the thesis work and its relevance to the aerospace industry, a literature study had been performed. The first section presents the motivation and the gap for Topology Optimization (TO) and aircraft crashworthiness. The second section dives into the state-of-the-art of the relevant methods.

2.1 Unconventional aircraft Motivation and Objective

In recent years, unconventional aircraft concepts are being investigated more extensively, aiming at making air-transportation more cost-efficient and sustainable. The Flying-V is one such aircraft, increasing the Lift-drag ratio by eliminating the typical fuselage. Its structural design was found to be challenging which has been presented in this section, followed by the gap of topology optimization in unconventional aircraft structural design.

2.1.1 Unconventional aircraft structural design challenges: Flying-V

The commercial aviation industry has pushed air-transportation to become more cost effective and sustainable. Additionally, this has also been achieved by concerns over environmental impact and pollution. Higher efficiency in engine fuel consumption, structural mass and aerodynamic lift/drag ratio. Throughout these individual design efforts, the aircraft configuration has consistently remained the same: a tube and a set of wings as can be seen in Figure 2.1. Only small changes are made and progress is stalling. Its aerodynamic performance is one aspect that has sought for unconventional design, such as the blended-wing-body. More and more, with technological advances, recent innovations in aircraft design thus move away from the standard.

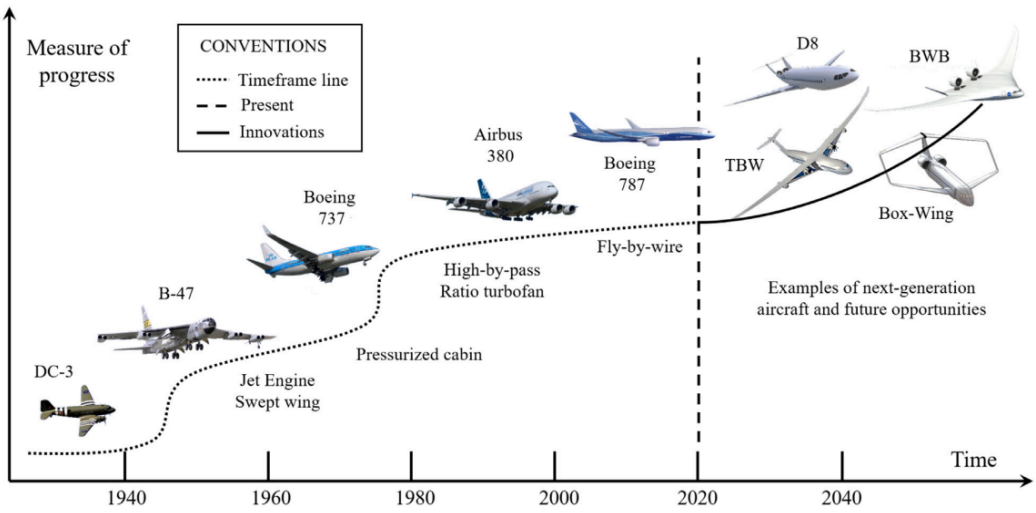

Figure 2.1: Main design changes of commercial airliners in the past and foreseen for the future [1]

One of such innovative unconventional aircraft is the Flying-V, which shows a promising reduction of 20% of fuel burn compared to the Airbus A350-900 following the research by Oosterom [18] on the Flying-V family design [17]. This unconventional aircraft, originally designed by Benad [19] and being developed at TU Delft since 2017 [3], is a flying wing aircraft that eliminates the need of a fuselage tube by accommodating the passengers in the wings. Besides its aerodynamic advantage over the tube-and-wing configuration, it has a structural efficiency gain as the weight and lift are distributed more equally with respect to each other. In other words, less bending moment is developed. This unconventional configuration does bring its own design challenges which need to be overcome. A review of the past design changes and proposals is given in the following paragraphs.

First of all, the oval frames are less efficient in carrying pressurization loads (out-of-plane loading introduced), which initially led to the addition of vertical (LE and TE) and horizontal (ceiling and floor) panels to the Flying-V as demonstrated in 2012 for BWB by Vos [2]. See Figure 2.2. The oval frame is assumed to consist of 3 identical arcs, and out-of-plane loads at the intersections due to pressurization are hereby taken up by these spars/panels. However, this design underwent some design changes in subsequent thesis work.

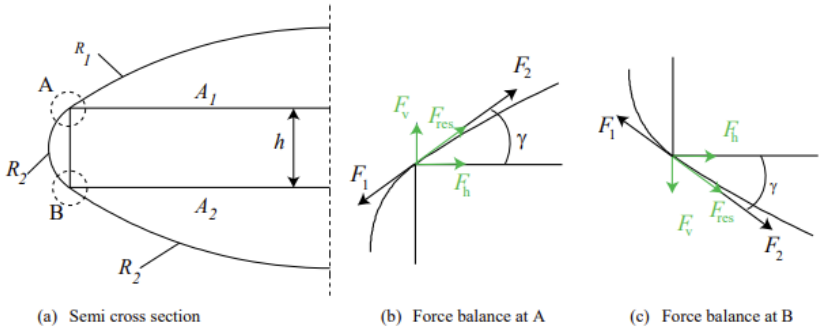

Figure 2.2: To avoid out of plane loads due to pressurization, the frames have been fortified with a LE spar, a TE spar, a floor panel and a ceiling panel [2]

Past thesis work on the Flying-V structural design started off here with van der Schaft (2017) followed by Claeys (2018), whom both used ParaPy Knowledge-Based Engineering (KBE) to generate the mass estimation and preliminary failure analysis' [3, 4]. The primary structure layout was first given by van der Schaft based on existing structures of other flying wing or existing aircraft, with an eye on the expected loads. The lay-out is presented below in Figure 2.3. The frame spacing resembles the rib spacing in wing structures, except for the central section. Some parameters, such as rib spacing, were inserted using data from Airbus. However, no discussion or reference is given on the considered load cases or the applicability to the Flying-V. Additionally, van der Schaft concludes that indeed this lay-out is not optimal, with a reduced bending stiffness in the plane of symmetry (central joint) and high concentrated loads [3]. Moreover, the primary load path runs from the leading edge of the outer wing to the aft spar at the plane of symmetry, whereas a more distributed load path could lower the required mass.

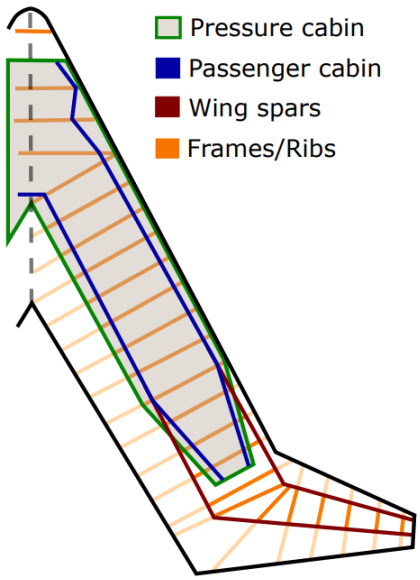

Figure 2.3: The primary lay-out concept for the Flying-V proposed and used by van der Schaft [3]

Claeys [4] imposed some improvements, although surprisingly this non-optimal primary lay-out was left unaltered. In his research, the Flying-V fuselage was found to twist a lot under aerodynamic loads. This resulted in the proposal to add shear walls in the cabin (see Figure 2.4) to reduce the deformation.

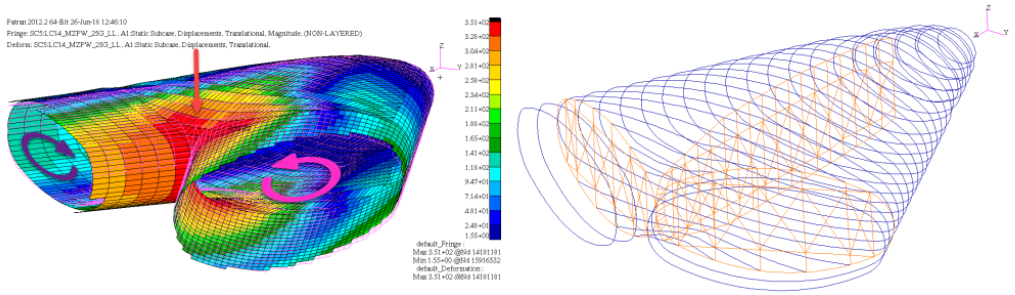

(a) Initial Deformation

(b) Structural Modification

Figure 2.4: Unconventional structure: Flying V central joint deformation and implemented solution. Credits: M.P. Claeys [4]

Successive research by Dotman [5] resulted in a different methodology, by focusing on the design of the constant cross-section fuselage. In this study, the desire to remove the front spar has additionally been investigated, which resulted in only a slight increase of the mass. This concept is called the No Leading Edge Spar concept (NLES), visualized in Figure 2.6 by Voeten [6]. However, with investigating such sections, a lot of simplifications are made and the global performance might be non-optimal. Additionally, the cabin design raised significant doubt due to high sensitivity under small design changes (such as for the ceiling width/spars under angle see Figure 2.5). It has therefore been recommended to perform a general study on the sensitivity of all components, while a general redesign of the non-optimal primary structure lay-out could prove more useful.

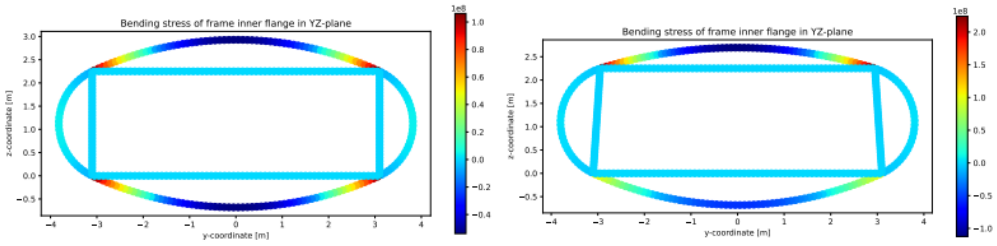

Figure 9.8: Frame inner flange bending stresses for $w_{floor} = w_{ceiling} = 6.2m$.

Figure 9.9: Frame inner flange bending stresses for $w_{floor} = 6.2m, w_{ceiling} = 5.9m$.

Figure 2.5: Constant cabin-cross section studying the stress sensitivity under different ceiling widths by Dotman [5]

Using the same approach as van der Schaft and Claeys, Nanninga developed a fully parametric framework for weight (distribution) estimation of unconventional aircraft [20]. One relevant improvement to earlier work (by van der Schaft and Claeys) is that sizing has been combined with spacing of the components (compared to inputted from reference data), which is a step into full optimization. Buckling was however excluded from the analysis, due to the relatively large computational cost when compared to the linear static analysis. The goal was to more efficiently compare concept designs of unconventional aircraft, such as the NLES option. Unfortunately, the framework has not been expanded to the full Flying-V yet. However, the

conceptual design of the constant cabin-section, as described above, can be improved and the design of the central joint has not even had this assessment yet.

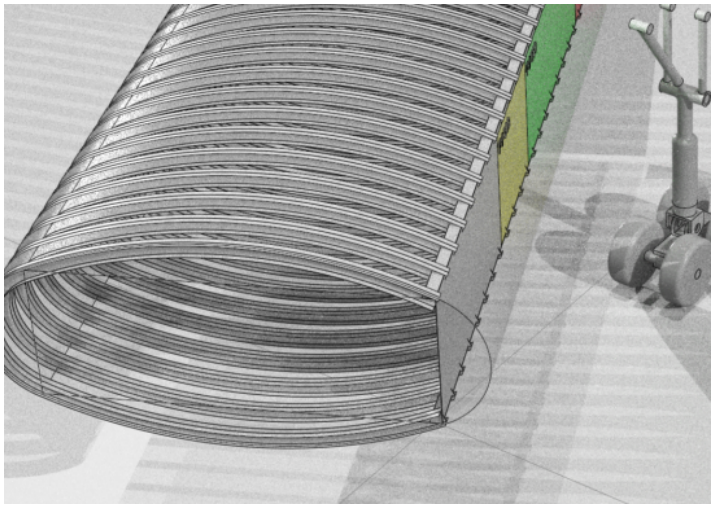

Figure 2.6: Unconventional structure: Flying-V oval fuselage impression without a leading edge spar (the floor and ceiling have not been shown in the image). Credits: R. Voeten [6]

The current primary structural-configuration of the Flying-V can be seen in the figure below (Figure 2.7. It is based on the NLES concept with only the aft spar and the design proposal by Claeys [4] of the 3 additional primary shear walls/frames. Voeten [6] used the aft-spar to mount the engines.

All of the above made structural design choices happened sequentially and the global optimally can be challenged. Additionally, a different approach could be taken to also accommodate for other design objectives such as aero-elasticity or crashworthiness. The latter will be discussed in the next sections. Some other design challenges are the detailed design of the central joint, the integration of cut-outs for doors and integration of the floor and ceiling into the aft spar and/or frames. Furthermore, the transition of the oval fuselage frames into the nose cabin can be determined more specifically as well, challenging the lay-out proposed by van der Schaft [3] (see Figure 2.3).

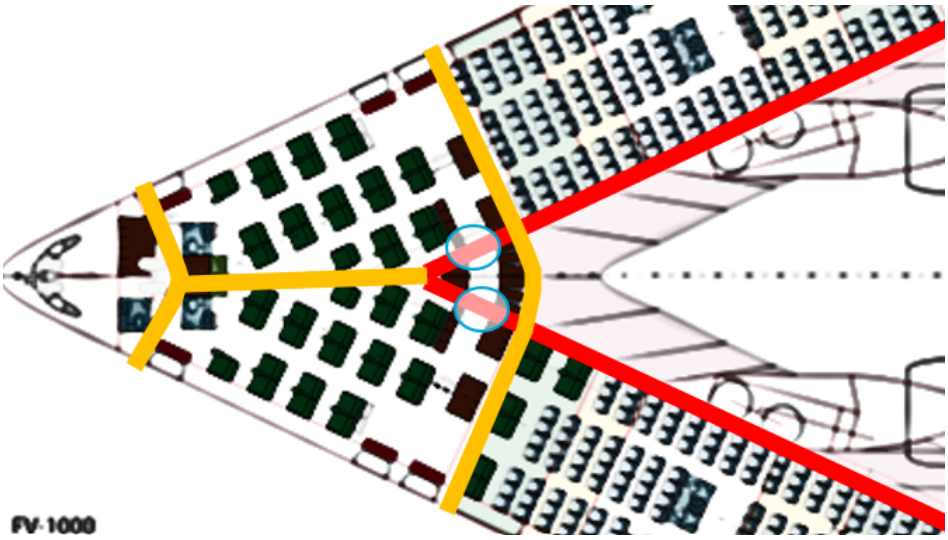

Figure 2.7: Unconventional structure: Flying V nose cabin structural layout with the central joint. The orthogrid aft-spar has been shown in red. The addition of Claeys' design change (Figure 2.4) has been shown in yellow.

2.1.2 Conceptual Structural Design Optimization and Topology Optimization

Aircraft design is an iterative process composed of the interaction between aerodynamics, structures, propulsion and manufacturing. The structures with its manufacturing technique are designed to carry the loads of the other disciplines, which are sized depending on the mass estimate (distribution). This mass and stiffness distribution affects the aircraft performance and the loop continues. For conventional aircraft, old designs and data can be used for the mass estimations used in design feasibility studies, even making use of empirical formulas.

For unconventional aircraft, this data is limited or absent. Additionally, the inherent structural layout does not deviate much for conventional aircraft whereas unconventional aircraft could produce drastically different geometries and mass distribution, adding also to uncertainty in stability behaviour. The Flying-V [19] is a prime example. The benefits this concept brings has to outweigh the risk associated with the lack in data and/or uncertainty in mass and stability behaviour [1]. Recent work in the Flying-V have all performed mass estimation through FEA sizing [3, 4, 20], with the (potential) inclusion of stability, stress, stiffness and fatigue. In general, progress in high-performance computing and finite element analysis has helped swift the use of high-fidelity modelling towards the conceptual phase [1], with the aim to reduce the associated risks in later stages of (structural) design. Topics that are typically investigated at later stages are for example damage tolerance and crashworthiness, since only marginal changes are made to conventional aircraft.

From the above study, it is clear that aircraft design is moving towards full consideration of all design objectives in the early design phases. The weight estimation in these early phases rely on empirical relations for conventional aircraft, and when this is absent, FEA with KBE provide the solution [3, 4, 20]. However, as for the Flying-V [3], initial lay-out of the primary structures are being designed based on reference aircraft or engineering judgement, while these can turn out to not be ideal. These lay-out are then optimized for size or shape.

Ultimately, size and shape optimization are applied for the most efficient structural lay-out. To find this optimal lay-out, the identified and proposed method is to use topology optimization (TO). With complete freedom, this method should be able to find the most efficient distribution of mass during conceptual structural design. The resultant TO solution can then give valuable insight, which can be interpreted into a manufacturable design.

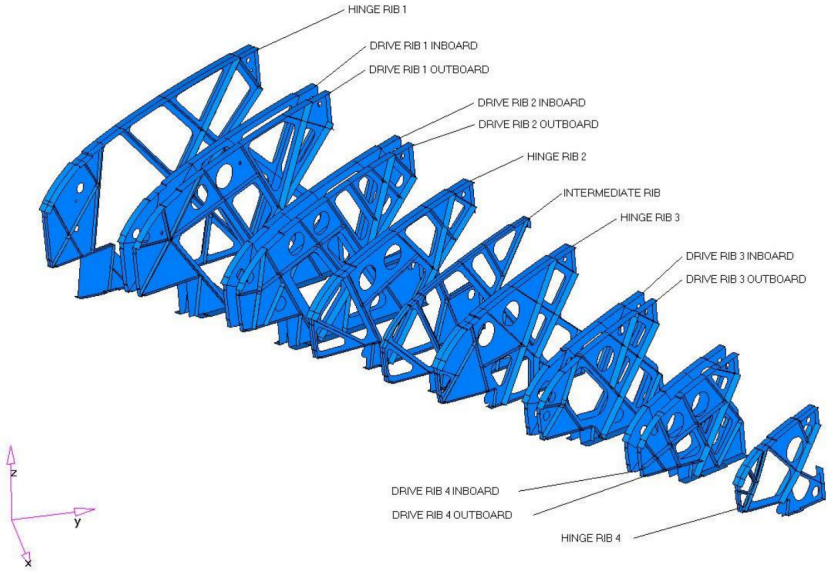

Figure 2.8: TO applied to the LE rib design of the A380 [7]

Topology Optimization has already been applied in the structural design for a wide range of aircraft components, such as brackets, engine pylons, door frames and more [21]. One of the most famous examples is the design of the wing ribs of the A380 [7]. In this example, a total of 13 droop LE edge ribs had been optimized and translated into real products, see Figure 2.8. However, work on large-scale topology optimization is limited. Mainly since the conventional aircraft is reliable and does not require any change. Large scale topology optimization is therefore more applicable to unconventional aircraft. The same proposal has thus been found for the blended wing body (BWB) concept [8]. With minimum compliance as the objective and 3 critical load cases, yielding 3 different topology solutions. The design interpretation result can be seen below and does show an unconventional lay-out in Figure 2.9. Although the level of detail could have been better and the proper penalization could yield more a more distinct design (see **??** for more information). More importantly for the example [8], buckling and stress constraints are not imposed yet, while stability of TO solutions is quite a concern due to the outputted slender solutions and stability is of major importance for aircraft. Although Singh et al. (2016) [8] explains stability is tackled in later stages, it could be useful to include it as early as possible and thus add this (and stress constraints) to the TO process to avoid costly redesign.

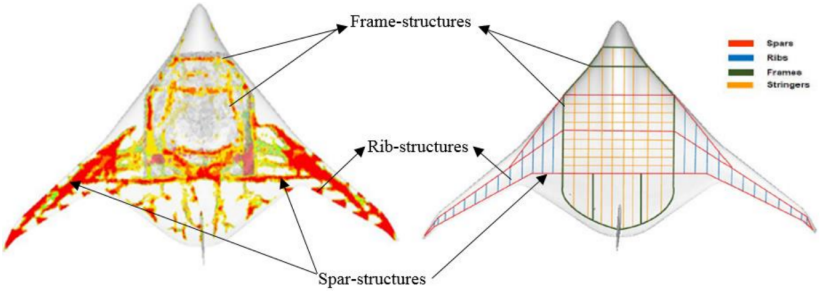

Figure 2.9: TO novel unconventional concept BWB and interpreted to a manufacturable design [8]

2.1.3 Aircraft Crashworthiness and Topology Optimization

Crashworthiness poses a risk for unconventional aircraft as is noticeable for the Flying-V, with its smaller volume beneath the cabin floor compared to conventional aircraft. The smaller volume can result in more impact energy propagating into the cabin in the case of emergency landing. On top of that, new designs require at least the same safety standards concerning for example emergency landings [22], where regulations are set for certification by EASA CS-25 for civil aircraft [23]. For conventional aircraft, aircraft airworthiness is typically tested using for example drop tests. However, due to high cost and preparation time, simulations are introduced for preliminary assessment [9]. Such as for the A340, which has been validated using the test of the A320. In this analysis for conventional aircraft, the material and connection failure are the dominant failure types [9]. Two main modes of failure have been identified in the literature, namely unrolling and flattening. The bending and formation of plastic hinges in the frame absorb the majority of the crash energy, through destruction by zones (which can be seen in Figure 2.10).

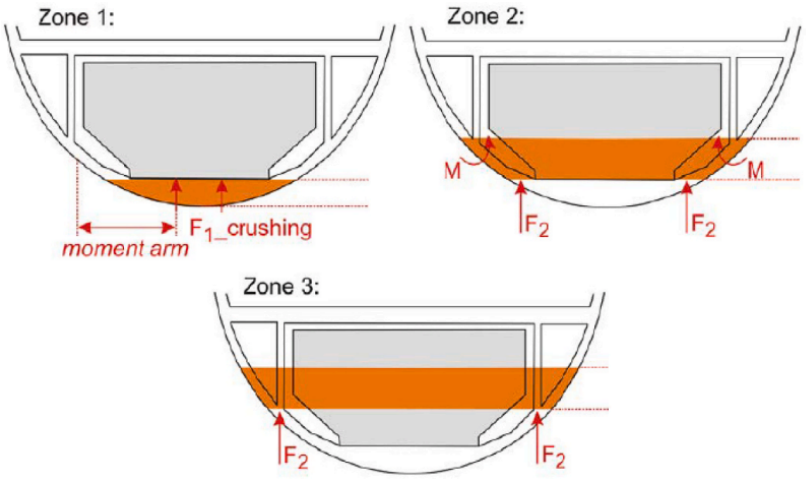

Figure 2.10: energy absorption zones for conventional structures absorbing the majority of the crash energy through rotation of the frames [9], Figure credits: [10]

One such detailed crashworthiness assessment has been performed by Gransden and Alderli-

esten [11], developing a finite element model to compare the drop-test behaviour of metal and composite fuselage sections. Although the assessment has been made on existing sections to compare materials, the paper's A320 model validation concerning hinge formation and overall energy absorption capabilities of a FEM model is. For the A320, the deformation is governed by the frame-struts cross-section making the response appear 2D. The damage is focused in the 'pinch' behaviour at A, and the plastic hinges at B and C (see Figure 2.11 for the numbering). The hinge at location C was identified as critical in decreasing the accelerations experienced by the occupants at floor level. One key difference was that the separation of the cargo floor at the pinch A (through rivet failure following shearing of the brackets) from the experiment was absent in the model. In terms of accelerations, it has been concluded that the overall width, magnitude and duration of the accelerations show good agreement considering variations in accelerometer locations [11]. The same crash-response of drop-test experiment can thus to some extent be achieved by finite element models for existing conventional-aircraft. Sub-floor designs can be optimized using FEM models by making sections more compliant or stiffer to tailor the crash-response.

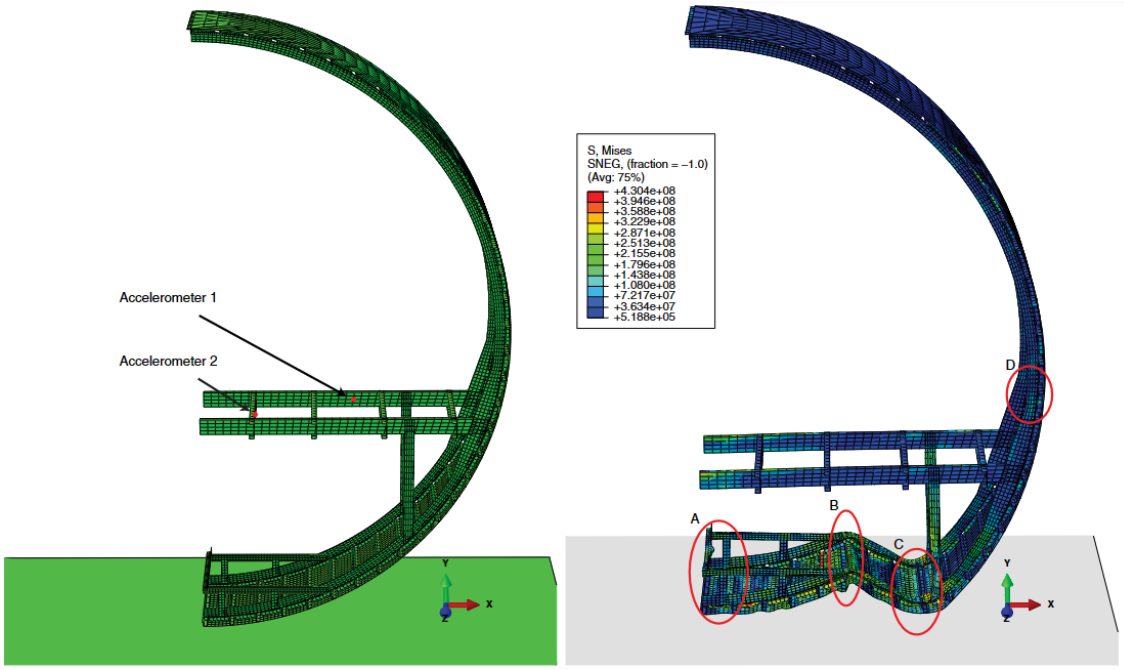

Figure 2.11: A320 two frame FEM model and peak Von-Mises result [11]

For the Flying-V, there is no existing structure and its sub-floor space has less volume available for energy absorption mechanisms due to its oval shape, seen in Figure 2.12. Desiderio [12] was the first to address the uncertainty in crashworthiness structural mass for the unconventional Flying-V by means of FEA crash simulations on the designed fuselage section by Dotman [5]. A significant portion of the aircraft did not have a preliminary structural design and as a result, the performed assessment was limited to the designed typical section. One interesting finding was that Desiderio's objective was extremely sensitive to the already designed (for static loading) frame height. This proves the importance of earlier inclusion of crashworthiness. Above all of these challenges, it is not known whether the crash-response of the typical section

is representative for the full aircraft, due to its sweep with respect to the crash-direction or the large inertial forces of its surrounding structures or engines.

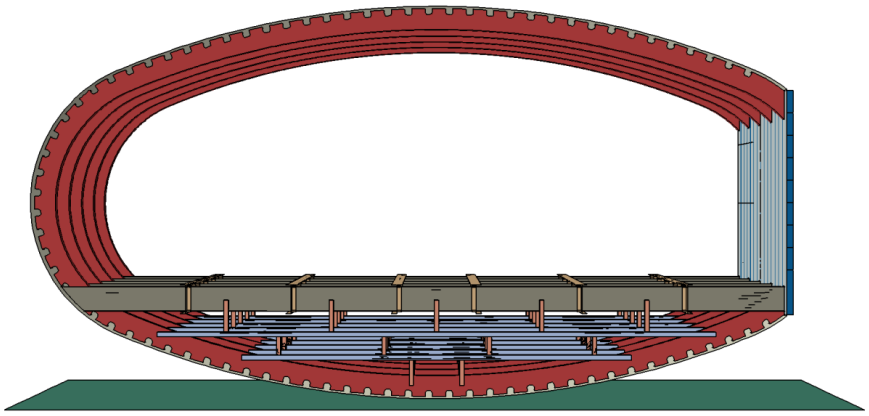

Figure 2.12: One of the sub-floor crash-structure configurations by Desiderio [12]

Nevertheless, Desiderio had to come up with new sub-floor crash configurations for the oval shape of the Flying-V typical section, where the options are infinite in strut positions, orientations, quantities and dimensions. One such unconventional structure has been presented in Figure 2.12. These configurations should absorb most of the energy where plastic hinges ultimately are to be formed. For all of the concepts, plastic hinges hardly formed along the frame. For that reason, the study shifted towards energy absorption through plastic bending of the sub-floor structure itself with the addition of many-sub-floor section, as seen in Figure 2.12. For unconventional aircraft, such as the Flying-V, there is thus a desire to include crashworthiness earlier in the process by means of high-fidelity modelling as well. Performing crashworthiness assessment earlier in the preliminary design (through simulations) can help avoid costly and time-consuming redesign [22, 24].

With infinite possibilities, topology optimization could be used to find the conceptual mass-distribution that would result in plastic bending. However, there is limited research on aircraft crashworthiness TO (except for the study on crush-able lattice structures [25]), with limited insight in suitable optimization formulations as a result [13]. Das et al. very recently, in 2023, introduced gradient-based topology optimization with for aircraft sub-floor structure [13]. In their work, the objective was to minimize the acceleration, by discretizing the continuous non-linear response and calculating the gradients analytically of a acceleration function. Although the framework proved effective, the computation of derivatives remains costly and sensitive to errors, to which their tested design domain consisted of a few number of elements, visible in Figure 2.13.

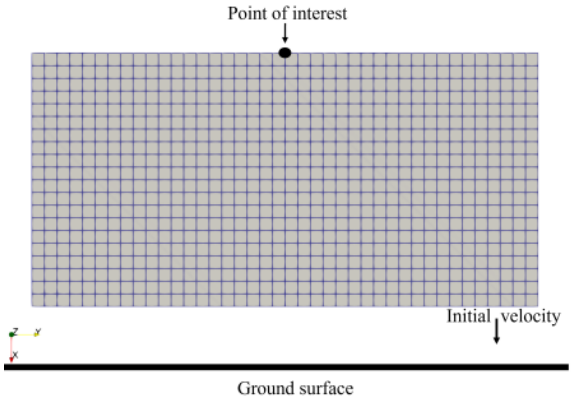

(a) Baseline domain with initial conditions.

(b) Optimal material distribution with $vf < 0.3$

Figure 2.13: Design domain and solution to gradient-based SIMP TO for crash-acceleration minimization [13]

Therefore, literature on crashworthiness typically computes the gradients on simplified responses (Equivalent Static Load, ESL) or even avoids the use of gradient-based optimization at all, relying on heuristic approaches or the Hybrid Cellular Automata approach. More on these in the topology optimization section. A suitable optimization formulation for aircraft crashworthiness is thus yet to be found.

2.1.4 Research Objective

To conclude, the Flying-V is still in a very early preliminary stage with many aspects untouched such as its critical region the central joint. The structural design for the Flying-V presented above (and possibly other unconventional aircraft) resulted in unconventional design choices spanning and affecting different projects over time. Additionally, a detailed crash-assessment in this early phase of the Flying-V has been found challenging, where many design choices still need to be made. Topology optimization could be used in the conceptual structural design to give insight in the configuration's most efficient distribution of structural

mass for all load-cased, ultimately including a crashworthiness assessment. Early inclusion of crashworthiness, for aircraft in general, has the potential to avoid costly redesign in later stages or even termination.

With the absence of an efficient approach and optimization formulation for aircraft crashworthiness, this thesis aims at bringing topology optimization and aircraft crashworthiness together as the first step towards a full-scale aircraft TO. Since aircraft crash-responses greatly benefit from the formation of plastic hinges, it shall be included in the **research objective**:

To achieve aircraft crash topology optimization by developing a TO method which includes plastic hinge formation

To achieve energy-absorbing plastic hinges in TO, energy-based methods and formulations could prove useful and is included in the following study.

2.2 Topology Optimization and Crashworthiness

It has been found in the literature study above that, for aircraft in early design stages, the conventional structural designs might be non-optimal in static and crashworthiness sizing. Such as for the Flying-V, where the unconventional oval fuselage required the unconventional design choices presented in subsection 2.1.1 and where the space below deck is limited for crash energy absorption. To make the most efficient use of any design space such as this unconventional belly, there is a need for TO and aircraft crashworthiness.

Crash responses are highly non-linear, for which the traditional optimization technique using static load is not viable anymore. Gradient based TO contains numerical noise on the gradient information of non-linear analysis [26,27]. Additionally, the cost of computing the sensitivities of frame in the dynamic response can be too high [28]. Alternatively, there is the Equivalent Static Load approach, which simplifies the full non-linear response to be used for linear static optimization. Simplification of the displacement field can strain away too far from reality. Therefore, gradient-free approaches are more suitable, such as genetic algorithms (i.e. Evolutionary Algorithms), and converge to global optimum. However, the cost rises exponentially with up-scaling. Other state-of-the art on the combination of continuum-based TO and crashworthiness involves the heuristic approach of HCA. Both ESL and HCA have been investigated and presented in this section.

2.2.1 Topology Optimization Background

In topology optimization, the material distribution is optimized under given objectives, constraints, loads and boundary conditions [21]. The main difference it has compared to shape or size optimization is that no initial design is needed.

Topology optimization has known many forms, where the focus for this study lies only on the approaches that are independent of initial choices. One of the unwanted approaches is for example the ground structure approach, in which positions of nodes are inputted and the goal is to find the optimum truss layout in this design space. This study thus focuses on

continuum based TO, that starts with a voxel-based block of material representing the design space. The relevant methods can be grouped into three groups, hard-kill methods, boundary variation method and the gradient-based method [29].

A common hard-kill method is called Evolutionary Structural optimization (ESO), which differentiates the presence of an element as fully present or fully absent (0 or 1) based on removing inefficient material using heuristic criteria [30] (for example low von-misses stress). This method received some criticism, since element removal could also lead to failure of the design. So a variation is the bi-directional ESO, in which material is allowed to be re-introduced. However, this heuristic approach could lead to local-optima dependent on the initial lay-out and has not proof of optimality. One benefit is that the solution is referred to as a black-white design, meaning no grey elements are present and thus no post-processing or filtering is needed, compared to gradient based optimization.

The most recent developed method is the level-set based method, which makes use of functions to represent the design domain (compared to explicit parameterization) in optimization, such that again a black-white solution is obtained but then with sharp and smooth edges [29]. The analysis is still performed using finite elements, requiring translation of the domain. In optimization, voids are added/removed/merged and translated by adjusting the functions using its shape derivatives (which can be considered a modified gradient approach).

The most widely used topology optimization method is the solid isotropic material with penalty method (SIMP) [21]. In this method, a density value between 0 and 1 is assigned to isotropic element material to gradually remove the material by removing its stiffness. The intermediate densities allow for continuity calculations but should be pushed towards void or solid in the final solution. This is achieved by using a penalization scheme [29], interpolating the material properties at specific penalization rates to reach convergence faster. Continuation strategies that vary the penalization scheme throughout optimization can be used to avoid reaching a local but rather a global optima [29].

The SIMP method does have three drawbacks, namely checkerboarding, mesh-dependency and low-density regions, which have been mitigated through different approaches throughout the years. The phenomenon of checker-boarding (which is also present in the discrete element approach of ESO/BESO), where voids occur in-between solid elements resembling a checkerboard. These regions are physically meaningless and result in faulty stiffness. Different filtering schemes exist, which alleviate the issue by essentially using a 'blur' filter on the densities (or sensitivities) [29]. The current most widely used filter is the PDE-filter. Mesh-dependency algorithms, which impose a minimum length scale, also solve the checkerboarding issue [29].

For non-linear analysis, low-density regions can cause convergence issues (or even divergence) [31]. The low density regions obtain negative tangent stiffness matrices causing unnatural mesh distortion. This mesh distortion can be avoided by means of a threshold filter chosen for the design variables volumes. After the nonlinear (NL) analysis, the FE model before filtering is used for the next linear TO cycle. Selection of threshold magnitudes is extremely important, and it has been reported that, whereas large thresholds help in accelerating convergence, too large thresholds result in unwanted 'checkerboard' patterns. However, more recent work on TO has utilized different filtering schemes exist where my preference in checkerboard solving lies in 'blurring' or averaging the densities, due to its ease of usage. Avoiding mesh-distortion can also be achieved by imposing a minimum density, which is the most stable (with the least

amount of discontinuities) but over-estimates the stiffness. An unconventional approach, by Behrou et al. (2021) [32], has been found that even deletes low density elements and their respective DOF from the system. Boundary conditions then need to be imposed on the surrounding elements. Some other approaches include heaviside projection and penalization.

2.2.2 Equivalent Static Load (ESL) approach

Crashworthiness analysis in TO can be solved by means of the linear static formulation of equivalent static load (ESL). The non-linear response is computed to get the non-linear displacement field of the system. Inputting these displacements back into the linear static system yields the equivalent static load force vector. This vector from the outer loop can then be used for the optimization in the inner loop as a load case.

Lee and Park (2015) [31] discuss the challenge of the dynamic non-linear dynamic analysis in the ESL method. For a dynamic response, the optimizer should find a TO solution for the entire response. In the ESL method, each time-step has its own ESL vector and more than one can thus be of importance. Typically, the individual time-step compliance's are summed, yielding a topology with minimum compliance but possibly peaks on local level [31]. Their proposal is to only consider the time increments with the highest internal work and the increments surrounding these peak(s). By this approach, they hope to reduce the average and achieve a more evenly distributed compliance, or in other words, a stiff topology for all increments. Other work proposes performing a design of experiments (DOE) on the weights of each increment compliance [33] to gain insights in the behaviour.

To pick the peaks only (or even weighted with the neighbouring increments) has the potential to exaggerate the loads for large (bending/plastic) deformations, because the ESL formulation will find a solution to conform these deformations while neglecting the load history. Moreover, numerical instabilities can cause termination of the optimizer since the linear static range assumption is exceeded [34]. Another approah, by Bai et al. (2019) [34] is to scale the ESL's using energy ratio. The strain energy for the peak time increment is then taken and compared to the computed ESL strain energy (computed with the deformations and the linear stiffness matrix). The paper argues when the dynamic (for the peak) strain energy is 30% of the computed static strain energy, the energy scaling method has to be applied and from 70% on-wards the standard ESL loads are still applicable.

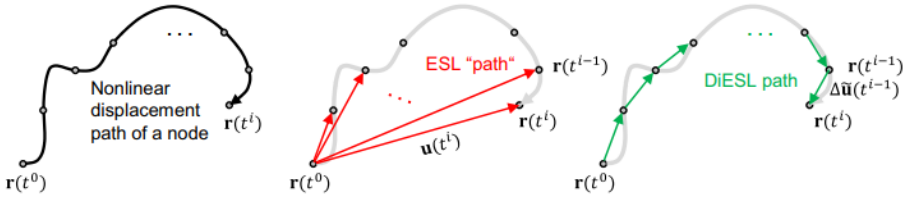

Figure 2.14: The principal method of DiESL, following the deformations [14]

The current state-of-art for dynamic nonlinear TO has been identified as the work done presented in 2022 by Triller et al. [14]. In their work, they successfully applied the method of difference-based ESL (DiESL) to TO, to overcome the challenge of exaggerated loads

(similar to [34]). The method splits the non-linear response into subdomains and stores the deformation fields. The incremental/relative displacement fields can then easily be calculated, which are then used as the 'undeformed' matrices. Each increment will thus have its own ESL based on the intermediate time increment. A schematic showing the sampling can be seen in Figure 2.14. The ESL then are more meaningful and do not have the risk of exaggerated magnitudes explained above. Additionally, they have shown that standard ESL solutions are harder to interpret and 'neglect' inertial effects, in contrast with DiESL. Different to standard ESL multi-load approach (where loads are weighted, the undeformed matrices differ and so different FEM models are needed for optimization. This has been solved by utilizing multi-model optimization within optistruct. Another limitation of ESL is that the stiffness matrix assumes linear elasticity, whereas plasticity can occur. As a result, the proposal consists of updating the elemental stiffnesses due to strain hardening to get more accurate stresses and stiffness representation.

Although the Di-ESL method is able to overcome most of the issues associated with the ESL method, its applicability to aircraft is questionable. The high degree of material and geometrical non-linearities would require careful selection of (and the number of) the subdomains. Especially since we desire a large degree of plastic deformation. Besides, computation of the sensitivities remains high.

2.2.3 Hybrid Cellular Automata (HCA) approach

Patel et al. [35] introduced the HCA approach to crashworthiness for continuum based TO. The cellular automata is a bio-inspired methodology where, for a grid of cells, each individual cell uses only information from its surrounding elements to determine its own state change based on a set of rules. 'Hybrid' refers to the combination of this methodology with the global response of a structural analysis' using FEM (as opposed to the neighbouring cells). When the HCA method is applied in density based TO, each element's state holds information of its density and its field variable. The field variable is decided upon for the objective and the HCA approach strives for uniformity of the field variable. An example of the field variable is the strain energy density, which is taken from the neighbors and used to determine the center element's state based on rules concerning the field variable set-point. Typically, the average value of the surrounding responses are taken as the state and the set-point could be the average value of the entire domain. Several neighborhood definitions exist in the literature (see Figure 2.15 for a 2D example) where the most common is the von Neumann, here only the elements directly adjacent are considered for each element. However, its small size could be a source for instability, when extreme local responses cause significant jumps in density changes (leading to oscilation) or checkerboarding. Too large neighborhoods have the disadvantage that detail is lost. Fortunately, the neighborhood configurations are also used to fix checkerboarding as the density is averaged, similar to a filter in SIMP TO.

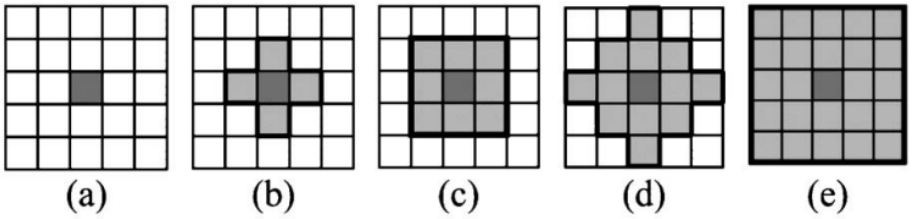

Figure 2.15: CA neighborhood definitions: (a) Empty, (b) von Neumann, (c) Moore, (d) radial, (e) extended [15]

Patel et al. [35] assumes a crashworthy design is one in which deformation is minimized and the whole structure contributes to the energy absorption, requiring uniform distribution of plastic strain. Since not every element might show plasticity, the internal energy density is commonly used as field variable. Aullig et al. [27] also use this assumption and required uniform distribution of the total energy (including strain energy for static loads). Material density then moves proportionally to its offset with neighboring elements. Uniform internal energy for crashworthiness can however unnecessarily make the entire domain stiff. Whereas for aircraft, most absorption needs to occur beneath the floor.

In this belief, Bandi et al. (2013) [16] developed the method of 'controlled energy absorption'. Here, the domain is split at predefined 'output ports' (see Figure 2.16) in a stiff domain and a flexible domain, where the IED and Mutual Potential Energy (MPE) are optimized respectively. The MPE is the work done by a so called dummy load, by using its stress field with the actual impact strain field output. The objective is to maximize the mutual potential energy for a compliant design in the flexible domain only, while driving the IED to uniformity in the stiff domain. This 'non-existent' load has a specified location with a specified (preferred deformation) direction. Splitting the domain and deciding on the deformation direction requires too much user input. This energy is therefore not ideal.

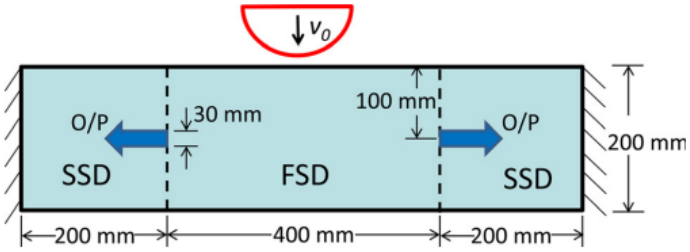

Figure 2.16: A 2D beam under impact split in a compliant flexible subdomain (FSD) and a stiff subdomain (SSD) [16]. The dummy loads are imposed to compute the work done (MPE) by the FSD under the impact load. The SSD and FSD should obtain uniformity in internal energy distribution and MPE respectively.

One advantage of the HCA over ESL is that the static and dynamic non-linear optimization are more compatible since both cases can be expressed in energies. The research by Aullig et al. [27] is one example where this has been conducted to find a multi-objective optimum. In their research, the strain energy from static sizing with the internal energy from crash scenarios

were summed with weights. This total energy is then sought to be uniformly distributed. One issue is that static design only concerns one single equilibrium position while crash scenarios are dynamic and thus time-variant. Typically, in this case, the time-increment at maximum total internal energy is taken for optimization [27]. HCA is then applied to distribute this accumulated and weighted sum.

An improved method by Afrousheh et al. [36] has been dedicated to plastic strain distribution for maximum energy absorption and peak load constraint, including setting a allowable strain limit to avoid rupture. Additionally, the entire collision time history is used (to compute the plastic strain), compared to the peak energy increment explained for the ESL.

Nevertheless, the HCA approach is familiar with the large non-linearity involved in aircraft crash-scenario (and thus the high energy absorption involved) and could therefore still be very useful in forming a TO method for aircraft crashworthiness alone (compared to the gradient-based approach of the elastic ESL method). Buckling could be tackled in further studies.

de-facto hinges

Chapter 3

Methodology

With the objective to achieve aircraft crash topology optimization, the energy-based topology optimization method of Hybrid Cellular Automata (HCA) is aimed to incorporate plastic hinge characteristics that can lead to their formation. This chapter outlines the methodological framework designed to achieve this goal. First, the fundamentals of topology optimization and the HCA approach is presented. This is followed by the the proposed bending energy definition and its integration into the Cellular Automata framework. Finally, the validation strategy with the test-case called 'proof-of-concept' is presented. This proof-of-concept showcased the need for a new energy-based HCA framework in chapter 5.

3.1 Hypothesis and Research Questions

Does bending optimization in HCA allow plastic hinge formation in topology optimization (TO) to improve the crashworthiness of aircraft?

To answer the hypothesis above, the following three research questions have been composed.

1. **RQ1. How can detailed FEM aircraft crashworthiness assessment reliably be approximated by voxel-mesh models?**
   In the literature study, it has been found that traditional absorption mechanisms, such as frame folding, cannot easily be enforced in structural design. A alternative aim has been developed by Desiderio [12] to introduce hinges in the sub-floor structure itself. With infinite design possibilities, topology optimization has been proposed in this thesis. However, how consistent are voxelmesh elements with detailed aircraft crash analysis?

2. **RQ2. What is the effect of inter-level based bending energy on crashworthiness TO using the HCA?**
   Bending of the frame and the associated plastic hinges have been the inspiration to isolate the bending energy in the energy based TO approach of HCA. Similar to general bending analysis, multiple adjacent elements are needed to accurately model the

bending deformation. Therefore, it is necessary verify the reconstruction method based on the HCA principle.

3. **RQ3. How does the bending-energy objective in HCA influence the crashworthiness performance of a sub-floor structure?**
   Finally, the framework shall be used in designing a sub-floor structure, which is to be compared to the standard HCA algorithm.

3.2 HCA Crashworthiness Model Framework

The basic HCA algorithm that is used as a starting point has been presented in this section. Furthermore, implementation and main test-case are presented to complete the framework.

3.2.1 HCA principles

For this thesis, the baseline of the TO crashworthiness HCA method was the paper by Bandi et al. [16], building the basis of this thesis' model and identities given below.

In topology optimization, an elements presence is defined by its density for solid element and thickness for shell element. This state is called the design variable x_i. The element i its material properties are scaled accordingly and can have specific penalization p and q.

$$\rho_i(x_i) = x_i \rho_0$$
$$E_i(x_i) = x_i^p E_0$$
$$\sigma_i^{yield}(x_i) = x_i^q \sigma_0^{yield}$$

The value of the design variable thus ranges from 0 to 1 and depends on the elements field variable S_i and of its neighbors S_j in the HCA principle. Typically, the state variables are averaged over their neighborhoods. This average $\overline{S}_i$ of each element i is computed for N_i number of neighbours.

$$\overline{S}_i = \frac{1}{|N_i|} \sum_{j \in N_i} S_j$$

Different neighborhood definitions exist, where adjacent elements can be used or more extended neighborhoods, see Figure 2.15. With extending, each element has more information of its surrounding, but detail is lost.

In static HCA, the strain energy is used as field variable [28] while for crashworthiness the internal energy density (IED) is more commonly used [16].The difference is that the plastic energy is included which is computed using FEM non-linear explicit crash analysis. The principle of HCA is to drive the entire domain towards a uniform distribution of this field variable. Therefore, local (cellular - CA) control rules use these field variables to increase or decrease the element's design variable x_i based on the global field variable target S^* (hence

the name hybrid in HCA). The optimization objective is thus a minimization problem of the error between the global average field variable $\overline{S}$ and its target:

$$\begin{aligned} \underset{x}{\text{minimize}} \quad & \left\| \overline{S} - S^* \right\| \\ \text{s.t.} \quad & \frac{1}{n} \sum_{i=1}^{n} x_i = M_f^* \\ & x_{min} \leq x_i \leq 1 \end{aligned} \tag{3.1}$$

In Equation 3.1 above, the design variable constraints are presented for which the total shall be smaller than the desired target mass fraction M_f^*. This mass fraction is chased by adjusting the field variable target based on the previous average field variable $\overline{S}$ and the previous mass fraction M_f for every iteration.

$$S^{*(k)} = \overline{S}^{(k-1)} \left(\frac{M_f^{(k-1)}}{M_f^*} \right)$$

The local control rule (for an iteration k) on the element design variable x_i to bring its state variable to the target is given below. Typically, not only the field variable is averaged but also the design variables. This obtains a continuous density field that good in avoiding explicit-solver failure. Checker-boarding is eliminated as well. However, the level of detail is lost.

$$\Delta x_i^{(k)} = K_p \left(\overline{S}_i^{(k)} - S^{*(k)} \right) \tag{3.2}$$

Here, K_p is the proportional control gain, which is a chosen constant. Too large and the topology will oscillate. Too small and convergence will take many iterations. The convergence criteria is met if the sum of all changes of design variable is less than a specified tolerance.

$$\sum_{i=1}^{n} (|\Delta x_i|)^{(k)} < \delta$$

There are some parameters that took a look time to decide on. There is the option to limit the maximum global change in design variable (to for example 5%) to avoid that large fluctuations in the field variable target cause unexpected radically different designs or oscillation. It was found that the limiter also has an effect on the final solution. Alternatively, the proportional gain can be lowered such that these fluctuations are less severe, but convergence will take longer or not occur.

3.2.2 Implementation

Two Altair packages have been used, namely Radioss as the non-linear solver and Compose to execute the HCA algorithm above. Their products are integrated well, with easy and fast access to the solver output. Additionally, Altair has built in topology optimization keywords

which are used by another package called Optistruct. Optistruct does not include the HCA method (it uses the ESL method for non-linear TO) so it had to be built ourselves. However, its command lines for Radioss were exploited to streamline the whole optimization within their Python post-processing application 'Compose'.

Radioss allows element assignment of thicknesses or filling percentages for shell and brick elements respectively. Scaling the latter results in equal scaling of the element density, internal forces, yield strength and Young's modulus. Unfortunately, this material interpolation is not possible for the shell elements in Radioss, only the thickness is reduced. Intermediate (and minimum) thicknesses thus retain their stiffness. However, reduced thicknesses do experience increased internal stresses, leading to weaker elements post-yielding. Moreover, the total energy is used for shell elements (as opposed to energy density for brick), integrating the bending energy density over the thickness, thereby compensating for the increased deformations.

3.2.3 HCA Crashworthiness: compression beam

The standard HCA algorithm above has as field variable the averaged local IED (or $\overline{u}_i$) for crashworthiness. In Bandi et al. [16], distributing this variable is compared to their proposed controlled energy absorption method for a variety of test-cases.

The test case that has been used in this thesis is the compression beam, of which the compressive impact loading resembles a drop-test of an aircraft sub-floor structure. The standard HCA algorithm returns a thick column which is all but compliant or energy absorbing. Ultimately, for this simple case, the ideal solution would have plastic hinge formation. Therefore, the new method has been tested on this design case.

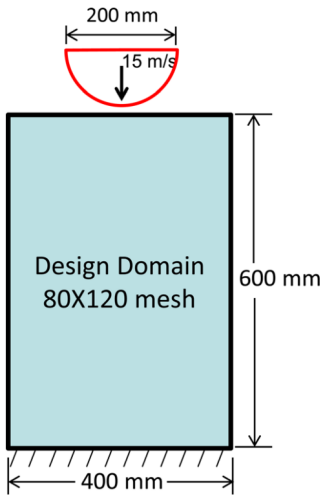

Figure 3.1: Schematic of a 2D compression beam design case with impact of a rigid pole [16]

Figure 3.1 presents the design domain, the mesh-size and impactor properties. The impactor has a mass of 15.7 kg and can slide with a friction coefficient of 0.3. The plane stress condition has been applied to be consistent with the reference.

Two adjustments have been made with respect to Bandi et al. [16]. First of all, the model (and the impactor mass) are halved. The mesh is halved along the vertical line of symmetry.

This has been decided to reduce the model size and to achieve a symmetric design. The line of symmetry only allows translation along the line of loading, constraining rotation and transverse translation. Secondly, the material model has been replaced with a Johnson-Cook model for better accuracy, presented in Figure 3.2. The values for A and B of this curve have been found through curve-fitting with a coefficient of determination of 0.9546. Other material properties have been added as well in Table 3.1.

$$\sigma = A + B\varepsilon_p^n \tag{3.3}$$

Table 3.1: Material properties used for the compression beam [16]

	Value	unit
ρ	2700	kg/m3
E	70	GPa
ν	0.33	
A	180	MPa
B	108.35	MPa
n	0.417	

The target mass fraction, initial density distribution, minimum density and convergence tolerance are respectively:

$$M_f^* = 0.3 \quad x_0 = 0.3 \quad x_{min} = 0.05 \quad \delta = 6.4$$

Since the aim was to force bending structures, hourglass control was necessary. With large expected and preferred plasticity, Radioss shell type 3 elements have been used (Q4, elasto-plastic hourglass with orthogonality).

Additionally, the implementation presented in subsection 3.2.2 can be verified for the standard HCA algorithm of distributing the IED by using the results in Bandi et al. [16]. This has been presented in chapter 4.

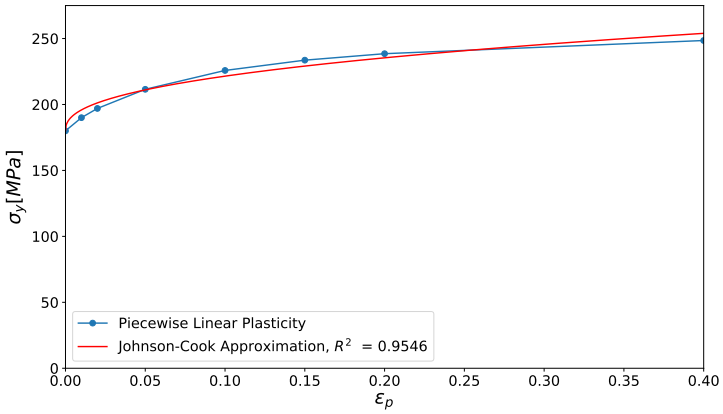

Figure 3.2: Johnson-Cook fitting of the material model used in [16]

3.3 Bending Energy

Bandi et al. [16] has shown that the original Hybrid Cellular Automata method for crashworthiness is unfit for energy absorption. Only a small portion of the kinetic energy is dissipated. When the crash behaviour of an aircraft was analyzed, most of the dissipated energy was stored in the plastically deformed elements under bending loads. Therefore, instead of aiming for uniform total strain energy, isolating its bending component might be more interesting. This section contains the bending energy derivation.

3.3.1 Strain Energy Density definition

The strain energy density u (SED, strain energy per unit volume) of an element is given in Equation 3.4. Here, the tensors are used for the stress $\boldsymbol{\sigma}$ and strain $\boldsymbol{\varepsilon}$ (elastic and plastic strain E and P respectively).

$$u = \int_{\varepsilon} \boldsymbol{\sigma} : (d\boldsymbol{\varepsilon}_E + d\boldsymbol{\varepsilon}_P) \tag{3.4}$$

This integral can also be rewritten when using time samples, where the average stress states of two subsequent timesteps is used and the total change of strain as shown in Equation 3.5. Here, i represents the timestep between the start time t_0 and the total crash duration t_{end} ($N = t_{end}/\Delta t$).

$$\boldsymbol{u} = \sum_{i=1}^{N} \left(\frac{\boldsymbol{\sigma}_i + \boldsymbol{\sigma}_{i-1}}{2} \right) \cdot (\boldsymbol{\varepsilon}_i - \boldsymbol{\varepsilon}_{i-1}) \tag{3.5}$$

The SED thus has 3 contributions for a shell element in plane stress, namely the normal directions xx and yy and the shear direction xy. The latter is doubled for isotropic material (or the engineering strain has to be used).

$$u = u_{xx} + u_{yy} + 2u_{xy} \tag{3.6}$$

$$u_{xx} = \sum_{i=1}^{N} \left(\frac{\sigma_{xx,i} + \sigma_{xx,i-1}}{2} \right) \cdot (\varepsilon_{xx,i} - \varepsilon_{xx,i-1}) \tag{3.7}$$

$$u_{yy} = \sum_{i=1}^{N} \left(\frac{\sigma_{yy,i} + \sigma_{yy,i-1}}{2} \right) \cdot (\varepsilon_{yy,i} - \varepsilon_{yy,i-1}) \tag{3.8}$$

$$u_{xy} = \sum_{i=1}^{N} \left(\frac{\sigma_{xy,i} + \sigma_{xy,i-1}}{2} \right) \cdot (\varepsilon_{xy,i} - \varepsilon_{xy,i-1}) \tag{3.9}$$

3.3.2 Strain gradient definition using FEM

Now that we have a definition for the internal energy density, the next step is to find the stress and strain function. For an bilinear quadrilateral element as shown in Figure 3.3, the strain

function can be derived from the displacements u, v. The corresponding shape functions in local coordinates given in Equation 3.10 and Equation 3.11 are used.

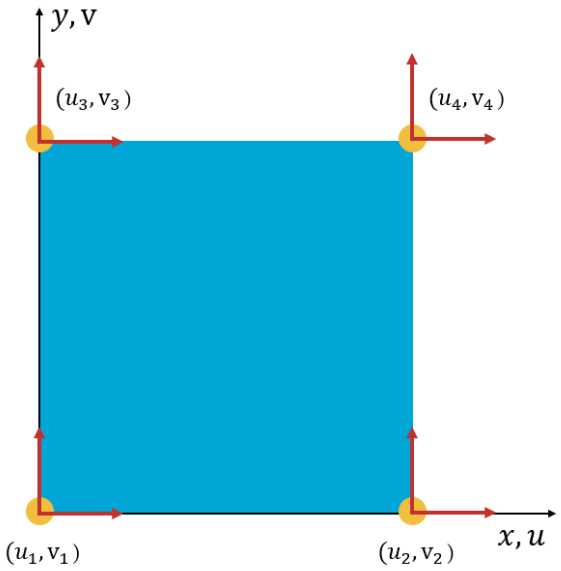

Figure 3.3: A bilinear square quadrilateral element of height and width h

$$u = c_1 + c_2x + c_3y + c_4xy \tag{3.10}$$

$$v = c_5 + c_6x + c_7y + c_8xy \tag{3.11}$$

Solving for the constants gives:

$$u = u_1 + \frac{1}{h}(u_2 - u_1)x + \frac{1}{h}(u_3 - u_1)y + \frac{1}{h^2}(u_1 - u_2 - u_3 + u_4)xy$$

Gather all nodal displacements $u_1..u_4$:

$$u = \left(1 - \frac{x}{h}\right)\left(1 - \frac{y}{h}\right)u_1 + \frac{x}{h}\left(1 - \frac{y}{h}\right)u_2 + \frac{y}{h}\left(1 - \frac{x}{h}\right)u_3 + \frac{xy}{h^2}u_4$$

Changing the coordinate system to natural coordinates (see Figure 3.4) we require the change of coordinate functions through normalization using width h:

$$r = \frac{2x}{h} - 1 \tag{3.12}$$

$$s = \frac{2y}{h} - 1 \tag{3.13}$$

Resulting in the final bilinear equation for the displacements u and v as:

$$u = \frac{1}{4}(1-r-s+rs)u_1 + \frac{1}{4}(1+r-s-rs)u_2 + \frac{1}{4}(1-r+s-rs)u_3 + \frac{1}{4}(1+r+s+rs)u_4 \tag{3.14}$$

$$v = \frac{1}{4}(1-r-s+rs)v_1 + \frac{1}{4}(1+r-s-rs)v_2 + \frac{1}{4}(1-r+s-rs)v_3 + \frac{1}{4}(1+r+s+rs)v_4 \quad (3.15)$$

Moving from displacements to strains, we can make use of the Lagrangian finite strain tensor.

$$\varepsilon_{ij} = \frac{1}{2}\left(\frac{\partial u_i}{\partial x_j} + \frac{\partial u_j}{\partial x_i} + \frac{\partial u_k}{\partial x_i}\frac{\partial u_k}{\partial x_j}\right) \quad (3.16)$$

To simplify the model, the infinitesimal strain tensor is used, meaning that we remove the non-linear part as we assume that the strains are small. However, with large plasticity, the non-linear part is best included.

$$\varepsilon_{ij} = \frac{1}{2}\left(\frac{\partial u_i}{\partial x_j} + \frac{\partial u_j}{\partial x_i}\right) \quad (3.17)$$

For Equation 3.17, we can derive the normal and shear strains as:

$$\varepsilon_{xx} = \frac{\partial u}{\partial x} \quad (3.18)$$

$$\varepsilon_{yy} = \frac{\partial v}{\partial y} \quad (3.19)$$

$$\varepsilon_{xy} = \frac{1}{2}\left(\frac{\partial u}{\partial y} + \frac{\partial v}{\partial x}\right) \quad (3.20)$$

The strain for such elements are (where $dr/dy = ds/dx = 0$):

$$\varepsilon_{xx} = \frac{\partial u}{\partial x} = \frac{\partial u}{\partial r}\frac{\partial r}{\partial x} + \frac{\partial u}{\partial s}\frac{\partial s}{\partial x} = \frac{\partial u}{\partial r}\frac{2}{h}$$

$$\varepsilon_{yy} = \frac{\partial v}{\partial y} = \frac{\partial v}{\partial r}\frac{\partial r}{\partial y} + \frac{\partial v}{\partial s}\frac{\partial s}{\partial y} = \frac{\partial v}{\partial s}\frac{2}{h}$$

$$\varepsilon_{xy} = \frac{1}{2}\left(\frac{\partial u}{\partial y} + \frac{\partial v}{\partial x}\right) = \frac{1}{2}\left(\frac{\partial u}{\partial r}\frac{\partial r}{\partial y} + \frac{\partial u}{\partial s}\frac{\partial s}{\partial y} + \frac{\partial v}{\partial r}\frac{\partial r}{\partial x} + \frac{\partial v}{\partial s}\frac{\partial s}{\partial x}\right) = \frac{1}{2}\left(\frac{\partial u}{\partial s}\frac{\partial s}{\partial y} + \frac{\partial v}{\partial r}\frac{\partial r}{\partial x}\right) = \frac{1}{h}\left(\frac{\partial u}{\partial s} + \frac{\partial v}{\partial r}\right)$$

Plugging in u and v gives:

$$\varepsilon_{xx} = \frac{\partial u}{\partial r}\frac{2}{h} = \frac{1}{2h}(-u_1 + u_2 - u_3 + u_4) + \frac{1}{2h}(u_1 - u_2 - u_3 + u_4)s$$

$$\varepsilon_{yy} = \frac{\partial v}{\partial s}\frac{2}{h} = \frac{1}{2h}(-v_1 - v_2 + v_3 + v_4) + \frac{1}{2h}(v_1 - v_2 - v_3 + v_4)r$$

$$\varepsilon_{xy} = \left(\frac{\partial u}{\partial s} + \frac{\partial v}{\partial r}\right)\frac{1}{h} = \frac{1}{4h}((-u_1 - u_2 + u_3 + u_4) + (u_1 - u_2 - u_3 + u_4)r + (-v_1 + v_2 - v_3 + v_4) + (v_1 - v_2 - v_3 + v_4)s)$$

As can be concluded, the strains are linear functions of s or r. The gradients of these functions are the derivatives as given below:

$$\frac{\partial \varepsilon_{xx}}{\partial x} = \frac{\partial \varepsilon_{xx}}{\partial r}\frac{\partial r}{\partial x} + \frac{\partial \varepsilon_{xx}}{\partial s}\frac{\partial s}{\partial x} = 0$$

$$\frac{\partial \varepsilon_{xx}}{\partial y} = \frac{\partial \varepsilon_{xx}}{\partial r}\frac{\partial r}{\partial y} + \frac{\partial \varepsilon_{xx}}{\partial s}\frac{\partial s}{\partial y} = \frac{\partial \varepsilon_{xx}}{\partial s}\frac{2}{h} = \frac{1}{h^2}(u_1 - u_2 - u_3 + u_4)$$

$$\frac{\partial \varepsilon_{yy}}{\partial x} = \frac{\partial \varepsilon_{yy}}{\partial r}\frac{\partial r}{\partial x} + \frac{\partial \varepsilon_{yy}}{\partial s}\frac{\partial s}{\partial x} = \frac{\partial \varepsilon_{yy}}{\partial r}\frac{2}{h} = \frac{1}{h^2}(v_1 - v_2 - v_3 + v_4)$$

$$\frac{\partial \varepsilon_{yy}}{\partial y} = \frac{\partial \varepsilon_{yy}}{\partial r}\frac{\partial r}{\partial y} + \frac{\partial \varepsilon_{yy}}{\partial s}\frac{\partial s}{\partial y} = 0$$

$$\frac{\partial \varepsilon_{xy}}{\partial x} = \frac{\partial \varepsilon_{xy}}{\partial r}\frac{\partial r}{\partial x} + \frac{\partial \varepsilon_{xy}}{\partial s}\frac{\partial s}{\partial x} = \frac{\partial \varepsilon_{xy}}{\partial r}\frac{2}{h} = \frac{1}{2h^2}(u_1 - u_2 - u_3 + u_4)$$

$$\frac{\partial \varepsilon_{xy}}{\partial y} = \frac{\partial \varepsilon_{xy}}{\partial r}\frac{\partial r}{\partial y} + \frac{\partial \varepsilon_{xy}}{\partial s}\frac{\partial s}{\partial y} = \frac{\partial \varepsilon_{xy}}{\partial s}\frac{2}{h} = \frac{1}{2h^2}(v_1 - v_2 - v_3 + v_4)$$

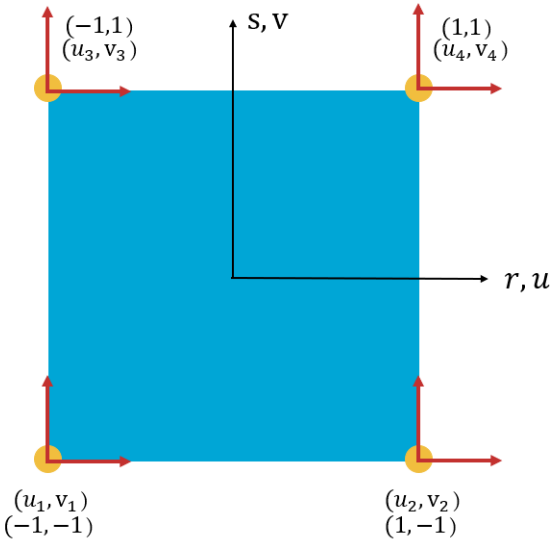

Figure 3.4: A bilinear square quadrilateral element of height and width h in natural coordinates

The displacements in the expressions above can be grouped for each side of the quadrilateral element. This has been visualized in Figure 3.5. By replacing these identities in the gradients we get the final expressions:

$$\frac{\partial \varepsilon_{xx}}{\partial y} = \frac{\varepsilon_{xx}^{TOP} - \varepsilon_{xx}^{BOTTOM}}{h} \tag{3.21}$$

$$\frac{\partial \varepsilon_{yy}}{\partial x} = \frac{\varepsilon_{yy}^{RIGHT} - \varepsilon_{yy}^{LEFT}}{h} \tag{3.22}$$

$$\frac{\partial \varepsilon_{xy}}{\partial y} = \frac{\varepsilon_{xy}^{TOP} - \varepsilon_{xy}^{BOTTOM}}{h} \tag{3.23}$$

$$\frac{\partial \varepsilon_{xy}}{\partial x} = \frac{\varepsilon_{xy}^{RIGHT} - \varepsilon_{xy}^{LEFT}}{h} \tag{3.24}$$

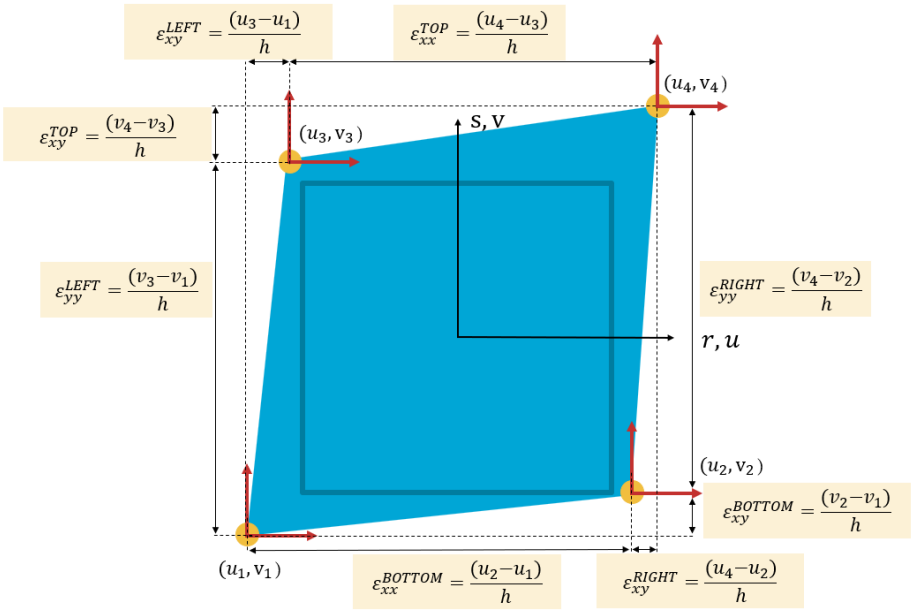

Figure 3.5: A deformed element with infinitesimal strains

3.3.3 Bending Energy definition

In subsection 3.3.2, the small strain deformation has been assumed allowing the usage of the infinitesimal strain tensor. This tensor neglects the non-linear terms presented in Equation 3.16. As a result, the derived strains are linearly varying across the element, see Equation 3.21-Equation 3.24. The corresponding stress gradient approximations are then also linear.

Looking back at Equation 3.6, the strain energies u_{xx}, u_{yy} and $2u_{xy}$ are now functions of x, y and (x,y) respectively under the small strain assumption, presented in Equation 3.25. The shear term can be split in a variation along x or a variation along y with the gradient functions defined in Equation 3.24 and Equation 3.23.

$$u = u_{xx}(y) + u_{yy}(x) + u_{xy}(x) + u_{xy}(y) \tag{3.25}$$

We want to isolate the energy stemming from bending deformation in the internal energy function. Since first order linear elements cannot follow the curvature of a bend, shear stress is introduced in the element under shear-locking. Therefore, the full expression including the shear terms is used for the bending energy derivation. The use of linear elements for bending maximization can be questioned, since linear elements are stiffer in bending together with the aforementioned shear-locking. However, if topology solutions consist of bending sections of at least 3 elements thick, the issue can be neglected.

The linear functions for the energy portion that represent the pure bending deformation are presented below for the strain. Interchange ε for σ for the stress field functions.

$$\varepsilon_{xx}(y) = \frac{d\varepsilon_{xx}}{dy}y + \varepsilon_{xx,y=0} \tag{3.26}$$

$$\varepsilon_{yy}(x) = \frac{d\varepsilon_{yy}}{dx}x + \varepsilon_{yy,x=0} \tag{3.27}$$

$$\varepsilon_{xy}(y) = \frac{d\varepsilon_{xy}}{dy}y + \varepsilon_{xy,y=0} \tag{3.28}$$

$$\varepsilon_{xy}(x) = \frac{d\varepsilon_{xy}}{dx}x + \varepsilon_{xy,x=0} \tag{3.29}$$

The SED equation in Equation 3.4 needs to be integrated over the element volume to find the total element internal energy.

$$U = \int_V u dV = \int_x \int_y \int_z u dz dy dx \tag{3.30}$$

When we consider the variations along the y-axis, the integrals over x and z can be replaced with their respective widths. For a shell with square elements, the widths along x and y are h and t for z. The internal energy for the two normal stresses and strains is thus:

$$U_{xx} = ht \int_y u_{xx}(y) dy \tag{3.31}$$

$$U_{yy} = ht \int_x u_{yy}(x) dx \tag{3.32}$$

$$U_{xy,1} = ht \int_y u_{xy}(y) dy \tag{3.33}$$

$$U_{xy,2} = ht \int_x u_{xy}(x) dx \tag{3.34}$$

Inserting Equation 3.26 and its stress function counterpart (interchanging epsilon with sigma) in Equation 3.7 and integrating as shown in Equation 3.31 (for element width h) gives in the internal energy function:

$$\begin{aligned}\Delta U_{xx} = \frac{1}{2}ht\Bigg[&\frac{1}{3}\left(\left(\frac{d\sigma_{xx}}{dy}\right)_i + \left(\frac{d\sigma_{xx}}{dy}\right)_{i-1}\right)\left(\left(\frac{d\varepsilon_{xx}}{dy}\right)_i - \left(\frac{d\varepsilon_{xx}}{dy}\right)_{i-1}\right)y^3 \\ &+ \frac{1}{2}\Bigg(\left(\left(\frac{d\sigma_{xx}}{dy}\right)_i + \left(\frac{d\sigma_{xx}}{dy}\right)_{i-1}\right)(\varepsilon_{xx,y=0_i} - \varepsilon_{xx,y=0_{i-1}}) + \\ &\left(\left(\frac{d\varepsilon_{xx}}{dy}\right)_i - \left(\frac{d\varepsilon_{xx}}{dy}\right)_{i-1}\right)(\sigma_{xx,y=0_i} + \sigma_{xx,y=0_{i-1}})\Bigg)y^2 \\ &+ (\sigma_{xx,y=0_i} + \sigma_{xx,y=0_{i-1}})(\varepsilon_{xx,y=0_i} - \varepsilon_{xx,y=0_{i-1}})y\Bigg]_{-h/2}^{h/2}\end{aligned} \tag{3.35}$$

The same applies to the other equations from Equation 3.32, Equation 3.33 and Equation 3.34. What can be seen is that the equation is composed of three parts.

1. Integrated quadratic IED distribution: Average stress gradient multiplied with the change in strain gradient
2. Integrated linear IED distribution: The inner product of the previous one and the next one
3. Integrated uniform IED distribution: The average mean stress multiplied with the change in mean strain

The third part resembles the general internal energy from Equation 3.5 for reduced-integration elements, where the strain gradient is smeared out to be 0 as the mean strain is taken at the integration point. This can be seen in the left figure of Figure 3.6. In terms of Equation 3.35, the linear part (that integrated to y^2) in Equation 3.36 disappears due to its bounds as its energy is considered in the third part. However, we want to isolate this energy (right figure in Figure 3.6) and thus the mean value is removed as presented in Equation 3.36.

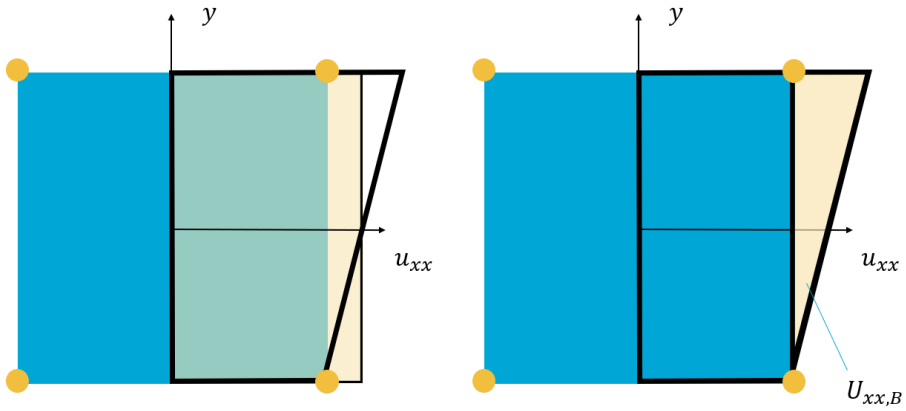

Figure 3.6: Internal energy distribution (direction xx) if the stress distribution is uniform with a linear strain distribution. Left would be the generalized internal energy, right figure showcases the desired bending energy fraction.

Figure 3.6 presents the fraction that remains (right side) for the second part. Note that the internal energy function would also have the quadratic term (that integrated to y^3 in Equation 3.36) if we assume linearity in the stress distribution, however it has not been plotted for clarity on part and its bounds.

$$\begin{aligned}\Delta U_{Bend,xx} = \frac{1}{2}ht\Bigg[&\frac{1}{3}\left(\left(\frac{d\sigma_{xx}}{dy}\right)_i + \left(\frac{d\sigma_{xx}}{dy}\right)_{i-1}\right)\left(\left(\frac{d\varepsilon_{xx}}{dy}\right)_i - \left(\frac{d\varepsilon_{xx}}{dy}\right)_{i-1}\right)y^3 \\ &+\frac{1}{2}\Bigg(\left(\left(\frac{d\sigma_{xx}}{dy}\right)_i + \left(\frac{d\sigma_{xx}}{dy}\right)_{i-1}\right)(\varepsilon_{xx,y=0_i} - \varepsilon_{xx,y=0_{i-1}}) + \\ &\left(\left(\frac{d\varepsilon_{xx}}{dy}\right)_i - \left(\frac{d\varepsilon_{xx}}{dy}\right)_{i-1}\right)(\sigma_{xx,y=0_i} + \sigma_{xx,y=0_{i-1}})\Bigg)y^2\Bigg]_{-h/2}^{h/2}\end{aligned} \tag{3.36}$$

The bending energy of the linear part (presented as $U_{xx,B}$ in Figure 3.6) is found by changing its bounds to $[0, h]$, such that it does not cancel out. The quadratic IED function keeps its original bounds. Working this out for Equation 3.36 and (as presented in Figure 3.6) the total incremental change in bending energy is given as:

$$\begin{aligned}\Delta U_{Bend,xx} = \frac{1}{24}\left(\left(\frac{d\sigma_{xx}}{dy}\right)_i + \left(\frac{d\sigma_{xx}}{dy}\right)_{i-1}\right)\left(\left(\frac{d\varepsilon_{xx}}{dy}\right)_i - \left(\frac{d\varepsilon_{xx}}{dy}\right)_{i-1}\right) th^4 \\ + \frac{1}{4}\Bigg(\left(\left(\frac{d\sigma_{xx}}{dy}\right)_i + \left(\frac{d\sigma_{xx}}{dy}\right)_{i-1}\right)(\varepsilon_{xx,y=0_i} - \varepsilon_{xx,y=0_{i-1}}) + \\ \left(\left(\frac{d\varepsilon_{xx}}{dy}\right)_i - \left(\frac{d\varepsilon_{xx}}{dy}\right)_{i-1}\right)(\sigma_{xx,y=0_i} + \sigma_{xx,y=0_{i-1}})\Bigg) th^3 \end{aligned} \tag{3.37}$$

Only its component for the xx-direction is shown above, yy and xy are also used as seen below following Equation 3.25.

$$\Delta U_{Bend} = \Delta U_{bend,xx} + \Delta U_{bend,yy} + \Delta U_{bend,xy,1} + \Delta U_{bend,xy,2} \tag{3.38}$$

For the final expression of the bending energy Equation 3.37, the change in bending energy shall be computed using an incremental process. For each timestep, the following four states are computed for each of the four terms in Equation 3.38:

1. Strain gradient
$$\frac{d\varepsilon_{xx}}{dy}, \frac{d\varepsilon_{yy}}{dx}, \frac{d\varepsilon_{xy}}{dy}, \frac{d\varepsilon_{xy}}{dx}$$
2. Stress gradient
$$\frac{d\varepsilon_{xx}}{dy}, \frac{d\varepsilon_{yy}}{dx}, \frac{d\varepsilon_{xy}}{dy}, \frac{d\varepsilon_{xy}}{dx}$$
3. Strain at the element center
$$\varepsilon_{xx,y=0}, \varepsilon_{yy,x=0}, \varepsilon_{xy,y=0} = \varepsilon_{xy,x=0}$$
4. Stress at the element center
$$\sigma_{xx,y=0}, \sigma_{yy,x=0}, \sigma_{xy,y=0} = \sigma_{xy,x=0}$$

Note that the shear terms (stress or strain) at the element center are equal in both directions.

3.3.4 Linear internal energy density (L-IED) to physical energy formulations

For the linear part of the IED function, which is quadratic once integrated to total IE as given below, sign convention needs to be put in order. Namely, what does a positive or negative,

stress or strain gradient mean?

$$\frac{1}{4}\Bigg(\left(\left(\frac{d\sigma_{xx}}{dy}\right)_i + \left(\frac{d\sigma_{xx}}{dy}\right)_{i-1}\right)(\varepsilon_{xx,y=0_i} - \varepsilon_{xx,y=0_{i-1}}) + \left(\left(\frac{d\varepsilon_{xx}}{dy}\right)_i - \left(\frac{d\varepsilon_{xx}}{dy}\right)_{i-1}\right)(\sigma_{xx,y=0_i} + \sigma_{xx,y=0_{i-1}})\Bigg)th^3$$

These incremental changes are simplified to:

$$\frac{1}{2}\left(\left(\frac{d\sigma_{xx}}{dy}\right)_{avg}\Delta\varepsilon_{xx,y=0} + \left(\Delta\frac{d\varepsilon_{xx}}{dy}\right)(\sigma_{xx,y=0})_{avg}\right)th^3$$

A positive stress gradient and negative change of mean strain would result in nonphysical negative energy.

Several solutions have been found that each gave different results. This section presents the logical solution first, followed by two fictional definitions that could lead to more excessive bending and finally one for post-yielding.

The goal is to find the best definition for plastic hinge formation.

Option L-IED-1: Loading specified gradient

Suppose the average stress gradient is positive due to $\sigma_{top} > \sigma_{bottom}$. This could have two possible meanings as shown in Figure 3.7.

1. The stress at the top is in tension while the bottom is less in tension (or even compression)

2. The stress at the top is in compression while the bottom is even more in compression

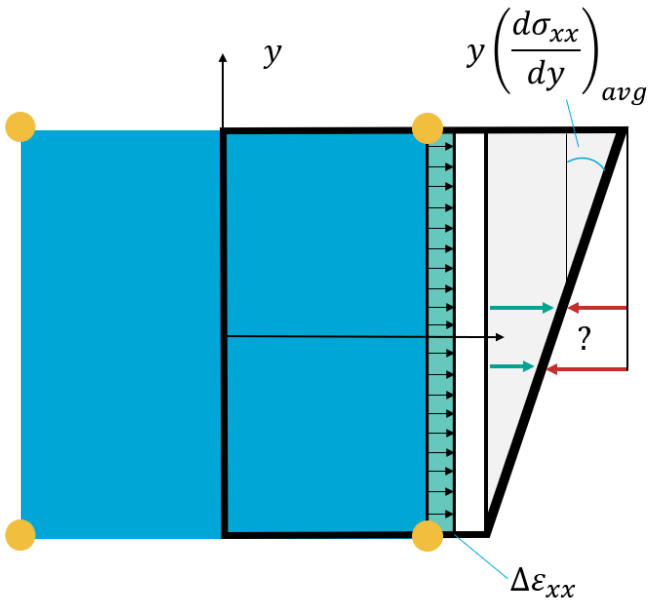

Figure 3.7: Sign convention of gradients: Uniform change in strain distribution with a linear stress distribution example I

This average stress gradient is multiplied with the change in mean strain (the strain of the center integration point). For this option, the sign of the stress gradient is removed and given the sign of the average stress, which is equal to what is underneath the gradient.

$$\left(\frac{d\sigma_{xx}}{dy}\right)_{avg,NEW} = \left|\left(\frac{d\sigma_{xx}}{dy}\right)_{avg}\right| \frac{(\sigma_{xx,y=0})_{avg}}{|(\sigma_{xx,y=0})_{avg}|}$$

Energy will accumulate for any gradient direction as long as its stress underneath is in line with the change in strain.

Similarly for the other part:

$$\left(\Delta\frac{d\varepsilon_{xx}}{dy}\right)_{NEW} = \left|\Delta\frac{d\varepsilon_{xx}}{dy}\right| \frac{\Delta\varepsilon_{xx,y=0}}{|\Delta\varepsilon_{xx,y=0}|}$$

Option L-IED-2: Single-bend maximization

The linear IED function can also be manipulated such that elements that bend in one direction only are prioritized, maximizing this single-sided bending. This can be achieved by keeping the sign of the gradient and removing the sign of its product:

$$\frac{1}{2}\left(\left(\frac{d\sigma_{xx}}{dy}\right)_{avg}|\Delta\varepsilon_{xx,y=0}| + \left(\Delta\frac{d\varepsilon_{xx}}{dy}\right)|(\sigma_{xx,y=0})_{avg}|\right)th^3$$

Once the gradient direction flips, or the stress gradient is not in-line with the change in strain gradient, energy is 'lost' in this manipulated form. Negative energies (gained from negative

bending deformation) are made positive after summation:

$$U_{Bend} = |\sum_{i=1}^{N} \Delta U_{bend,xx}| + |\sum_{i=1}^{N} \Delta U_{bend,yy}| + |\sum_{i=1}^{N} \Delta U_{bend,xy,1}| + |\sum_{i=1}^{N} \Delta U_{bend,xy,2}|$$

Elements that deformed primarily in one direction have higher energies and will thus be prioritized to keep.

Option L-IED-3: Full single-load maximization

This method returns the energy in a single deformation direction. The energy due to the change in mean stress, irrespective of compression or tension, is accumulated until its direction flips. The same is enforced on the change in strain gradient: energy is lost if the element bends back.

$$\frac{1}{2}\left(\left|\left(\frac{d\sigma_{xx}}{dy}\right)_{avg}\right| (|\varepsilon_{xx,y=0_i}| - |\varepsilon_{xx,y=0_{i-1}}|) + \left(\left|\frac{d\varepsilon_{xx}}{dy}\right|_i - \left|\frac{d\varepsilon_{xx}}{dy}\right|_{i-1}\right) |(\sigma_{xx,y=0})_{avg}|\right) th^3$$

Basically, the above behaves like an elastic material where energy is lost when unloading.

Option L-IED-4: Plasticity corrected L-IED-3

L-IED-3 can be altered to include plasticity, although still considering linear gradient approximation. When an element reaches plasticity, its accumulated energy is set and can only increase. Thus L-IED-3 is used until plasticity:

$\varepsilon_p > 0$:

$$\frac{1}{2}\left(\left|\left(\frac{d\sigma_{xx}}{dy}\right)_{avg}\right| |\Delta\varepsilon_{xx,y=0}| + \left|\Delta\frac{d\varepsilon_{xx}}{dy}\right| |(\sigma_{xx,y=0})_{avg}|\right) th^3$$

The above equation neglects elastic spring-back and loss of energy, however, this loss is negligible against the plastic work from large strains.

3.3.5 L-IED comparison and preference study

Above, 4 formulations are given for the L-IED function. A study has been performed on the solutions each of these formulations delivered. The one that is optimized for bending is used in subsequent studies.

The L-IED is only half of the equation of Equation 3.37, with the quadratic distribution of the internal energy (Q-IED) as the counterpart. It was believed that a pure bending section is not necessarily loaded in additional shear, compression or tension. This latter is present in the L-IED functions and overshadows the first Q-IED functions.

The relative influence of the two halves can be manipulated to optimize for bending. These results have been given in the preference study.

3.4 Bending Optimization in HCA

While the derivation of the gradients presented in subsection 3.3.2 can be used to compute the bending energy of a single FEM element, it is expected to be too detailed to be useful. Topology optimization using the true bending energy of each element is expected to give sections that are 1 element wide and loaded in bending. As a result, the neutral axis of the bend is exactly at the element center for which the strain would be 0. For an efficient crash-analysis, reduced order element are preferred but these are unstable to such deformation modes leading to hourglassing. While most solver have hourglass controls to overcome this issue, the required resisting loads are non-phyisical and should thus be minimized. Therefore, it is preferred to extend the domain on which the strain gradients are computed, with the expectation that local (1 cell) bending deformations are filtered out since they are not detected. Only bending deformations that span multiple cells are detected. This could potentially construct bending sections of the size of the extended domain.

3.4.1 Gradients in HCA

Using the Hybrid Cellular Automata principle, the adjacent elements are used to extend the domain and compute the gradients. With the infinitesimal strain assumption, the strain remains linear into these adjacent elements. Therefore, we can extract the neighboring mean strains (evaluated at their centers) to compute the gradients presented in Equation 3.21-Equation 3.24. Figure 3.8 presents one of these gradients computed from the mean strain values of the adjacent elements.

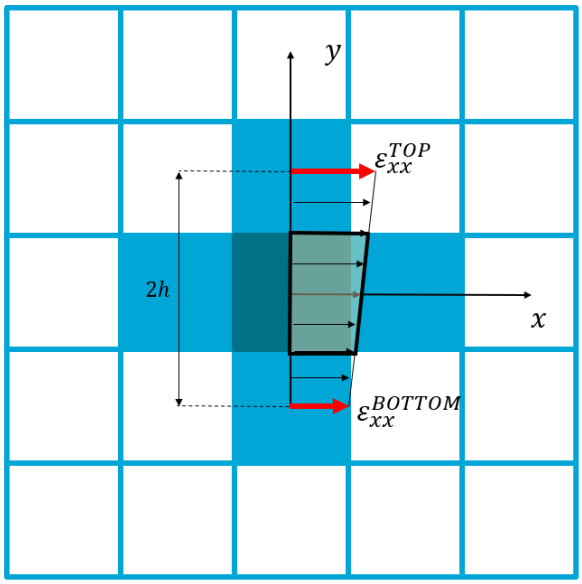

Figure 3.8: Gradient computation using the HCA principle showcased for $\frac{\partial \varepsilon_{xx}}{\partial y}$

By extending the domain of the gradient computation, the height increases to $2h$. The integration over y (as presented in Equation 3.36) is still performed over height $h(y = -h/2, y = h/2)$ as is depicted using the yellow box in Figure 3.9.

$$\frac{\Delta\varepsilon_{xx}}{\Delta y} = \frac{\varepsilon_{xx}^{TOP} - \varepsilon_{xx}^{BOTTOM}}{2h}$$

For corner or edges, the element's own mean strain (center strain) is used to compute the gradients, as shown in Figure 3.9.

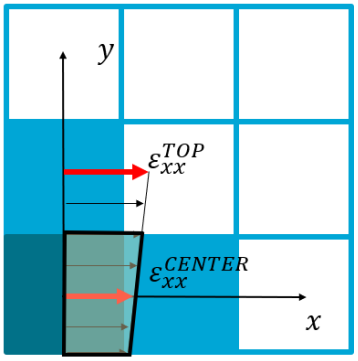

Figure 3.9: Gradient computation using the HCA principle showcased for $\frac{\partial\varepsilon_{xx}}{\partial y}$ in a corner

Following the procedures of the strain-gradient definition, the stress gradients can be derived from the neighboring elements as well. The result can be seen below in Equation 3.39.

$$\frac{\Delta\sigma_{xx}}{\Delta y} = \frac{\sigma_{xx}^{TOP} - \sigma_{xx}^{BOTTOM}}{2h} \tag{3.39}$$

3.4.2 Gradients in HCA: Voxelmesh material interpolation

For the brick elements in the sub-floor structure case, one adjustment had to be made in the BOHCA framework with respect to the shell model application. In subsection 3.2.2, it has been discussed briefly that Radioss does not yet include material-interpolation for thickness optimization of shell elements, although the results do not significantly differ (Appendix B). Stiffness interpolation is required in gradient-based optimization. In the HCA algorithm, the heuristic rules only require a decreasing relation between the considered energy and the design variable, which is obtained since thinner absorb less energy. By integrating the IED over the thickness, convergence can still be reached.

Contrary to shell elements, the reduction of volume in brick elements cannot be implemented in the FEM model. Material interpolation is thus required for the optimization to take affect in the non-linear dynamic analysis. The material degradation, as shown in section 3.2, ensures the lower density elements result in less energy dissipation.

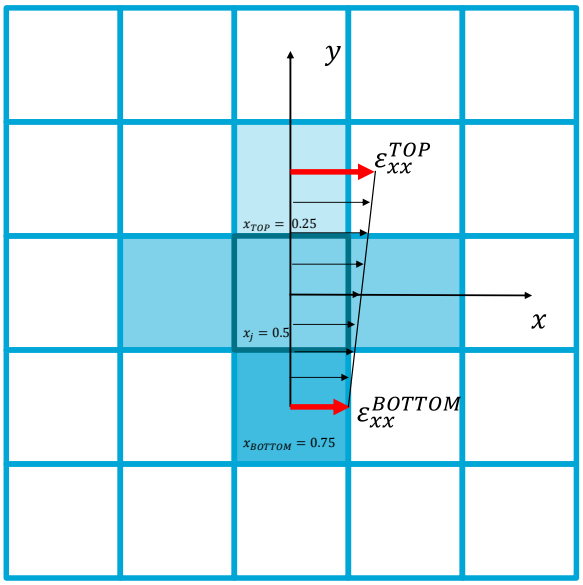

Figure 3.10: Thickness gradient along bending direction with hypothetical strains

Now suppose adjacent elements of different densities are bending as shown in Figure 3.10. Both will strain in the direction of deformation, leading to a consistent strain gradient. However, the reduced density element will have a lower stress state due to its decreased young's Modulus and yield strength. The stress distribution can become non-representative of the loading as the gradients become smaller or possibly even opposite towards the direction of bending. Especially once in the plastic domain, looking at Figure 3.11, the different densities would hypothetically result in an opposite stress gradient.

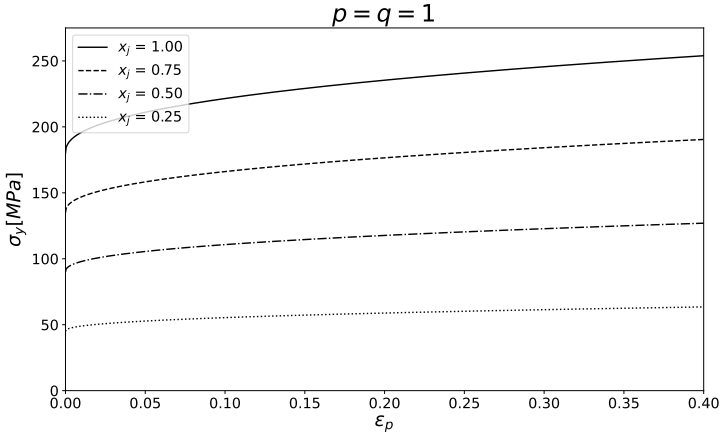

Figure 3.11: Yield stress for different values of element density

Alternatively, suppose these three elements are all plastically extending uniformly (equal plas-

tic strains). Their density gradient result in non-uniform stress distribution leading towards non-existent bending energy.

To correct the stress gradient to be in-line with the deformation direction, the stresses need to be normalized. Following this, the gradient magnitude is then brought back to its degraded state by the center elements density.

$$\frac{\partial \sigma_{xx}}{\partial y} = \frac{(\frac{\sigma_{xx}}{x})_{TOP} - (\frac{\sigma_{xx}}{x})_{BOTTOM}}{2h} x_j \tag{3.40}$$

Proving the necessity of this correction has been presented in Appendix A, including topology solutions.

To Do; show non-linear plasticity plot and approximate function

3.4.3 Bending-energy optimization algorithm

The procedure of the bending-energy optimization is similar to that of the standard HCA seeking for uniform IED distribution. The main difference is that the IED is displaced by the bending energy (BE).

$$\begin{aligned} \underset{x}{\text{minimize}} \quad & \left\| \overline{U_{bend}} - U^*_{bend} \right\| \\ \text{s.t.} \quad & \frac{1}{n} \sum_{j=1}^{n} x_j = M^*_f \\ & x_{min} \leq x_j \leq 1 \end{aligned} \tag{3.41}$$

The objective formulation from section 3.2 now drives the newly composed bending energy towards uniformity. For clarity, here is the bending energy equation for N evaluations within the timeframe. The set timeframe is found separately for each iteration k and is picked at the peak internal energy. This ensures all of the possible dissipated energy has been captured.

$$U_{Bend_j} = \sum_{i=1}^{N} \Delta U_{bend,xx_{ij}} + \sum_{i=1}^{N} \Delta U_{bend,yy_{ij}} + \sum_{i=1}^{N} \Delta U_{bend,xy,1_{ij}} + \sum_{i=1}^{N} \Delta U_{bend,xy,2_{ij}} \tag{3.42}$$

This bending energy per element j is averaged with its neighbors before computing its error with the global target.

3.5 Sub-floor structure Idealization and Topology Optimization

To answer the hypothesis, it is necessary to ensure the crash-responses of TO solutions are reliable. This led to the first research question. One way would be to find the topology, translate it to a manufacturable design and perform a detailed crash-analysis. This final

crash-performance is hypothetical and would be best validated with a experiment. For the duration of this thesis, a shorter route has been designed by starting from a validated design.

In Figure 2.11, the A320 FEM model crash-deformation has been shown which was extracted from Gransden and Alderliesten [11]. This deformation was generally consistent with experimental results in terms of hinge formation and in passenger accelerations, considering the variations between several seating locations [11]. Therefore, these results are used to validate the crash-behaviour reliability of a voxel-mesh representation. Reasoning and results of the detailed model idealization are presented in this section.

3.5.1 Idealization Assumptions

Topology optimization in the form presented in this thesis, to find the optimal distribution of material in earliest design phases, would not produce thin-walled structures of the papers presented in subsection 2.1.3 without requiring millions of brick-elements. The major deformation mode present in the literature for drop testing happened in planar bending. Several assumptions have been made in the translation of a thin-walled several-frame model to a voxel-mesh planar model:

1. It is assumed that small-scale deformation modes (buckling of the thin-walled structures) of the sections are negligible compared to the large-scale planar bending behaviour described above. Therefore, it is assumed that the hinge-formation capabilities will be unaffected. However, the global energy absorption capabilities will be affected, as shown by Gransden and Alderliesten [11] where the cargo floor structure does plastically deform under the buckling loads.

2. The crash-response seen for the A350-like six-frame (half-barrel) model in Gransden and Alderliesten [11] (and in Figure 2.11) is constant along the fuselage section. Therefore, it can be assumed that a planar model consisting of only 1 layer of elements in depth direction can achieve the same response. Additionally, the out-of-plane sections can be removed such as the tracks and stringers as their influence to the planar bending is assumed negligible.

3. The deformation seen in the cabin in Figure 2.11 and the absorbed energy of its floor in **??** are very small, therefore it is assumed its influence on the occurrence of plastic hinge formation is negligible. This allows for model size reduction by replacing the cabin with a rigid-coupling constraint. Again, the amount of energy absorbed per hinge and their exact location might be affected.

4. Following the results from **??**. It is assumed that the frame assembly' bending response and energy capability is dominated by the stiff and large frame. Therefore, the thin skin and its brackets are neglected.

5. It is assumed that every aircraft, conventional and unconventional, will always include frames. The frame of the A350-like aircraft has thus been taken out of the design space. As a result, the load impact load will be distributed more evenly into the design space. Additionally, in !!!, the optimization in displacement maximization resulted in removal of mass closest to the impact site, reducing cargo-hold volume. This design choice maintains the outer shape of the aircraft.

6. Since the large scale crash-response is bending dominated, it is assumed that the bending stiffness of the thin-walled structural sections can be used to replace them with solid brick-sections (voxel-mesh).

3.5.2 Section idealization results of the A350-like aircraft

The A350 sub-floor structure is very detailed and consists of thin-walled elements. Following assumptions 1 and 6 above, the goal is to replicate the response of the thin-walled sub-floor structure in a crash event with a voxel-mesh model, by idealizing the sections with solid 3D elements (see Figure 3.13 for the idealized cross-sections). Since the crash response is bending dominated, the choice has been made to idealize the thin-walled sections based on their moment of inertia's (compared to cross sectional area for axial/shear forces).

The FEM model of the A350-like aircraft six-frame model (see Figure 3.12) and its approximate dimensions have been used to idealize the sections.

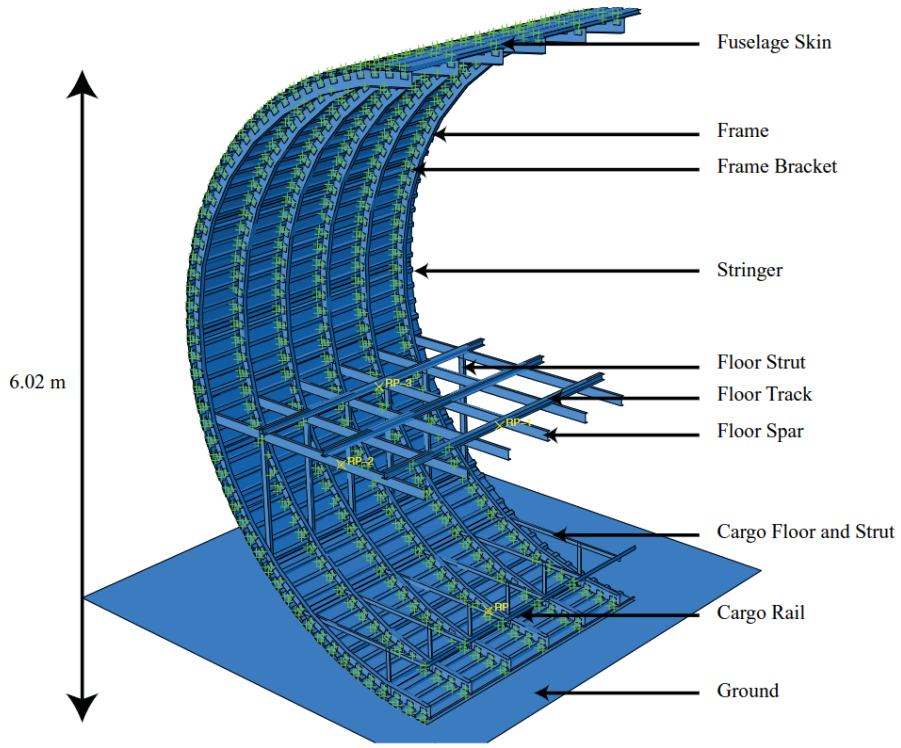

Figure 3.12: Half-barrel six-frame model of the A350-like aircraft from Gransden and Alderliesten [11]

From assumption number 2, 3 and 4, only the sub-floor structure will be modelled and the floor-cabin domain will be replaced with a rigid body. The left-over sections and dimensions can be found in Table 3.2.

Table 3.2: A350-like thin-walled sectional dimensions and MOI

	Section	$t[mm]$	$h_{web}[mm]$	$w_{flange,1}[mm]$	$w_{flange,2}[mm]$	$I_{xx}[mm^4]$
Frame	Z	3	132	45	14	$1.31 * 10^6$
Floor strut	C	3	60	30	30	$2.08 * 10^5$
Cargo floor	C	3	40	22	8	$4.84 * 10^4$
Cargo fl. strut	C	3	40	8	8	$3.16 * 10^4$

A section under bending should at least have 3-4 elements. So the desired mesh sizes of size (h x h x t) can be found using $I_{xx} = \frac{1}{12}t(3h)^3$. However, each section requires its own mesh size. Thus elements will be either over or under approximated for 1 uniform mesh size.

Cubic elements are unfit for this purpose when a mesh-study is to be performed, due to the design choice to only model 1 layer following assumption 2. Different mesh-sizes will have different thicknesses of the layer and thus a different total volume. Therefore cuboid elements are used with a fixed thickness t and mesh-study sizes of h.

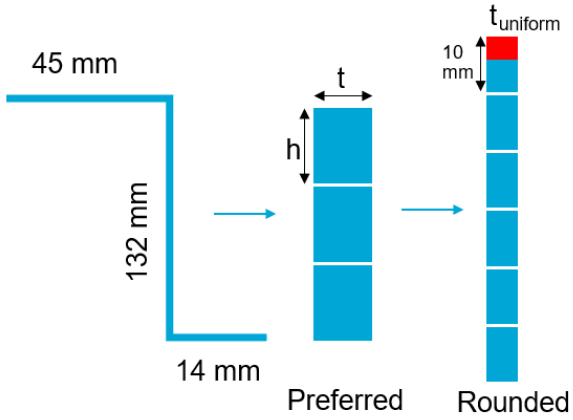

Figure 3.13: Section idealization using MOI (not to scale). Section will either be over or under approximated (red)

This thickness has to be constant for the entire model and the different mesh-sizes. So for a range in thicknesses (2-10mm has acceptable widths for aspect ratio<3), each section's preferred width is calculated. Additionally, to perform a mesh-study, all the mesh-sizes of the study should result models of equal total volumes (example: meshing a section of 169x13xt can only be meshed with sizes $h = 13, h = 6.5, h = 3.25$. Modelling it with size 5 mm will give a bigger section.). It is therefore decided to round these preferred widths to tens, allowing a study on the element mesh sizes 10 mm, 5 mm, 2.5 mm and 2 mm. For each combination of rounded widths and thickness, the section's MOI are recalculated and compared to those in Table 3.2.

Table 3.3: Final section dimensions for a thickness of 5 mm with relevant errors

	height [mm]	I_{xx} error[%]	height error [mm]	A_{CS} error[%]
Frame	150	7.61	18	30.1
Floor strut	80	2.61	20	11.1
Cargo floor	50	7.61	10	19.0
Cargo floor strut	40	-15.6	0	19.0

The combination with minimum error was a thickness of 5 mm. The corresponding rounded section heights are then as shown in Table 3.3.Unfortunately, the MOI's still deviate significantly, by which the frame and cargo-floor have become stiffer in bending and the cargo floor strut more compliant. This should be considered when comparing the crash-responses. Furthermore, the section heights are affected which could have an effect on the spatial response of the crash. However, the maximum error is 10mm on either side while the half-barrel has a radius of approximately 3000mm so it is assumed negligible. Finally, the cross sectional area of all 4 sections increased significantly, meaning the sections have become stiffer in tension or compression and the volumes are greater. It is therefore important to note that no direct comparison can be made between the thin-walled response and the idealized response. The comparison only serves in concluding on the hinge-formation similarities.

3.5.3 Material, loads and boundary conditions

In the A350-like model of Figure 3.12, the floor strut, cargo floor and cargo floor strut assigned material was Al-Li A8090 while the frame was assigned with Al-2024 [11]. Both with piecewise linear plasticity consisting of only 1 linear plastic step. Modelling two materials for a voxelmesh would be rather complicated and with the similar Young's moduli and yield stress (73.1 - 71.7 GPa and 324-370 MPa respectively), only one material model will suffice. Al-2024 has been chosen since the frame was found to be absorb most energy in literature (see **??**). The material properties of the piecewise linear-plastic Al-2024 has been presented below in Table 3.4. The last four rows corresponds to the 2 points of the piecewise-linear stress-strain curve.

Table 3.4: Al-2024 material properties as used in [11]

	Value	unit
ρ	2780	kg/m3
E	73.1	GPa
ν	0.33	
σ^{yield}	324	MPa
ϵ^{yield}	4.43 $*10^{-3}$	
σ_{max}	558.11	MPa
ϵ^{p}_{max}	0.166	

Assumption number 3 led to the rigid body coupling constraint substituting the cabin and floor (see Figure 3.14. This rigid body is constrained to only translate along z, removing any rotation. As a result, the experienced acceleration is uniform along the cabin width with a

value similar to the seat closest to the frame. However, rotation of the floor would dissipate energy elsewhere, so the experienced forces can be greater meaning it is conservative. A rigid wall has been used to model the floor for contact analysis, using sliding with friction coefficient of 0.5. A symmetry constraint has been imposed to limit the model size, where again only translation along z is allowed.

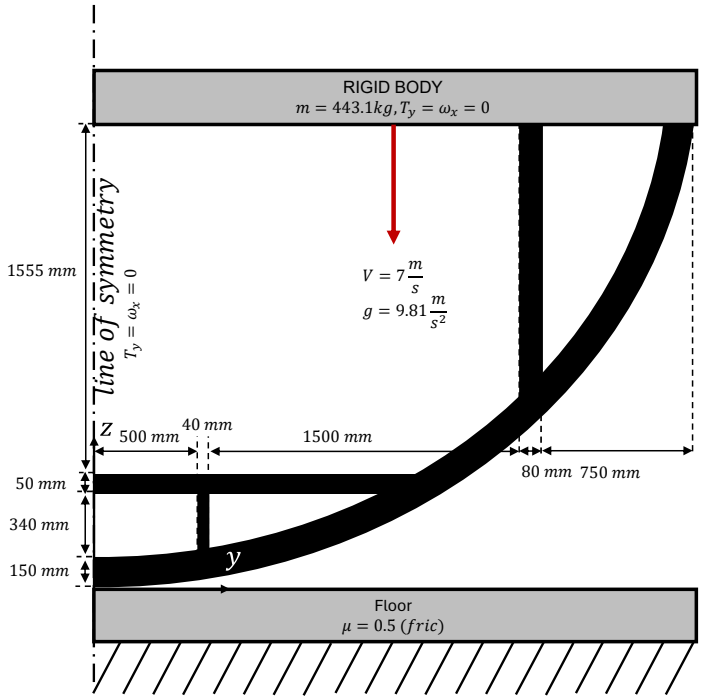

Figure 3.14: Half-barrel, sub-floor, single frame schematic of the A350-like aircraft with loads, symmetry and boundary constraints

A gravity load and initial velocity are imposed on the entire model, including the rigid body. The velocity should be 7 m/s with a total mass 1/6th of 2658.7 kg since only 1 frame is modelled here alternative to 6 in [11] (neglecting the single frame mass of Figure 3.14). This mass was distributed over the cabin floor and cargo floor, but to later include the cargo-hold in the design space, all mass has been moved to the cabin floor for consistency. Fully integrated shear-locking free solid elements (Isolid=18, Radioss), with full geometrical-non-linearities, have been used in Altair Radioss using explicit non-linear analysis. The final mesh-size will then be used and checked for reduced integration applicability.

Chapter 4

Bending Energy Results

In this chapter, the bending energy formulations have been tested on the compression beam using the HCA method. The goal was to compare the energy-absorption capabilities to find the optimized formulation. First, the implementation of the HCA algorithm has been verified using the standard case. Next, the comparison of the different L-IED formulations are presented. To optimize the formulation even more, the contributions of the two halves have been manipulated. This can be found in the preference study. Finally, the alternative stress function formulation have been shown.

4.1 HCA verification

The compression beam test case, presented in subsection 3.2.3, has been used to verify the correct implementation of the HCA algorithm and the integration of the software packages (Radioss and Compose). Only the standard algorithm is tested of which the results have been extracted from Bandi et al. [16] for comparison.

By doing so, the compression beam modelling in Radioss and its symmetry replacement can also be verified. Four potential causes for discrepancies are given below:

1. The proportional gain had not been presented, which thus needed to be found.
2. the Von-Neumann neighborhood definition has been used instead of the Moore (see Figure 2.15).
3. Finally, the piece-wise linear plasticity curve has been replaced by a Johnson-Cook model.
4. As mentioned earlier, material interpolation cannot be included for shell elements in Radioss.

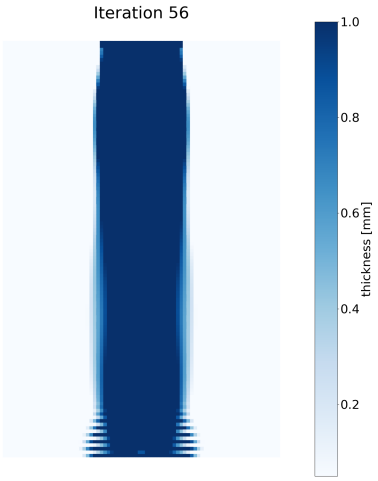

Figure 4.1: Topology solution (mirrored) for the standard HCA method applied to the compression beam

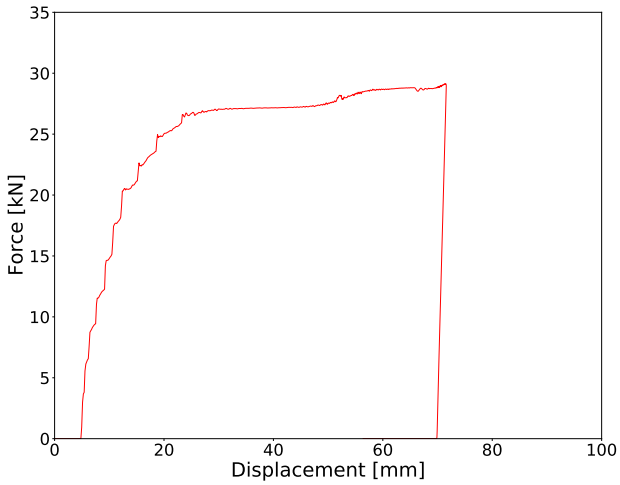

Figure 4.2: Force displacement curve of the compression beam's final topology solution (force doubled for symmetry)

The magnitude and profile of the force displacement curves shows good agreement. Although, the time increment for data-sampling was far more larger as can be seen from the loss in smoothness. The designs also slightly differ but that can be explained by the different neighborhood definition or the different found proportional gain.

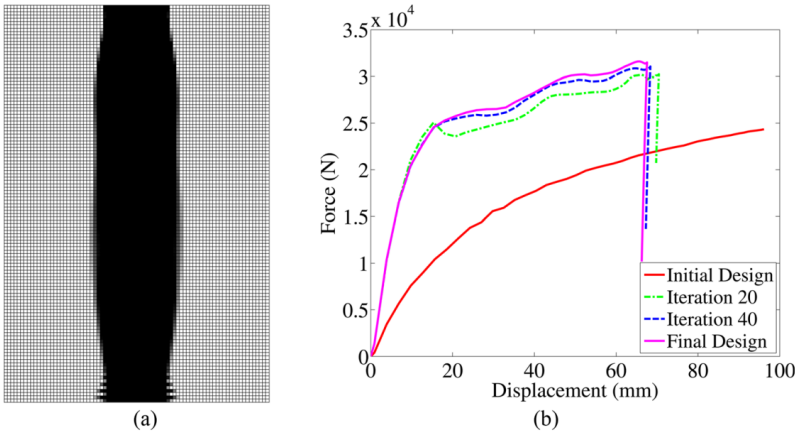

Figure 4.3: Verification results from Bandi et al. [16] for the compression beam using the standard HCA framework

The implementation has been verified successfully, considering the changes made.

4.1.1 Inter-level gradient approximations verification

Obviously, the dynamic non-linear nature of crash-analysis would better use the full Lagrangian strain derivation in the derivation of element' bending energy. Large plasticity (or plasticity gradients in thickness/density gradients) are non-linear, resulting in lower accuracy on the true bending energy with the linear approximation. Nevertheless, the small strain assumption has significantly reduced the complexity of this framework, with the majority of the energy being consistent with the bending deformation. In this section, verification of the inter-level gradient approach is performed.

Identified inconsistencies

Two cases have been identified where non-representing energies were found in the linear approximation using the neighboring elements (inter-level) field variables.

1. Density gradients in bending

2. Stepped thickness/density gradients in bending

Firstly, it has been shown in Appendix A that material interpolation in density gradients can alter the severity and possibly orientation of the stress-gradient. As a result, the computed bending energy can be erroneous. The correction presented in subsection 3.4.2 ensured these gradient are correctly in line with the intra-level loading.

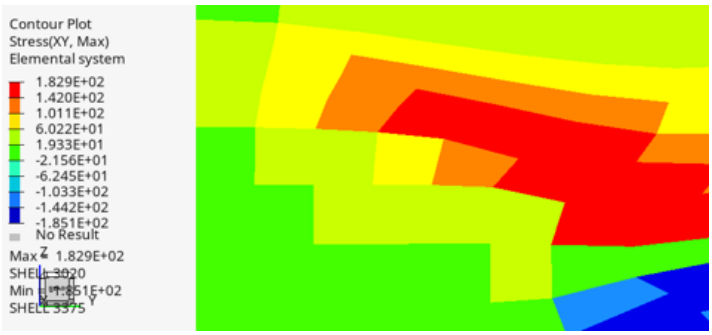

Figure 4.4: Shear stress in the shear-deformed stepped thickness gradients

Secondly, for stepped thickness/density gradients in bending, not only the stress gradient approximations are inconsistent, but even the inter-level strain gradients can be out-of-line with the intra-level deformation and bending energy. Thinner/softer elements in stiffer corners deform in shear, creating strain and stress discontinuities (see Figure 4.4). Additionally, the stiffness discontinuity is worsened after the thinner elements enter the plastic regime, lowering their relative stiffness even more.

The latter inconsistency thus remains in this framework. However, the effect might be negligible on the total bending energy, since the induced (or non-representative) shear stress and strain gradients might compensate for the actual (intra-) bending energy. These shear gradients are namely consistent relative to each other.

Intra- and inter-level gradients and bending energy comparison

Ideally, to compute the intra- and inter-level strain and stress gradients of the bilinear 4-node elements, the corner date of full integration is used. Unfortunately, these corner values cannot be exported in Radioss.

Alternatively, in subsection 3.3.2, the derivation of the strain gradient led to one where the gradients are a function of the nodal displacements. Appendix C verifies the reconstruction of the true strains from the true displacements when neglecting rotation and the non-linear shear terms.

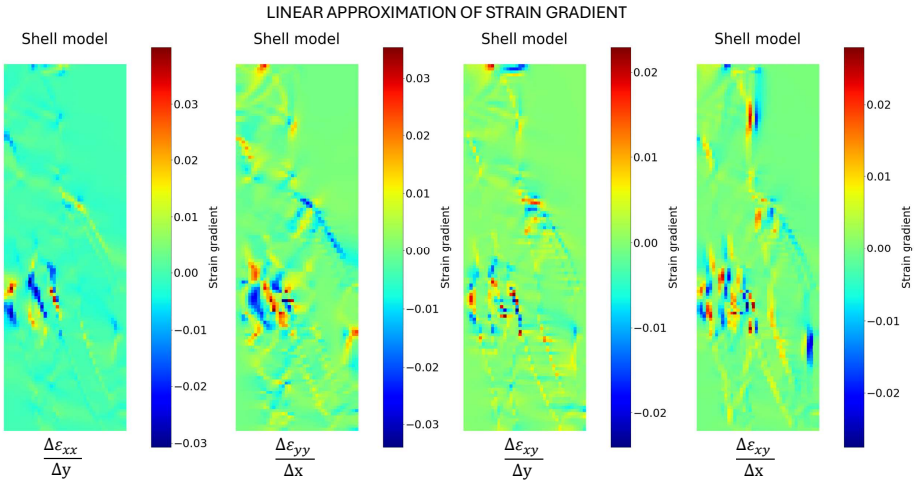

Figure 4.5: Inter-level linear strain gradient approximation at peak internal energy for the solution of L-IED2 (Figure 4.19)

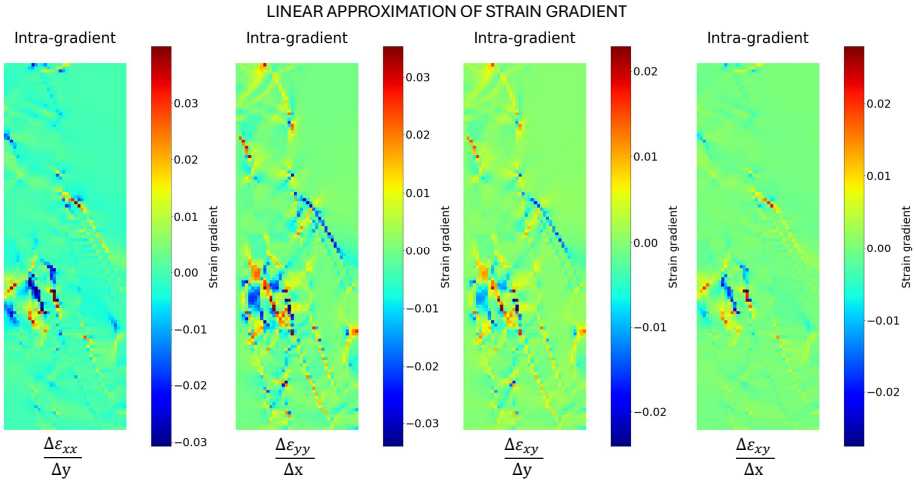

Figure 4.6: Intra-level linear strain gradient approximation at peak internal energy for the solution of L-IED2 (Figure 4.19)

The intra- and inter- level strain gradients show good agreement, although the intra-gradients indeed differs along the edges of the sharp design in Figure 4.19, correlating to the thickness

gradients. More local peaks are found for the intra-level strain gradients of xx and yy, while indeed the stepped regions show less variations in the xy figures.

In Appendix D, a formulation has also been presented for the stress gradient based on the strain gradients. These two combined would allow for the computation of the intra-level bending energy reconstruction. Figure 4.7 and Figure 4.8 are presented below for inter- and intra-level bending energy. As is clear, the overall distribution of the bending energy is quite consistent. The stepped regions is indeed not affected by the strain discontinuities. Intra-level does create localized peaks, as is expected for the smaller scale.

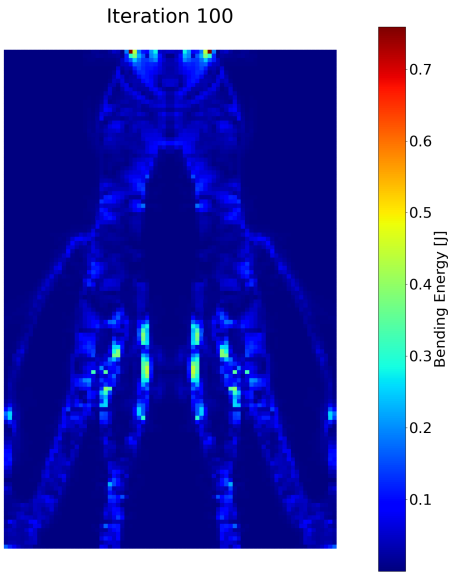

Figure 4.7: Intra-level linear bending energy at peak internal energy for the solution of L-IED2 (Figure 4.19)

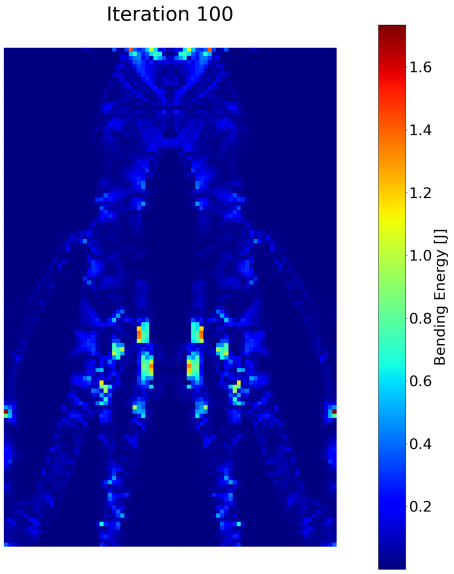

Figure 4.8: Intra-level bending energy at peak internal energy for the solution of L-IED2 (Figure 4.19)

However, the magnitude is little over a factor two larger. This could be due to the chosen time discretization in the stress gradient computation (Appendix D) or since an offset in the strain gradient propogates further in the stress gradient. Nevertheless, the algorithm normalizes the energies with the average (as will be explained in subsection 4.2.2).

4.1.2 HCA necessity verification

When the intra-level bending energy above would be used, the only function of the cellular automata approach would be to average the energies and thicknesses. However, as was explained in subsection 3.3.3, such a small level of detail can be unstable or result in very thin sections of only 1 element wide. For reduced-integration elements, the response would become nonphysical.

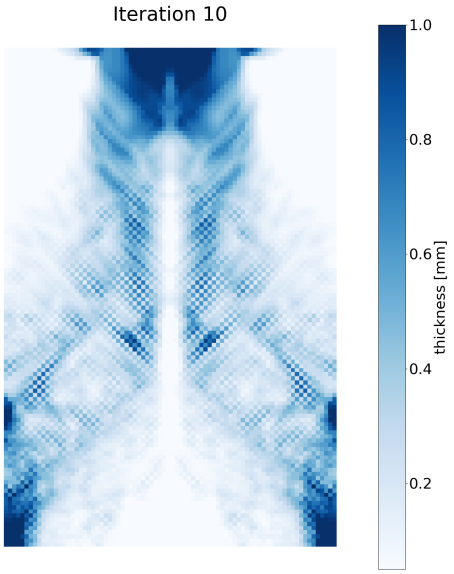

Figure 4.9: Intra-level L-IED2: Checkerboarding in the topology solution (mirrored)

To prove this, the gradients have been computed as such instead of extracting them from the neighbors. As expected, optimizing this quantity from such local levels is impossible. Figure 4.9 demonstrates the unstable and non-physical checkerboarding result of such a methodology. Bending and 1 element cannot go hand in hand. Therefore, not only is the HCA necessary in communication the field-variable (bending energy) states, it is even necessary in deriving the states for better stability and wider sections. For comparison, the same iteration (using same control and averaging parameters) of inter-level LIED-2 is given in Figure 4.10.

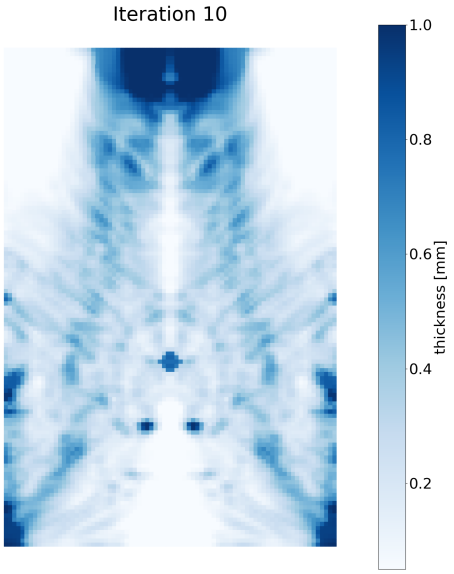

Figure 4.10: Inter-level L-IED2

4.2 Resolution and control modifications

The FEM model and the HCA framework are now used for the bending energy formulation. This section presents the modifications needed to reach convergence for the 4 formulations of the IED (presented in subsection 3.3.4) within the whole bending energy functions of Equation 3.37 and Equation 3.38.

4.2.1 Averaging modification

In the standard HCA example, averaging was not only applied on the field variable (IED), but also on the design variable (thickness). Averaging of the bending energy had been implemented, however, thickness averaging results in similar topology solutions for all 4 L-IED. Each returning a single diagonal column under bending, as can be seen in Figure 4.11. This is because the mesh size was too coarse to return multiple bendable sections. The baseline turns-off averaging if the convergence criteria reaches a certain value (48) to attain a 'crisp' solution [16], however the columns would become hollow again and strain away from convergence. Averaging thus had initially been turned off fully, to which some design would run into solver issues (squeezed elements that decrease the time-step for example), causing L-IED-2 and 3 to be stuck at iteration 66 and 54 respectively. Moreover, Some sections are only 1 element wide, causing reliability concerns of their stiffness in bending.

Therefore, to keep the same mesh-size, thickness averaging has only partially been removed by scaling the influence of the neighboring elements to an arbitrary number of 0.025. In other

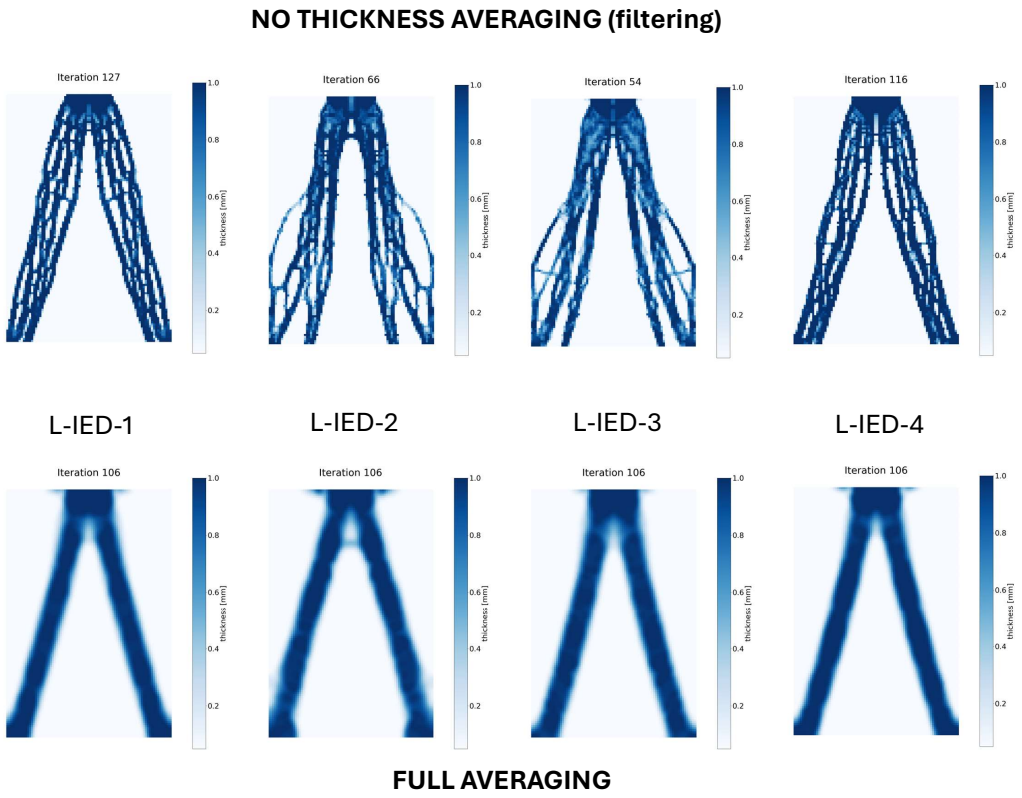

Figure 4.11: Topology outputs for the 4 L-IED functions using full averaging or no averaging (for a $K_p = 0.05$ in Equation 4.1)

words, the element thickness is dictated for approximately 10% by its neighbours. Larger values have been tried as well and were found too large for this mesh-size to have a significant effect.

$$\overline{x}_i = \frac{x_i + \sum_{j \in N_i} 0.025 x_j}{0.025 N_i + 1}$$

4.2.2 Control-gain modification for Convergence

The bending-energy optimization algorithm behaves rather different from the standard HCA algorithm. Several key-events can be identified for the Bending-Energy HCA.

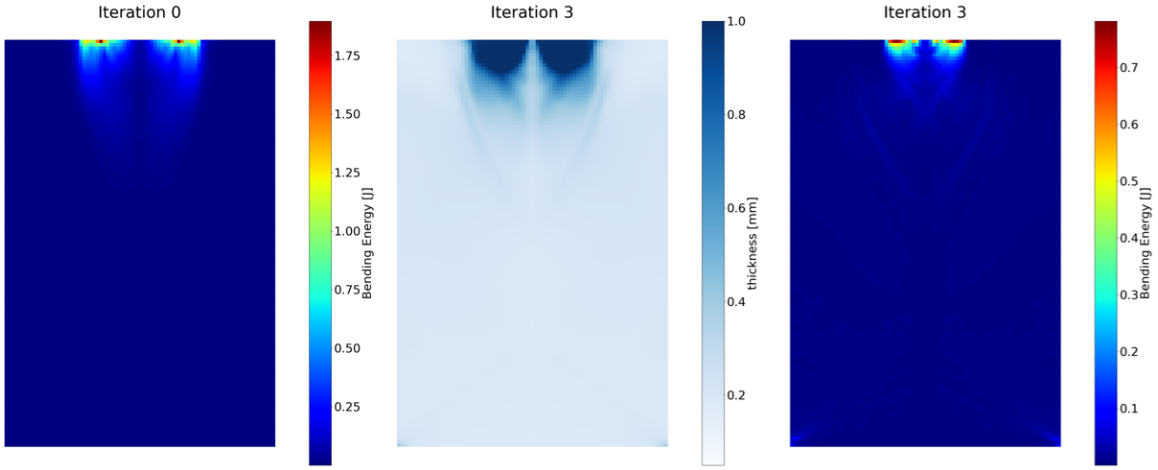

Figure 4.12: Bending Energy (for L-IED-4) for the uniform thickness distribution of 0.3mm (left), the fortification of the site-of-impact (middle) and the corresponding Bending energy (right)

1. First, the uniform distribution (input=0.3) of the field variable absorbs significant amount of energy through bending, presented in Figure 4.12 (left). In the initial reorganisation, the site or impact is fortified (middle) and non-bending regions are removed, causing the bending energy to plunge (right, check energy bar range).

2. Once, the site of impact has been formed, the material between the floor and site-of-impact slowly takes its shape and bending energy gradually increases with it.

3. Oscillation of the thickness changes and bending energy.

This third point is discussed below in more detail.

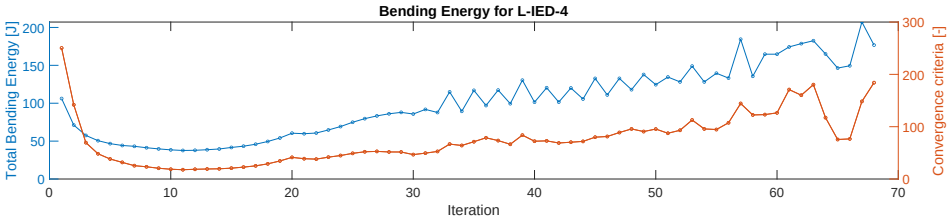

Figure 4.13: Energy and convergence criteria evolution for L-IED-4 using a relatively stable value of $K_p = 0.0016$ in Equation 3.2(without thickness averaging for clarity)

It was found that the constant proportional control gain (presented in section 3.2) was insufficient in reaching convergence for a bending-energy governed structure. As a topology becomes more defined/sharper (elements reaching the minimum density or maximum), the crash energy can become concentrated in a few local regions (Figure 4.14), drawing the bending-energy away from previously formed regions (Figure 4.15). These high-energy regions resemble plastic hinges while the solution is far from converged (many intermediate densities present). Although hinges are desired, the convergence will not be reached due to oscillation in the

design: The high-energy local regions are fortified at the cost of other regions. The above explanation can be drawn from the energy and convergence criteria plot in Figure 4.13.

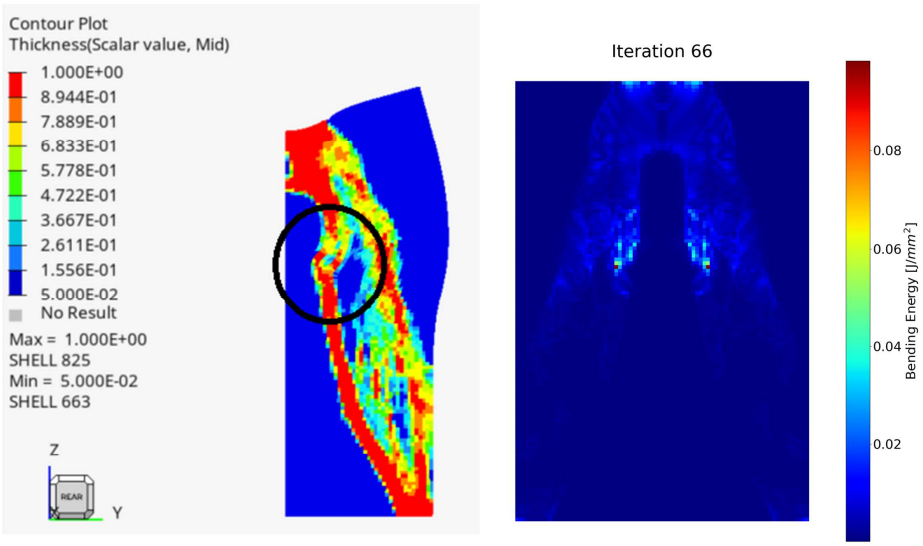

Figure 4.14: Local bending deformation in an non-converged design (for L-IED-4 $K_p = 0.0016$ without averaging)

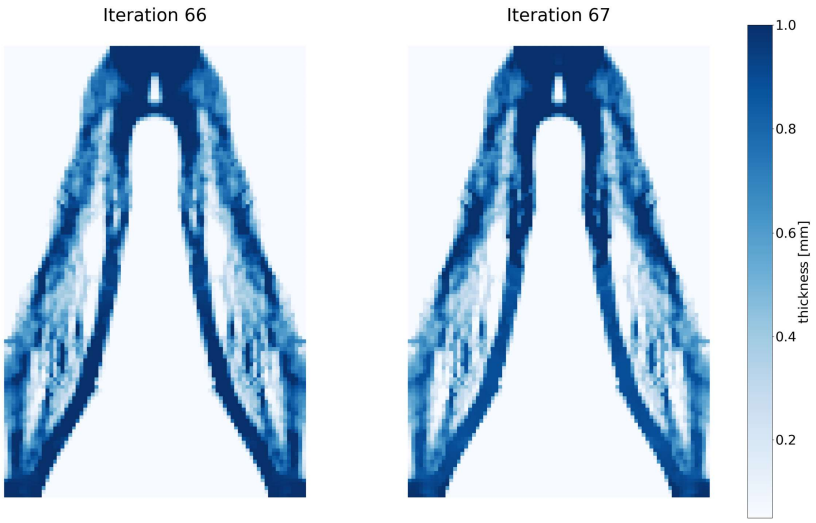

Figure 4.15: Oscillation of thickness due to the local bending deformation presented in Figure 4.14 without control gain modification for L-IED-4 using $K_p = 0.0016$ (not converged)

A smaller control gain can be used to reduce the severity of the oscillation, at the cost of more number of iterations (and thus more non-linear analysis'). Another option would be constraining the maximum change of density of each element. However, oscillation cannot be avoided once local-failure occurs, as the energy absorbing hinges drive the target bending energy up resulting in the removal of existing structure. Therefore, once the algorithm has reached this point, a different formulation of the objective is required. For a fair comparison of the four L-IED functions, a single modification is used that was easy to implement.

The proportional control gain parameter has been made inversely related to the average error between the bending energy and the target for all iterations. Equation 3.2 is altered to:

$$\Delta x_i^{(k)} = K_p \frac{\left(\overline{S}_i^{(k)} - S^{*(k)}\right)}{\frac{\sum_{i=1}^{n}\left(\overline{S}_i^{(k)} - S^{*(k)}\right)}{n}} \tag{4.1}$$

When the design sharpens and the total (and average) bending energy increases, the target bending energy $S^{*(k)}$ increases and as a result the error of any (small or) non-bending element increases. The error of each element is thus normalized to the average error, such that the total change in density between iterations is less affected by the individual responses, reducing or even eliminating the likelihood of diverging.

Alternatively, new local control rules can be formed (such as local bending-targets) or the history in density of each element is tracked. However, due to the higher complexity in implementation (determining new rules, mass control, zone-identification), this can be done in the future.

Finally, the convergence tolerance and its criteria have been altered as well. To filter out the remaining oscillation between iterations, the error is computed as the average net change over the period of two iterations. With the averaging and control gain modifications put in place, the design are less susceptible to divergence and oscillation dampens out, as can be in Figure 4.16 (Using L-IED-4 for example). The bending energy does reduce over time compared to the solution without any averaging and control gain alteration in Figure 4.13. This is due to detail loss caused by averaging, when comparing Figure 4.16 and Figure 4.17. A higher level of detail has more smaller sections which are easier to bend causing a higher (possibly non-physical) bending energy.

$$\sum_{i=1}^{n} \frac{1}{2} |(\Delta x_i^{(k)} + \Delta x_i^{(k-1)})| < \delta$$

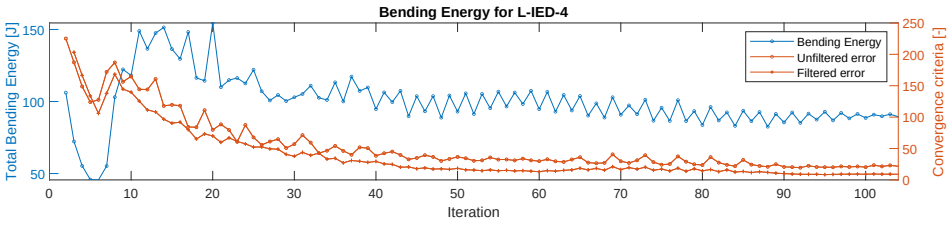

Figure 4.16: Thickness averaging: Energy and convergence criteria evolution for L-IED-4 using the modified control gain function of Equation 4.1 with a relatively stable value of $K_p = 0.05$

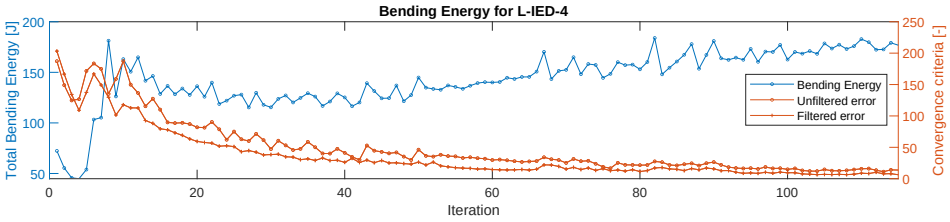

Figure 4.17: No thickness averaging: Energy and convergence criteria evolution for L-IED-4 using the modified control gain function of Equation 4.1 with a relatively stable value of $K_p = 0.05$

The corresponding tolerance δ has been increased with a factor of 4 from 6.4 to 25.6 (approximately a global thickness change of 0.5%) due to the higher detail under less thickness averaging.

4.3 L-IED Comparison

With these modifications in place, the 4 formulations have been compared in terms of geometry and response.

4.3.1 Topology solutions

The four models converged after 45, 100, 63 and 43 iterations in the order of L-IED-1 to 4. Since L-IED failed to converge as soon, all of the solutions have been compared for iteration 100 as well.

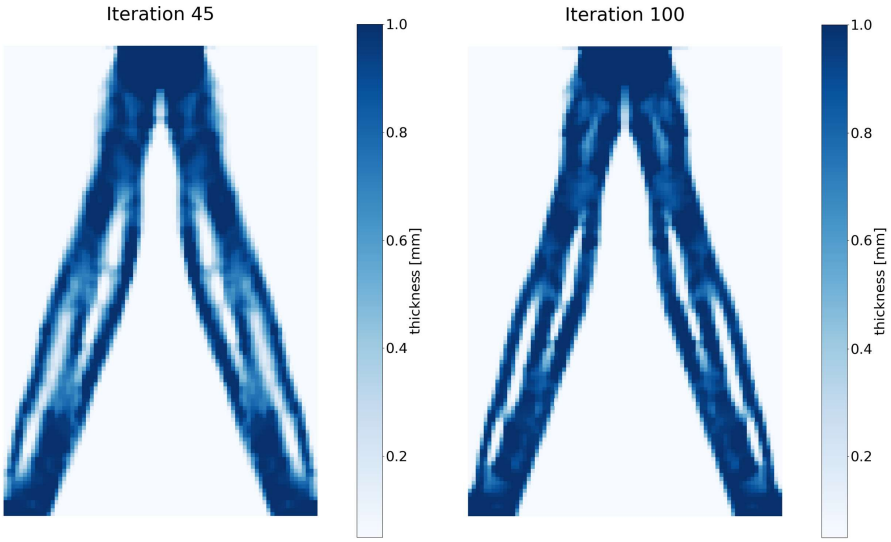

Figure 4.18: L-IED-1 topology solutions for the larger convergence criteria (left) and for iteration 100 (right)

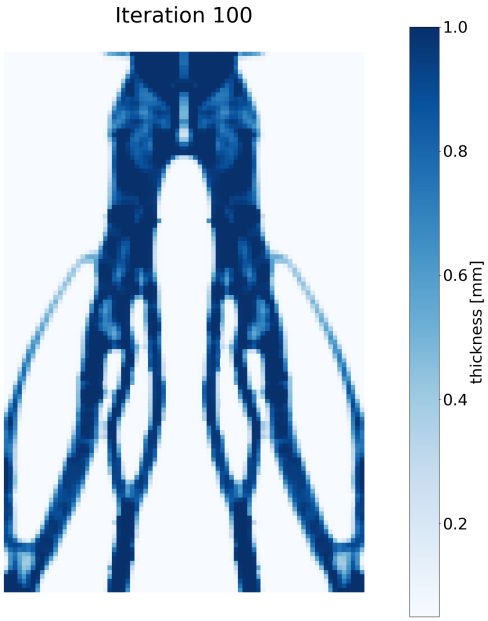

Figure 4.19: L-IED-2 topology solutions for the larger convergence criteria

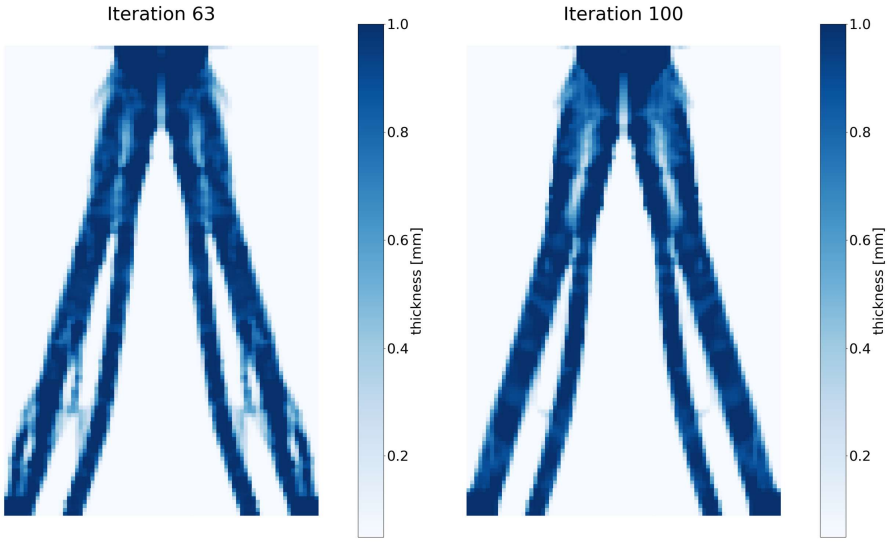

Figure 4.20: L-IED-3 topology solutions for the larger convergence criteria (left) and for iteration 100 (right)

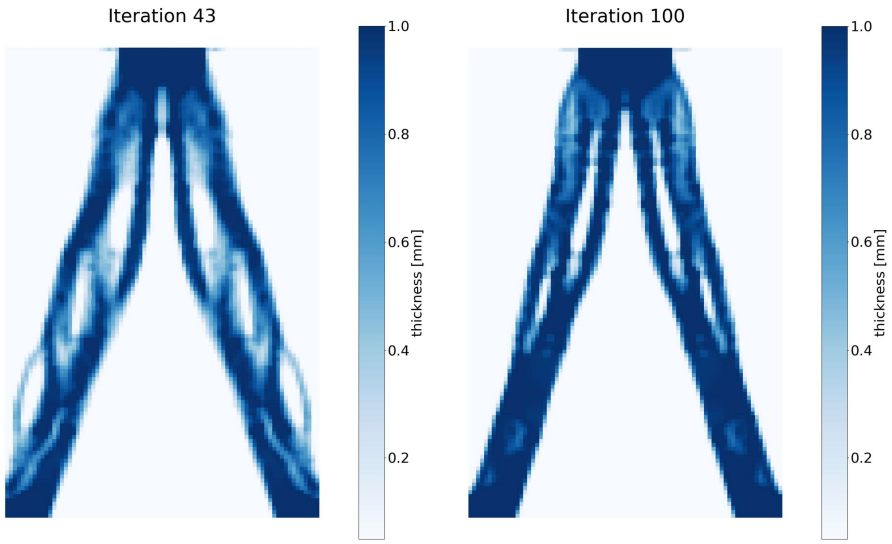

Figure 4.21: L-IED-4 topology solutions for the larger convergence criteria (left) and for iteration 100 (right)

Most solutions did not change much after the large convergence tolerance had been met, except L-IED-3. The effect of partial averaging can be seen when comparing the solutions to those in Figure 4.11. Some detail is lost compared to 0 thickness averaging (top), while the level of detail is far more greater than full averaging (bottom). Partial thickness averaging did result in some intermediate densities (lighter blue) inside thicker sections. These are undesired and ultimately removed. However, either full thickness averaging needs to be applied or no-averaging. The latter will give very questionable coarse designs, thus for a greater mesh size, averaging will be the solution. For the relative comparison, the influence of the intermediate densities are assumed negligible.

Returning to the expectations of these four approaches (subsection 3.3.4) to half of the full bend equation:

- L-IED-1: Considered the real bending-energy approach
- L-IED-2: Single-bend maximization approach: expects to return sections with 1 main bend direction throughout the full impact to promote hinge formation.
- L-IED-3: Single-loading maximization approach: expects single-bending sections with additionally unidirectional-loading throughout the full impact (bend in one direction with only growing (no sign flip, either positive or negative) compressive/tensile/shear stresses and strain)
- L-IED-4: L-IED-3 until plasticity: expected to be similar to function 1 while neglecting elastic spring-back.

Figure 4.18 (L-IED-1) and Figure 4.21 (L-IED-4) do indeed look similar. Figure 4.19 and Figure 4.20 are both composed of multiple paths running to the ground, possibly stemming from prioritizing the outer elements of a section under bending (removing the inner elements). The difference between these latter two in formulation is also visible, where L-IED-2 allows sign-changes in the stresses and strains by only considering the gradient direction during the full response. Once an element bends under compression, the compressive normal forces move towards the positive side. L-IED-3 would avoid eliminate these 'unloading' elements while L-IED-2 promotes these higher gradient elements. The curvier section showcase this, while L-IED-3 has rather straight sections with a slight curve in one direction.

4.3.2 Crashworthiness

The Force-displacement curves have been plotted together with the plastic energy curve. What is immediately noticeable is that the responses are not significantly better than the straight column of the baseline. Initially it was believed that this was due to the absence of material interpolation in my shell model. However, this has been disproven in Appendix B. The peak forces are almost as high as the baseline and the final plastic energy is surprisingly the same.

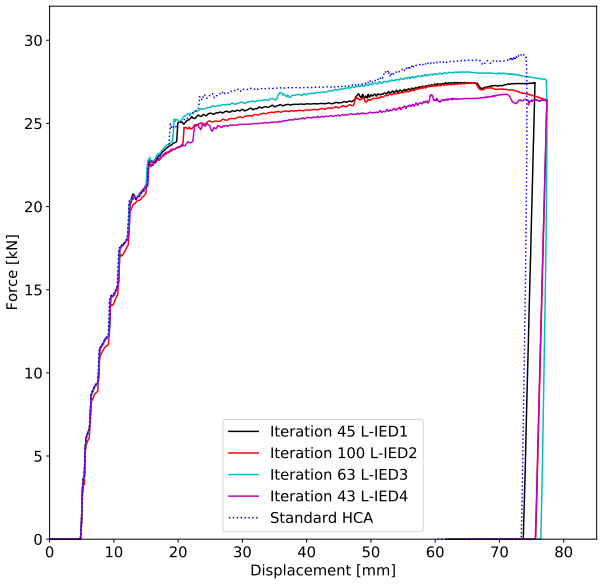

Figure 4.22: Force-displacement curves of the 4 L-IED formulations (within the total bending-energy functions) for the converged iterations

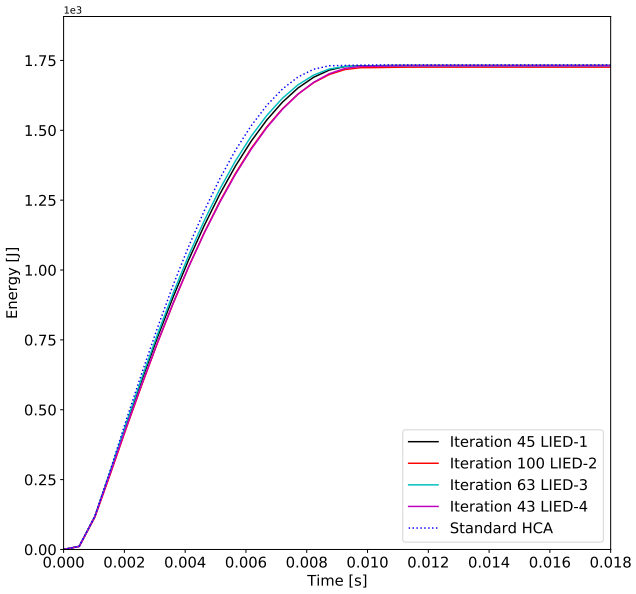

Figure 4.23: The plastic-energy profiles of the 4 L-IED formulations (within the total bending-energy functions) for the same iteration

The inability of all formulations to significantly reduce the peak stress and increase the dissipated energy could stem from the objective formulation. Fortifying high-bending regions makes the design strong enough for the specific load case. Alternatively, a variable target can be set that does not stiffen regions with large bending-deformation.

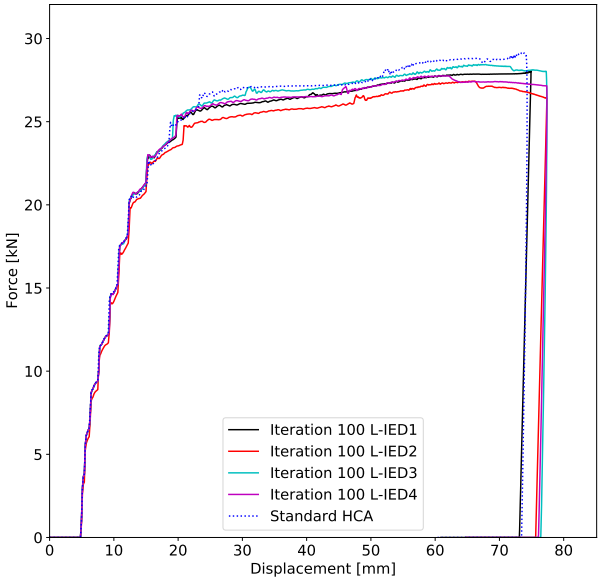

Figure 4.24: The force-displacement curves of the 4 L-IED formulations (within the total bending-energy functions) for the converged iterations

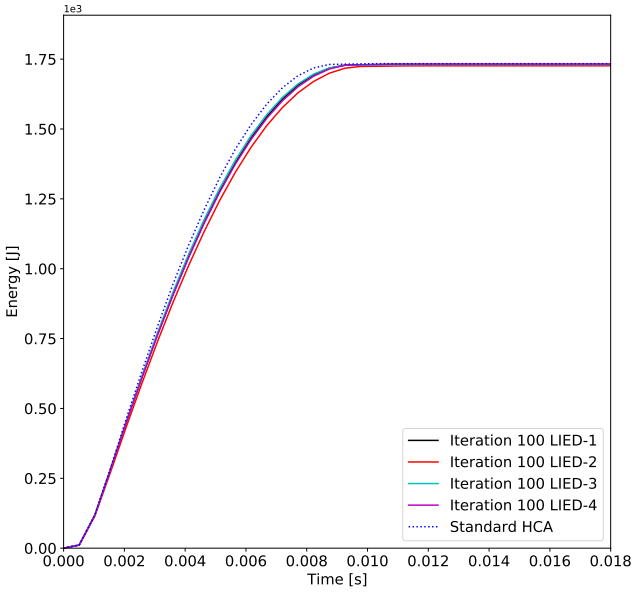

Figure 4.25: The plastic-energy profiles of the 4 L-IED formulations (within the total bending-energy functions) for the same iterations

4.3.3 Conclusion

The objective of uniform bending-energy distribution does give new topology solutions, but the overall performance is the same. The same amount of energy is captured for this load-case, although this energy is now distributed in bending instead of only compression.

Nonetheless, it can be concluded that bendable-sections are formed using a bending-energy quantity. When increasing the load, hinges can (and will) be formed compared to thick column of the standard HCA algorithm.

Moreover, the different formulations do meet the expectations. The single-bend maximization (L-IED-2) is most likely to form multiple plastic-hinges for an increased load. On this ground and due to its lower peak load, L-IED-2 has been used in the subsequent sections.

Recommendations chapter: Optimize for smaller impact, test on required impact Variable target to avoid stiffening bending regions of above average energies (but under bending limit)

4.4 Preference study

The full bending energy equation does not only include the L-IED function (L-IED-2), but also the quadratic part (Q-IED). This part stem from the (assumed) linear stress and strain gradients. Its relative presence has been small (1/24 compared to 1/4 for L-IED in Equation 3.37). However, the final magnitude difference is not 6 but in the range of 10-30. This section studies the effect of function weight manipulation on compliant design.

By weighting, either the L-IED function or the Q-IED function receives a factor. Although this alters the total energy, the normalization of the energy offset (to the objective (Equation 4.1) makes convergence and stability unaffected. Therefore, the K_p value can be kept at 0.05, which helps limit this study.

$$\begin{aligned}\Delta U_{Bend,xx} = A\frac{1}{24}\left(\left(\frac{d\sigma_{xx}}{dy}\right)_i + \left(\frac{d\sigma_{xx}}{dy}\right)_{i-1}\right)\left(\left(\frac{d\varepsilon_{xx}}{dy}\right)_i - \left(\frac{d\varepsilon_{xx}}{dy}\right)_{i-1}\right)th^4 \\ + B\frac{1}{4}\Bigg(\left(\left(\frac{d\sigma_{xx}}{dy}\right)_i + \left(\frac{d\sigma_{xx}}{dy}\right)_{i-1}\right)(\varepsilon_{xx,y=0_i} - \varepsilon_{xx,y=0_{i-1}}) + \\ \left(\left(\frac{d\varepsilon_{xx}}{dy}\right)_i - \left(\frac{d\varepsilon_{xx}}{dy}\right)_{i-1}\right)(\sigma_{xx,y=0_i} + \sigma_{xx,y=0_{i-1}})\Bigg)th^3\end{aligned}$$

On average, for (A=1,B=1), the final energies differ by a factor 10-30 (including the factors 1/24 and 1/4). Therefore, A is increased by steps of 20.

4.4.1 Topology Results

The results have been presented below from only L-IED (A=0, B=1) to only Q-IED (A=1, B=0) in increasing A. The normal solution (A=1, B=1) from Figure 4.19 is added again for completeness.

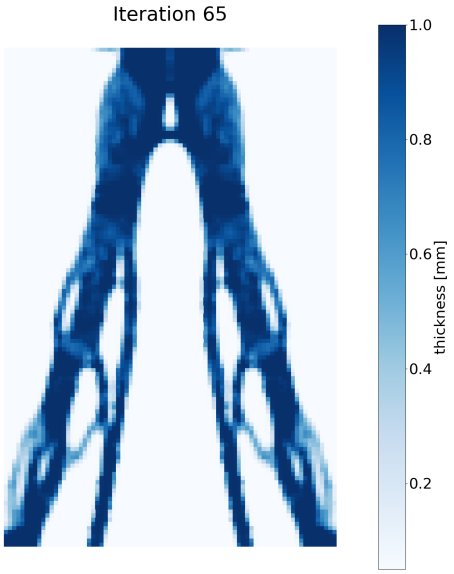

Figure 4.26: Preference study solution (A=0, B=1): only L-IED

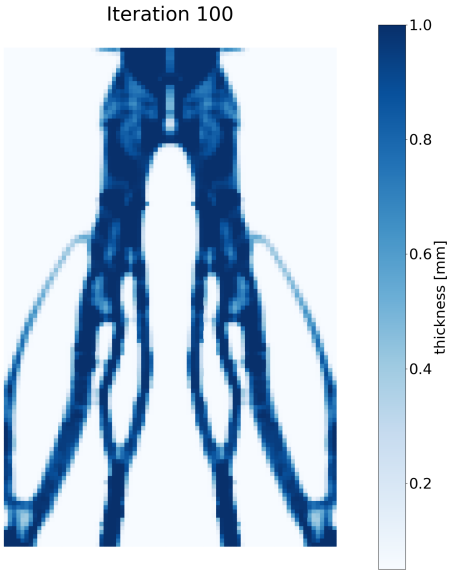

Figure 4.27: Preference study solution (A=1, B=1): no factor manipulation

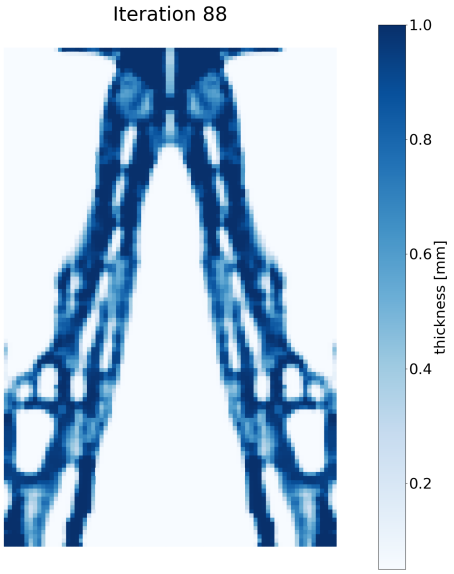

Figure 4.28: Preference study solution (A=20, B=1)

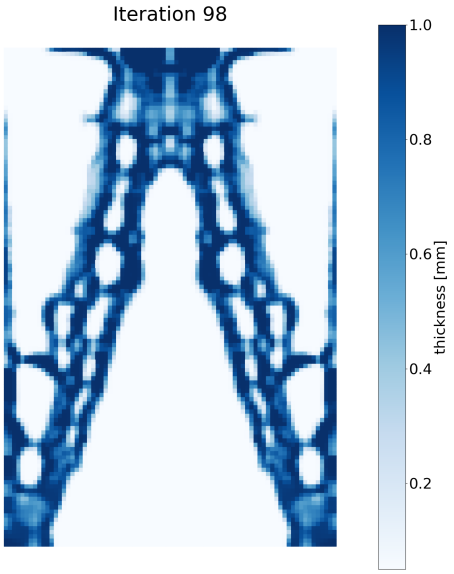

Figure 4.29: Preference study solution (A=40, B=1)

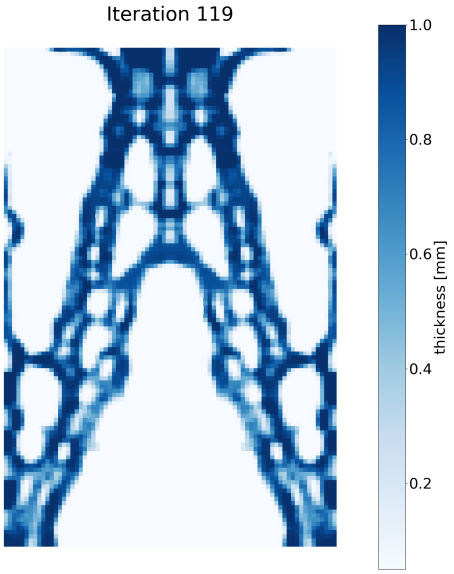

Figure 4.30: Preference study solution (A=60, B=1)

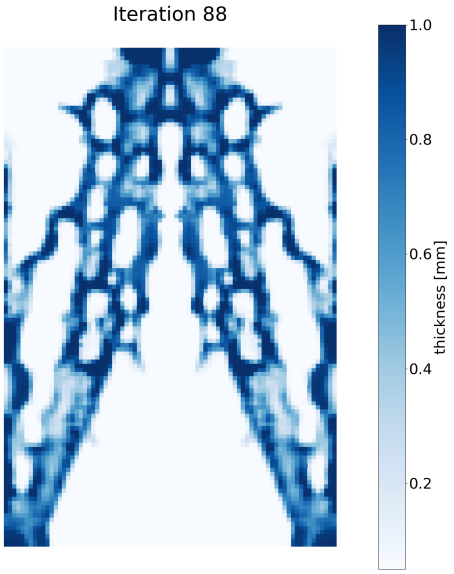

Figure 4.31: (no-convergence) Preference study solution (A=80, B=1)

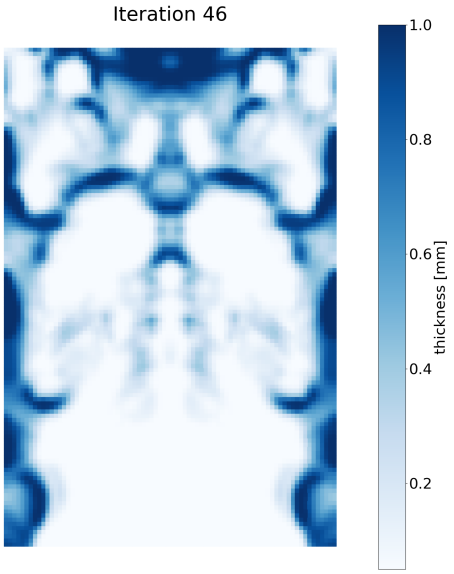

Figure 4.32: Preference study solution (A=1, B=0): Only Q-IED (not converged) showing de-facto hinge characteristic

As is clear, for increasing A the number of hollow regions (called bubbles henceforth) increases. Additionally, for the highest values of A, spurious mass is gathered along the edge. Looking at Figure 4.32 might explain why.

When B=0, only the Q-IED function is present in the function. This quantity only considers both gradients and thus the magnitude of the loading (compression, tension and shear) are not taken into account. As a result, low bending elements that are in the line of load are removed. For the compression beam, this lead to a very compliant model which does not absorb energy in compression. An iteration of this run can be seen in Figure 4.32. The non-linear solver would not complete without material in the bottom half for the first 20 iterations, thus the minimum thickness had to be gradually lowered (0.15 to 0.05 in steps of 0.0025) and the thickness averaging was scaled up (0.025 to 0.2). In the end, convergence could not be reached due to the de-facto-like hinges that occurred. Considering this and the optimization modifications, this solution is not directly comparable to the other outputs. However, it is still presented to explain the progress of increasing constant A. Solution A=80, B=1 did not need the thickness degradation but the inability to reach convergence was evident here too.

The effect of the Q-IED functions thus leads to the formation of bubbles and material moving outward from the line-of-loading. This is why intermediate factors include spurious materials on the side which are barely loaded. The reason the stress and strain gradients are both non-zero is a direct result of using a continuous mesh. As thick material bends outward, the 'deleted' elements are pushed outward as well. It is recommended for future work to implement an effective element removal framework, which allows element reintroduction.

Whether these bubbles make the design more compliant and promote plastic hinge formation,

is discussed in the following section.

4.4.2 Response Results

In Figure 4.33, there is a clear downward trend of the peak force during crash-analysis when adding preference to the Q-IED function. However, too large of a preference (A=80 with B=1 or A=1 with B=0) and convergence is not reached or the design is almost too compliant.

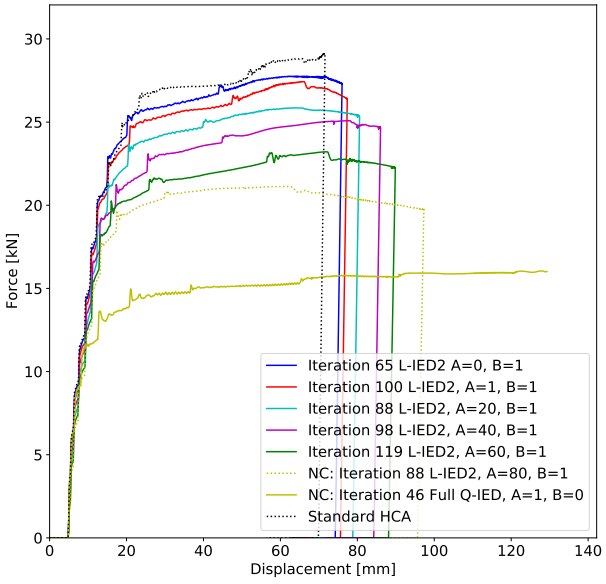

Figure 4.33: The force-displacement curves of the Preference Study for the converged iterations (and not-converged NC)

Figure 4.34 does show that the bubble-like structure deforms in bending. When looking at its plastic strain, 1 hot-spot is visible with unrealistic magnitudes. Although, this is caused by the intermediate densities in that region (see Figure 4.31), which have negligible stiffness and thus negligible influence on the response. When we filter the plastic strain, more hot-spots are visible that do lay in maximum thickness regions.

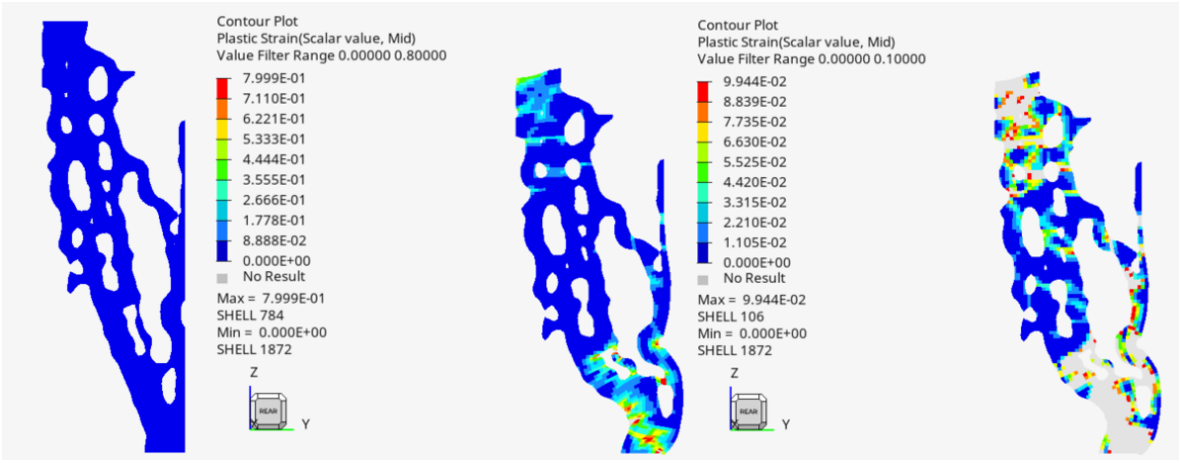

Figure 4.34: The deformed and un-deformed solution with plasticity for (A=80,B=1)[1]

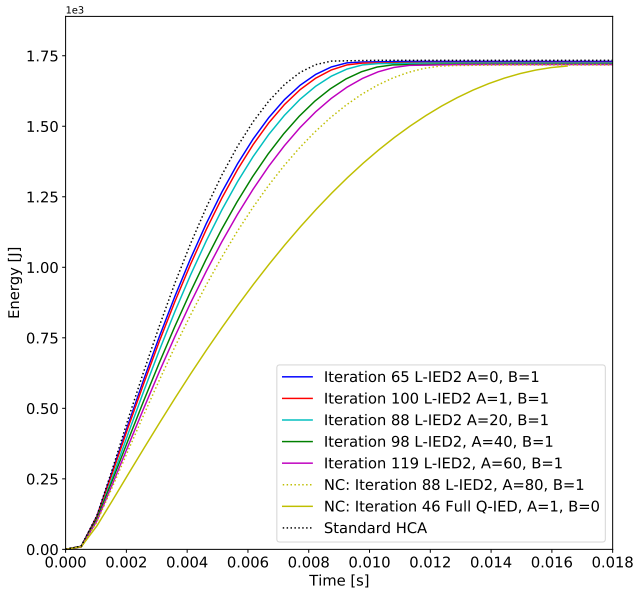

Figure 4.35: The plastic-energy profiles of the Preference Study for the same iterations

Chapter 5

Proof-of-concept (POC)

In this chapter, the results of the voxel-mesh reliability study have been presented to be able to answer the first research question. Furthermore, the outcomes of the basic HCA and the bending-optimized HCA are presented.

5.1 Idealization validation

The energy profile, acceleration profile and general damage analysis could help answer the first research question whether a voxel-mesh can give meaningful results.

5.1.1 Deformation and damage analysis comparison

Firstly, before analyzing the energies or accelerations, the deformation and possible damage has been analyzed. Damage analysis had been included using the strain limit as was done by Gransden and Alderliesten [11] ($\varepsilon_{max} = 0.166, \sigma_{max} = 558.11MPa$).

In [11] shown in Figure 5.1 below, a plastic hinge formed at A, although far less 'hinged' than point C in the A320 of Figure 2.11. Furthermore, the cargo-floor region B has some considerable plastic deformation. Location C below indicates a high stress region on the frame close to the floor spar.

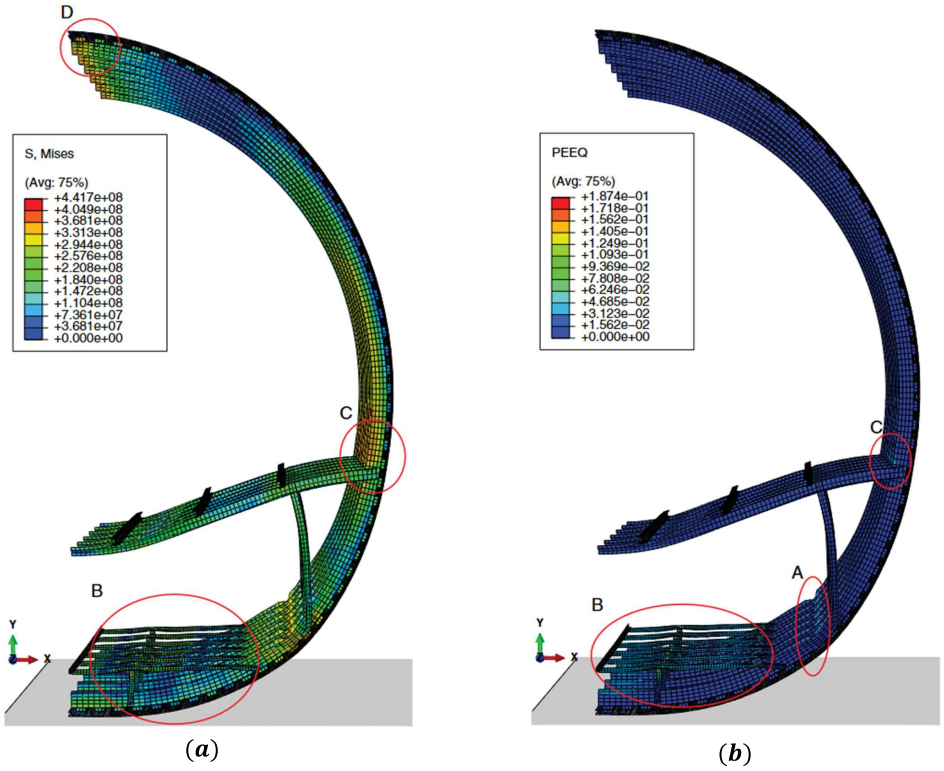

Figure 5.1: Von-Mises stress distribution (a) and plastic strain distribution (b) at maximum stress (t=0.125s) for the metal A350-like aircraft from [11]

In the voxel-mesh approximation of Figure 5.2 , the plastic hinge in the frame is missing. Region B in Figure 5.2 points at the more concentrated (compared to region B in Figure 5.1) deformation and stresses in the cargo floor region. The high stress and strain region of C is more pronounced in the image below as well although now it is below the floor spar.

The cause for this high stress at C in the voxel-mesh approximation is the rigid body replacement for the floor-cabin structure, which blocks the translation and rotation of this end of the frame. The disappearance of the hinge at A in Figure 5.1 can have the same explanation, since little rotation is allowed in the triangle construction. Instead, the stress and strain build-up in a weak spot nearby labelled with A in Figure 5.2. Hypothetically, A and C from Figure 5.1 and A and C from Figure 5.1 are related (thus the equal labelling).

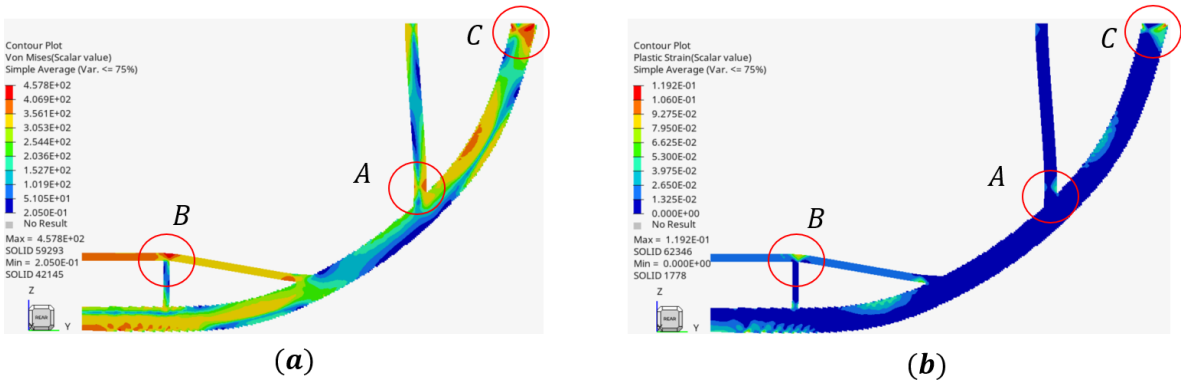

Figure 5.2: Von-Mises stress distribution (a) and plastic strain distribution (b) at maximum stress (t=0.055s) for the 10 mm voxel-mesh approximation

Above, the results for 10 mm of the voxel-mesh approximation of Figure 5.2 has been shown and discussed. A similar response was given by 5 mm and both experienced little damage. Despite that, the meshes of 2.5 mm and 2 mm fully split in the introduced stress concentrations at location C and at the root of the cargo-floor. Location A partially split for 2.5 mm and also fully split here for 2 mm. See Figure 5.3.

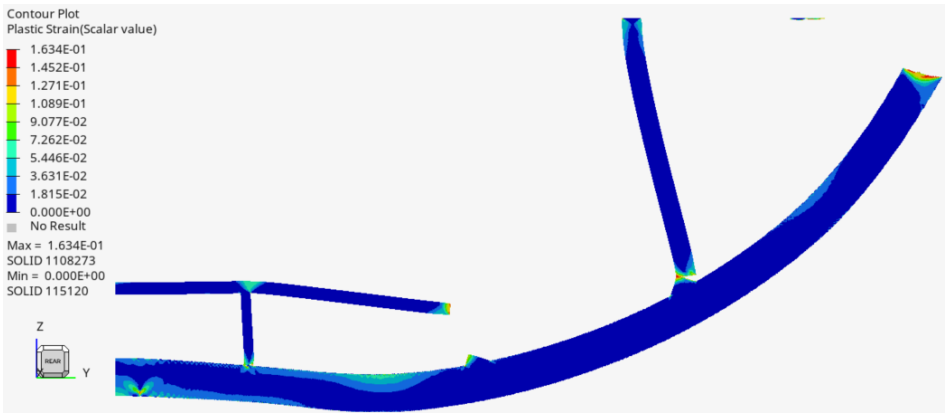

Figure 5.3: Ruptures in the 2 mm voxel-mesh approximation

Mesh-study on peak-stresses are a problem in FEM as the peak values tend to increase in refinement. Therefore, these high introduced stress-concentrations (as explained from the previous section) in combination with a very fine mesh could be the cause for crack nucleation (and thus damage progression). Gransden and Alderliesten [11] have not presented their mesh size for verification. Secondly, more energy could have entered the critical region due to:

- the absence of small-scale deformation modes (assumption 1 and removal of skin and brackets in assumption 2)
- the absence of a more compliant floor due to the rigid-body replacement (assumption 3). Figure 5.1 deformed significantly as opposed to the A320 in Figure 2.11.

Additionally, the voxel-mesh is stepped along the boundaries, creating or increasing stress concentration here.

Since damage is limited for the detailed model [11], avoiding the use of element deletion in the voxel-mesh could overcome the introduced higher stresses.

5.1.2 Energy profile comparison

The 4 mesh size models have been loaded in with a mass 1/6th of the half-barrel six-frame mass since hese represent 1 frame. To be able to compare the energy response, the normalized energies have been computed (see Figure 5.4 and Figure 5.5) and compared to those in Figure 5.6. A fair comparison can be made since the starting kinetic energies are equal.

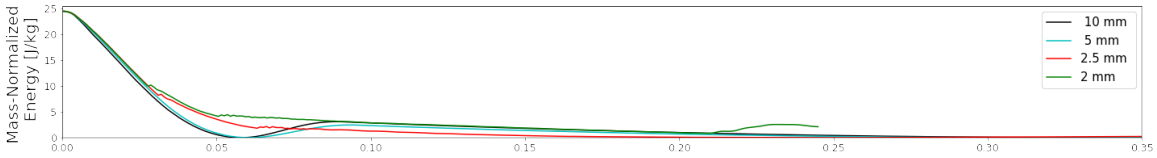

Figure 5.4: Kinetic Energy profile of the A350-like voxel-mesh approximation for different element widths (for thickness 5 mm)

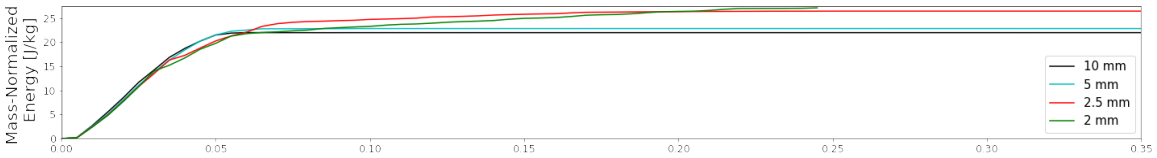

Figure 5.5: Plastic Energy profile of the A350-like voxel-mesh approximation for different element widths (for thickness 5 mm)

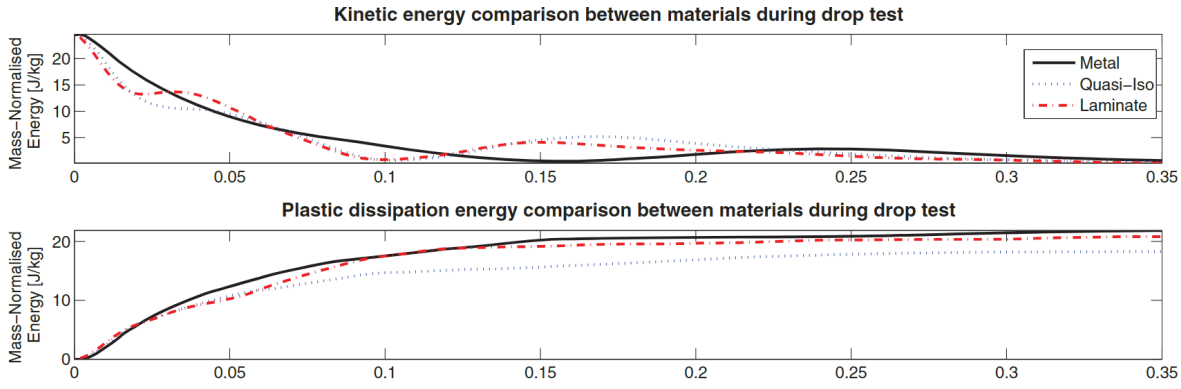

Figure 5.6: Plastic and kinetic Energy profile of the A350-like aircraft for different materials from [11]

Comparing the kinetic energy profile, it is evident that the crash-response is more elongated for the detailed baseline model (metal curve in Figure 5.6) with a duration of 150 ms before

bouncing back up. The voxel-mesh approximation for the meshes that do not rupture (10 and 5 mm) bounce back up after approximately 60 ms (Figure 5.4). This shorter crash-response can be explained by the stiffer (in bending) sections and the rigid-floor replacement. Unfortunately, as explained above, element deletion due to the high stress-concentration in critical regions caused sudden rupture for the fine meshes 2.5 and 2 mm. These curves (red and green) thus have a more prolonged crash-response, although the deformation is nowhere near the baseline (Figure 5.3 versus Figure 5.1).

The plastic energy of the baseline (metal curve in Figure 5.6) amounts to roughly 20 J/kg within the first 150 ms and converges to roughly 22 J/kg over the coarse of 350 ms. For the coarse (10 and 5 mm in Figure 5.5) voxel-mesh approximation, 22 J/kg is reached within the first 60 ms and 5 mm then converges at 23 J/kg. Therefore, besides the shorter crash response, the dissipated energies are very similar. For the finer meshes, failure at different timesteps led to greater frame bending followed by increased energy dissipation.

5.1.3 Passenger safety

Below, the two crash-response accelerations are presented to be compared, Figure 5.8 for the baseline and Figure 5.7 for the approximate voxel-mesh representations. Both have been filtered using 60 Hz Butterworth filtering. For the voxel-mesh approximations, the accelerometer is placed in the rigid body representing the floor. The baseline has its accelerometer in center of the section on the deformable floor.

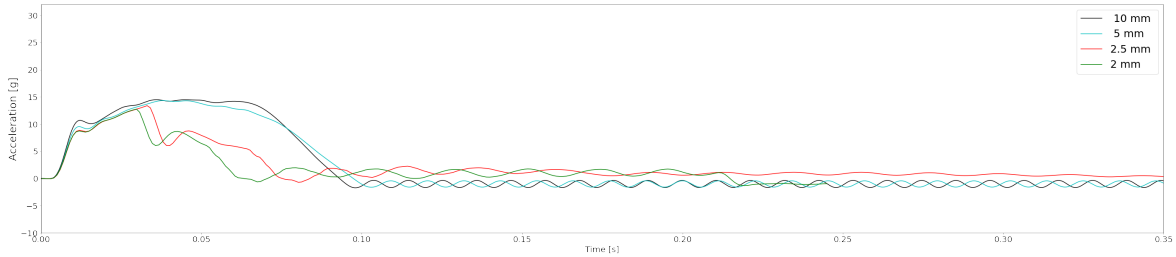

Figure 5.7: The resultant accelerations (100 Hz cut-off frequency, 4-pole Butterworth filtering) of the voxel-mesh approximations experienced by the rigid body

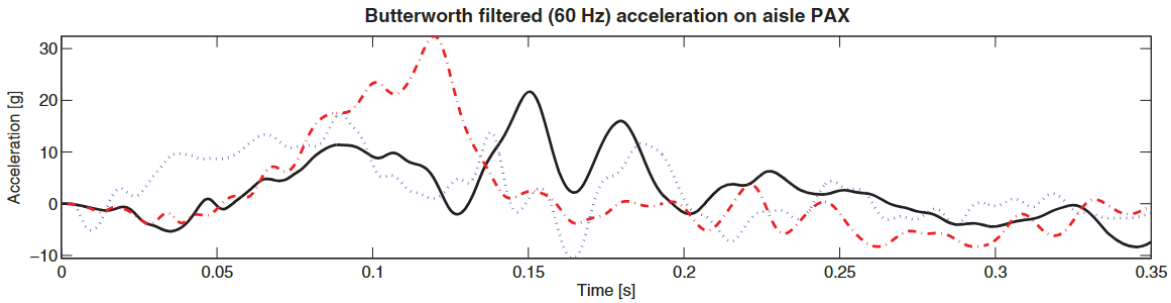

Figure 5.8: The resultant accelerations of the A350-like aircraft for different materials from [11] (black corresponds to metal)

Immediately it can be seen that, again, the crash-duration is shorter for the voxel-mesh

approximations and shows less variation during impact. Additionally, some oscillation is visible after 100 ms due to the elastic vibration mid-air of the structure after bounce. The meshes 10 and 5 mm peak at 15 g during spring-back at 60 ms, while progressive damage in 2.5 and 2 mm result in drop of acceleration and no spring-back. The baseline peaks at about 22 g during spring-back at 150 ms.

The voxel-mesh approximations have shown to not reach the same peak value, even though its floor is not able to dampen any motion (due to the rigid constraint). The difference of 7g is significant, but the least, the order of magnitudes are equal. On the other hand, the 10 mm and 5 mm mesh models have a sustained peak lasting almost 90-100 ms. This is in the same range of impact severity in the Eiband plot of Figure 5.9 [11]. Here, the voxel-meshes 10 and 5 mm ar represented by the red dot.

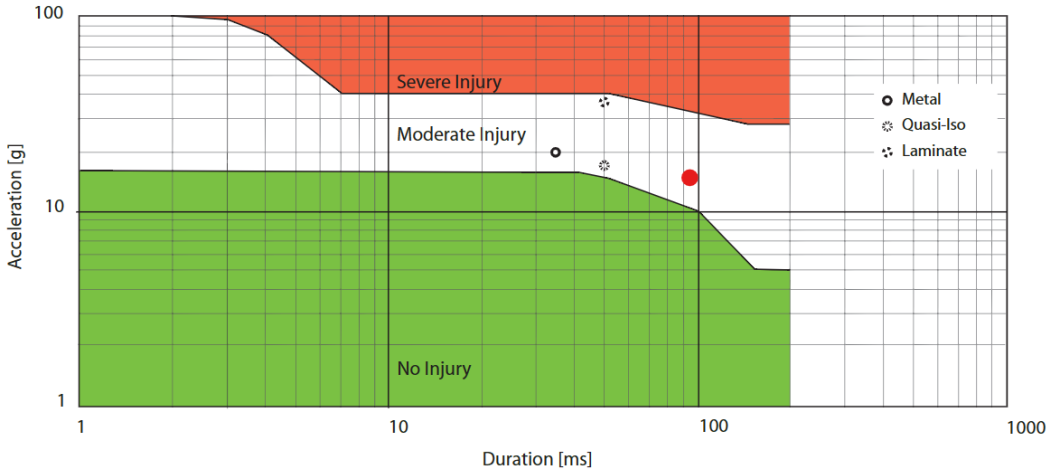

Figure 5.9: The injury severity of the crash response from [11]

5.1.4 Conclusion comparison and research question 1

It has been argued that multiple assumptions led to higher stress concentrations in all 4 meshes. The absence of energy dissipation in the floor-cabin or crippling in the skin brackets and the inability of the floor connections to rotate. These higher stress concentrations led to rupture for the fine meshes 2 and 2.5 mm which was not present in the metallic model of Gransden and Alderliesten [11]. The following solutions could make the voxel-mesh more representative of the detailed model:

1. The energy dissipated in brackets and skin should be removed from the input kinetic energy.

2. The cabin-floor structure should be idealized as well or replaced by a representative spring. By doing so, the hinge formation can be achieved in the voxel-mesh as well since translation and rotation is not obstructed.

Nevertheless, the 10 mm mesh and 5 mm mesh did not experience rupture (due to low detect-ability of stress peaks in coarser meshes) to which their crash-responses were in good

agreement in terms of plastic energy dissipation and injury severity. Their energy and acceleration profiles were far off still, as the duration until spring-back was almost three times shorter and the accelerations did not fluctuate as much.

RQ 1. How can detailed FEM aircraft crashworthiness assessment reliably be approximated by voxel-mesh models?

The suggestions named above are believed to make the voxel-mesh crash-responses representative for detailed models. In its current state, the approximation is reliable enough for the conceptual design stage.

For the duration of this thesis, hinge formation is forced by a removing element deletion and increases the impact kinetic energy. The stress concentrations do not result in failure and therefore the normal hinges can be formed.

5.2 Sub-floor structure crashworthiness TO using HCA: set-up

The aim of the proof-of-concept is to prove that standard crashworthiness TO is not suitable for aircraft such that a new method is to be found. The sub-floor structure of the previous section will be turned into a design space and optimized in this section.

5.2.1 Material, loads and boundary conditions II

The aforementioned progressive damage and element deletion has the potential to cause ruptures for intermediate densities in a topology optimization run. Lower thickness or density elements namely experience greater deformation. Three problems had been found for rupture in TO:

- Once an element is deleted, progressive damage can propagate through elements that have been 'removed' (at the minimum density/thickness) to functional elements. Additionally, it requires self-contact modelling.
- The response discontinuity between the subsequent iterations cause drastic topology changes and avoids convergence.
- A deleted element only holds a piece of the history of the crash duration.

Additionally, damage modelling had also not been included in the Controlled Energy Absorption research (the HCA baseline) by Bandi [16]. Therefore, considering all these arguments and the fact that there is no clear damage in the metal A350-like sub-floor structure FEM model [11], the strain limit has been removed from the material model.

By doing so, the entire model becomes stiffer so a compensation in kinetic energy is required. The aforementioned mass (1/6th of 2658.6 kg) and velocity (7 m/s) in Figure 3.14 have been increased such that the hinge characteristics can be observed, deviating from the baseline loads. The velocity of 9 m/s has been chosen following the research by Xue et al. [37]. The mass increased to 1250 kg. By doing so, a direct comparison between the A350-like crash response of Gransden and Alderliesten [11] and its voxel-mesh counterpart cannot be made

anymore, especially not with the nonphysical strains. The crash response of the voxel-mesh idealization can however be used to compare with the topology optimization output under the same conditions.

$$V = -9m/s, m = 1.250$$

Finally, the material model has been made more continuous by utilizing a Johnson-Cook plasticity model of the strain-rate insensitive Al2024-T3. At room temperature, the following parameters remain as presented in Table 5.1. The Johnson-Cook model in Equation 3.3 is a function of the plastic strain, A is the yield strength and B is the hardening modulus.

Table 5.1: Al-2024 T3 material properties

	Value	unit
ρ	2700	kg/m3
E	70	GPa
ν	0.33	
A	369	MPa
B	684	MPa
n	0.73	

5.2.2 Sub-floor structure mesh study

Four mesh sizes had been used so far and only one will be used in this thesis, which shall be found using a mesh-size study on the existing structure. These 4 sizes resulted in voxel-mesh approximations of equal total volume, such that they can be compared rightfully. Additionally, the coarsest size (10 mm) still guarantees that the existing sections of the A350-like aircraft are modelled with at least 4 elements in bending to avoid shear-locking.

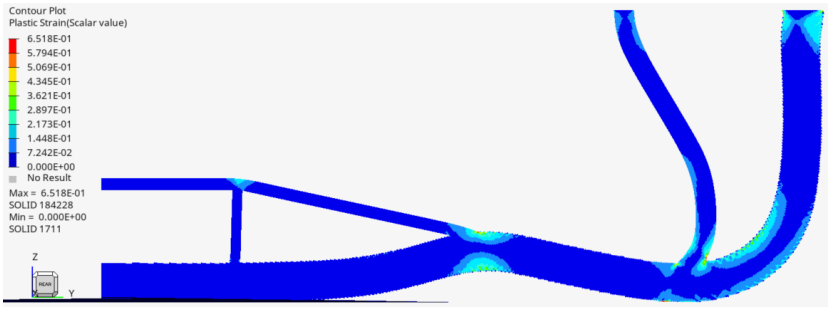

Figure 5.10: Plastic strain on the deformed voxel-mesh representation for mesh-size 5 mm

As can be seen in Figure 5.10, the increase in mass, velocity, change of material model and no of element deletion gives a deformation similar to that of the A320 in Figure 2.11. Especially the hinge at B is evident again. The hinge at C is still in the weaker strut due to the the inability of the strut and frame to translate and rotate from their floor connection point (the rigid body). The maximum plastic strain does exceed the earlier used 0.166 limit greatly as expected, however these are very localized points. The surrounding regions 1 or 2 elements

away show less than 0.2 plasticity. All the mesh sizes have the same deformation as shown in Figure 5.10.

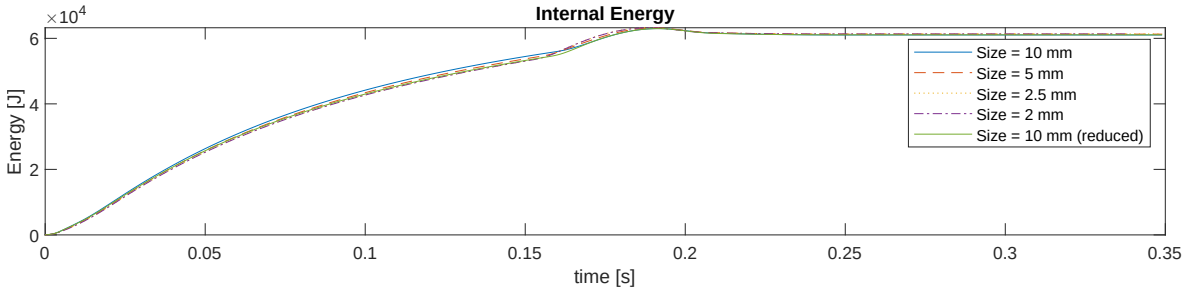

Figure 5.11: Internal energy profiles in the mesh-study

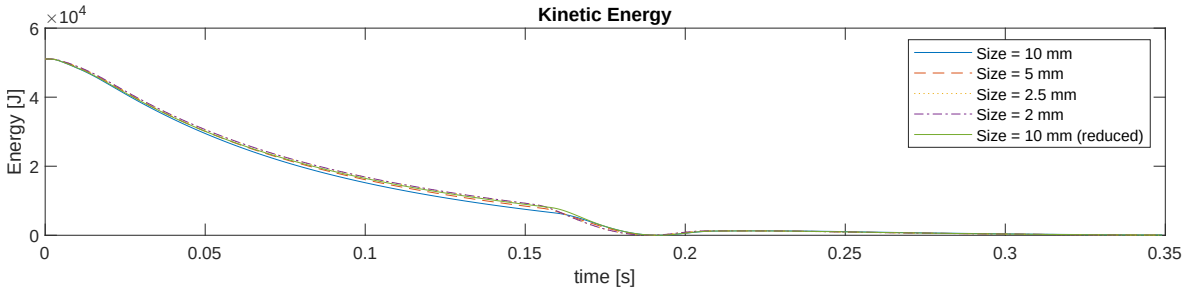

Figure 5.12: Kinetic energy profiles in the mesh-study

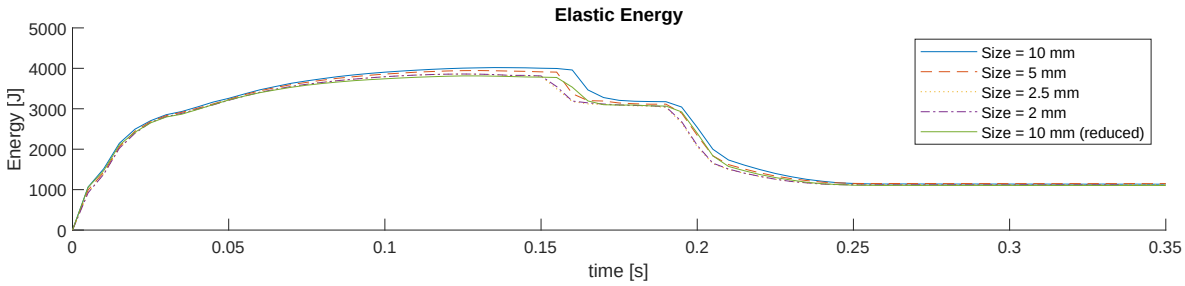

Figure 5.13: Elastic energy profiles in the mesh-study

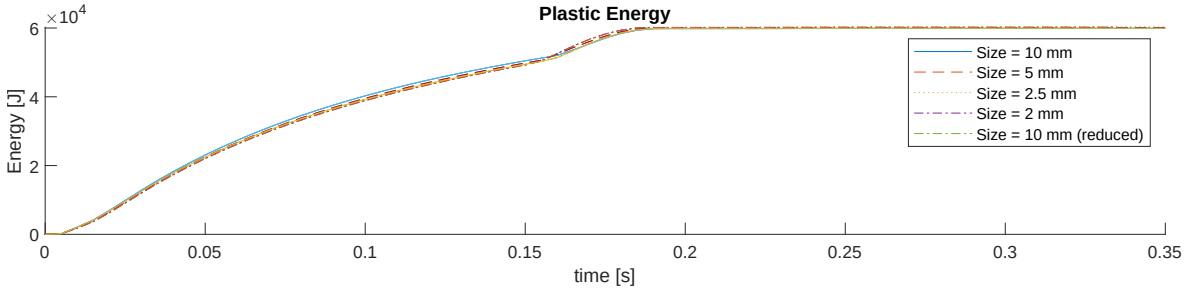

Figure 5.14: Plastic energy profiles in the mesh-study

The elastic, plastic, internal and kinetic energy are computed for each mesh size, these have been presented in Figure 5.11-Figure 5.14. The two kinks in each curves, between 150 ms and 200 ms, correlate to the frame hitting the ground at a second location (below the floor strut) and bouncing back up. It is clear that each mesh size is able to capture the exact same crash response. The only significant difference can be found close to 150 ms for the elastic energy, where mesh size 10 shows some delay. When computing the error between the elastic energy peaks between mesh 10 and mesh 2 (correcting the delay), the error is only 3.9%. A mesh of 10x10x5 mm is thus fine enough, moreover going from 10 mm to 5 mm costs roughly 4 times as much computational power.

On that note, fully-integrated elements are costly, thus it is preferred to move towards reduced integration. The default reduced integration element of radioss (Isolid =24) is used, with physical hourglass control since the structure is loaded in bending. Again full geometric non-linearities are used. The results had been added in each graph, showcasing good agreement with the finer 2 mm mesh.

It is important to note different mesh-sizes result in different levels of detail in a HCA topology solution. However, this study is removed from the scope of this thesis. The minimal resolution of 10 mm has been chosen to make sure that the level of detail of the current A350-like aircraft can be attained, since the narrowest section is 40 mm high with a minimum of 3-4 elements along the bend. A larger mesh size was thus not added in the study.

5.2.3 Sub-floor structure HCA crashworthiness TO: Design domain

The sub-floor structure is now fully filled as a starting point. The frame shall always be present (as stated in the assumptions) and is taken out of the design domain.

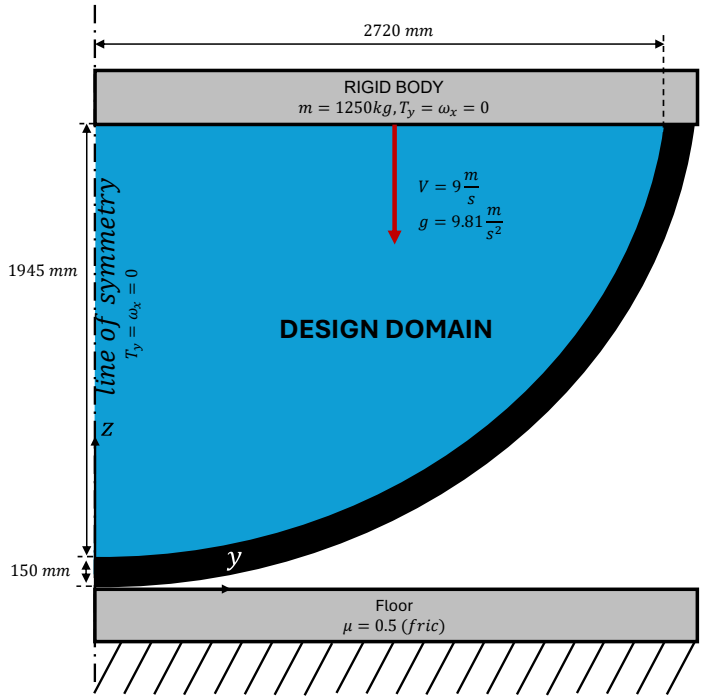

Figure 5.15: The design domain to be optimized using the HCA (the velocity and gravity are imposed on the whole model)

The final mass goal is to be the same as the A350-like voxel-mesh approximation, such that the comparison is fair. The number of elements that the floor strut, cargo-floor spar and cargo-floor strut have combined has been divided by the number of elements in the design domain to find the target mass fraction:

$$M_{target} = 0.0461$$

5.3 Sub-floor structure HCA and BOHCA solutions

In order to prove the in-applicability of the original HCA method, it has been applied to a A350-like sub-floor design-space, aiming to present the need for plastic hinge formation in topology optimization. Secondly, the new HCA method has been applied and compared to the A350-like voxel-mesh approximation.

5.3.1 Standard HCA

The Figure 5.15 for 10 mm mesh resulted in 46182 elements. Using the basic principles presented in section 3.2 on Delftblue HPC (24 CPU 4Gb/CPU for 15 min per iterations) gave

the following results.

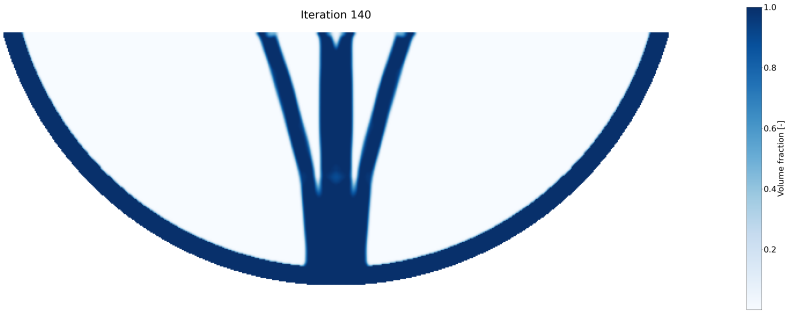

Figure 5.16: Sub-floor topology solution for iteration 140

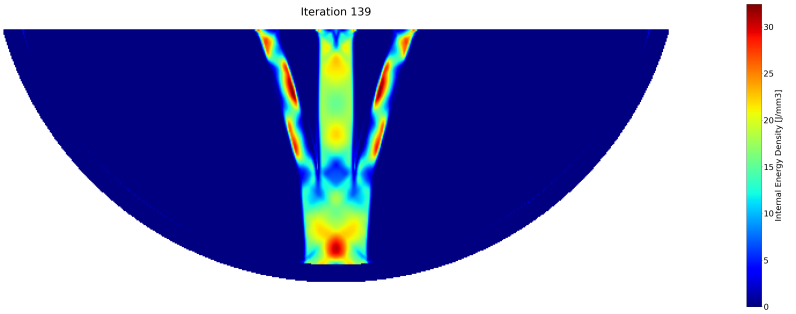

Figure 5.17: Sub-floor IED distribution for iteration 139: basic HCA

Between iteration 140 and iteration 50 there is little difference, the convergence tolerance was too small or the control parameter gain should have been increased.

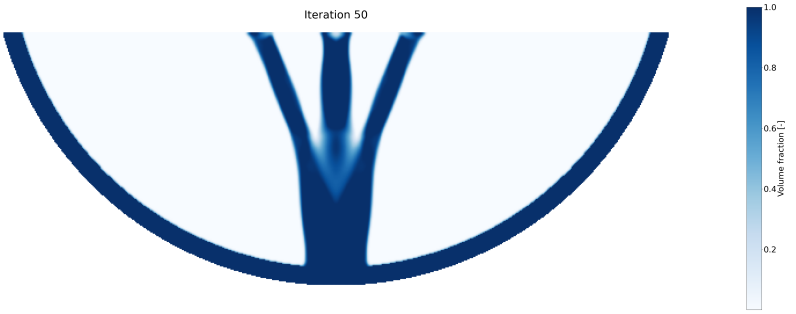

Figure 5.18: Sub-floor topology solution for iteration 50: Basic HCA

The IED plot as shown in Figure 5.17 demonstrates that the HCA principle indeed acquires

a structure of which every element contributes in carrying the internal energy. However, you can already see that, in terms of passenger safety, this design is far from optimal. The accelerations are not shown as the input mass is not representative anymore. Instead, the force displacement curve has be shown.

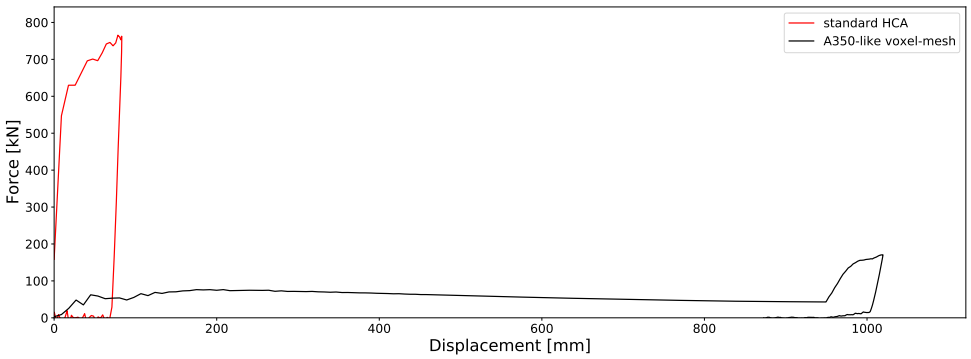

Figure 5.19: Force displacement curves of the standard HCA and the baseline voxel-mesh representation

As expected, the standard HCA proves insufficient as the force propagating to the floor far exceeds the baseline with minimal displacement. Negligible energy is dissipated, therefore, the energy profiles are not shown for this design.

5.3.2 Bending-Optimized HCA

The boundary condition applied resembling plane-strain caused inconsistencies with the plane-stress shell model. It has been derived that this is due to the low-density elements straining excessively. With the inability to expand out-of-plane, the mass shift in other directions, creating bending energies.

Therefore, in the sub-floor model, this out-of-plane deformation constraint has been relaxed, resulting in very small out-of-plane stress (resembling the shell model again).

Four solutions are provided in this order, all using the L-IED2 function and full averaging of the bending energy:

1. Preference: [A=B=1], full averaging of the densities

2. Preference: [A=60, B=1], full averaging of the densities

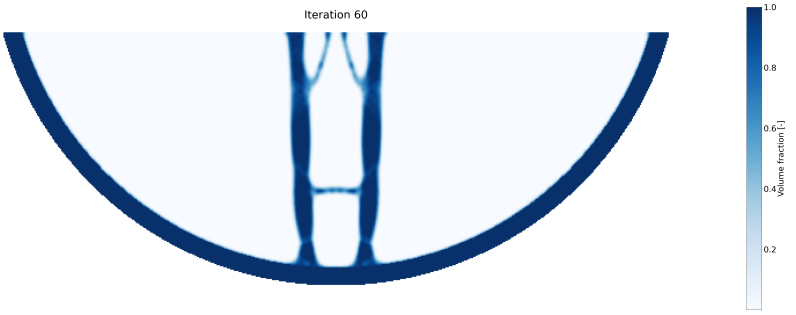

Figure 5.20: Sub-floor topology solution for L-IED2, Preference: [A=B=1], full averaging of the densities

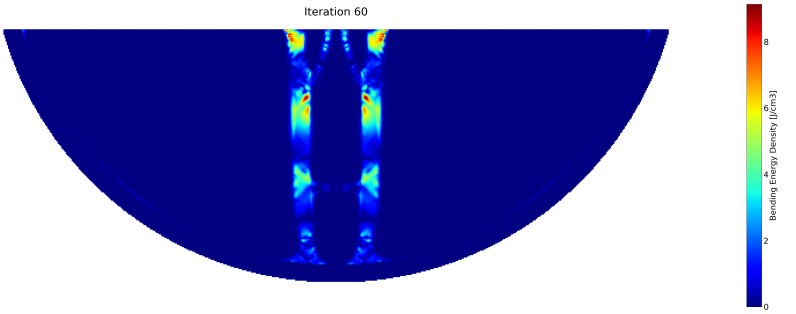

Figure 5.21: Bending Energy: sub-floor topology solution for L-IED2, Preference: [A=60, B=1], full averaging of the densities

The relatively straight columns of Figure 5.22 appear to be hinge about the stiffened intersects, with increased bending energies as shown in Figure 5.23.

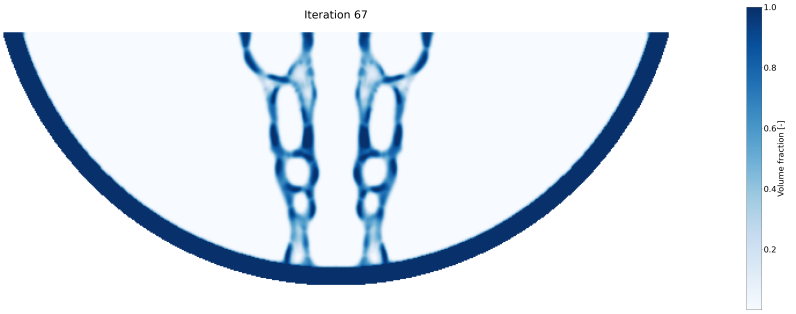

Figure 5.22: Sub-floor topology solution for L-IED2, Preference: [A=B=1], full averaging of the densities

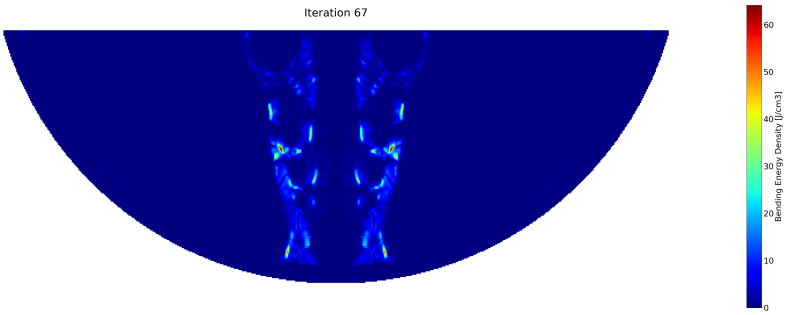

Figure 5.23: Bending Energy: sub-floor topology solution for L-IED2, Preference: [A=60, B=1], full averaging of the densities

As expected, adding a preference to the Q-IED function is consistent with the compression beam case presented in Figure 4.30, creating bubble like sections that resemble large-scale spinodal structures.

Chapter 6

Conclusion and Recommendations

It has been envisioned that unconventional aircraft structural design can make good use of topology optimization in the conceptual design phase, finding the most efficient distribution of mass for all load-cases without going back and forth. One of such cases is crashworthiness design and assessment, which can be a complication for the Flying-V with its reduced sub-floor hold volume. Therefore, a methodology has been developed that optimizes the sub-floor structure domain in terms of bending-energy. The method proved effective in creating sections that are loaded in bending for a representative small scale model.

Plastic hinges are a direct consequence of bending, leading towards the objective of uniform bending energy distribution in the Hybrid Cellular Automata framework. Reconstructing the bending energy functions on inter-cell-level using the Hybrid Cellular Automata principle showed good agreement with intra-level computations, while increasing the stability. The derived bending energy function assumed linear distribution of strains and stresses in the plane of bending. Although thickness/density gradients were found non-adhering to this assumption, the formulation proved successful in returning sections loaded in bending. The objective function with the standard formulation however was found incapable of exploiting these sections to form hinges, as hinges are being fortified resulting in stiff bending sections.

The assumption of both a linear stress and strain distribution in elastic and plastic deformation resulted in a quadratic (Q-IED) and a linear (L-IED) term in the bending energy density formulation. This L-IED function had been interpreted or manipulated in four ways. A comparison study found that L-IED-2, which favours coherence between the strain and stress gradient in a single direction, has the highest potential in leading towards hinge-formation, due to the greater curvatures in the sections. A study on the relative contribution of the L-IED-2 and its Q-IED counterpart to the total energy has shown that the structure can become more compliant by favoring Q-IED, resulting in effective peak force reduction. An optimal number should be found to avoid convergence issues and de-facto hinge occurence. Thus, for the first part of the hypothesis below, it can be concluded that plastic hinge formation and compliant mechanisms can be achieved in HCA by manipulating the bending-energy formulation.

Does bending optimization in HCA allow plastic hinge formation in topology optimization (TO) to improve the crashworthiness of aircraft?

Finally, to test the applicability of the framework for aircraft crashworthiness, a sub-floor structure had been optimized. The validity of a voxel-mesh model for aircraft crash-analysis needed to be proven. The A350-like aircraft voxel-mesh approximation showed good agreement with a detailed analysis, considering the simplifications made and the envisioned design phase usage. This conclusion had been drawn from deformation, acceleration and energy analysis. The rigid-floor coupling should be removed and replaced by the actual cabin-floor (stiffness). The framework was then applied on the entire sub-floor volume to conclude on the second part of the hypothesis.

Recommendations bending energy

1. Include the non-linear terms in the Lagrange strain tensor in deriving the bending energy
2. Derive the corresponding non-linear stress distribution function
3. Find a new objective function that does not bring the whole domain to an equal state of bending, but rather exploit some hinges that are formed.

Recommendations aircraft crashworthiness and TO

1. Set-up an element reintroduction scheme to be able to remove them from the non-linear analysis. The minimum value of 0.001 absorbs a negligble amount of energy, although the response is altered once they have been completely removed
2. Reduce the input kinetic energy with a factor that corresponds to energy dissipating in rivet failure and plasticity in the skin-panel.
3. Include the static case of supporting the floor in the topology run. Use the standard HCA with strain energy density (elastic) and combine with the crash-scenario through weighting.
4. Do not replace the cabin-floor structure with a rigid body for computational cost saving, as rotation along the frame-hinge is comprised and the accelerations are uniform along the seating span. Idealize both the cabin-frame and floor or limit the computational cost through replacement with a very-stiff material (replicating the cabin-floor stiffness).
5. Remove the cargo-hold from the design domain to force a load around the hold.

References

[1] P.D. Bravo-Mosquera, F.M. Catalano, and D.W. Zingg. Unconventional aircraft for civil aviation: A review of concepts and design methodologies. *Progress in Aerospace Sciences*, 131:4, 2022.

[2] R. Vos, F.J.J.M.M. Geuskens, and M.F.M. Hoogreef. A new structural design concept for blended wing body cabins. *53rd AIAA/ASME/ASCE/AHS/ASC Structures, Structural Dynamics and Materials Conference*, 2012.

[3] L.A. van der Schaft. Development, model generation and analysis of a flying v structure concept, 2017.

[4] M. Claeys. Flying-v and reference airraft structural analysis and mass comparison, 2018.

[5] T.P. Dotman. A structural sizing methodology for the wing-fuselage of the flying-v, 2021.

[6] R.C.J. Voeten. Flying-v: A design methodology for unconventional engine mounting structures, 2022.

[7] L. Krog, A. Tucker, and G. Rollema. Application of topology, sizing and shape optimization methods to optimal design of aircraft components. *Proceedings of 3rd Altair UK HyperWorks users conference*, 2002.

[8] G. Singh and V. Toropov. Topology optimization of a blended wing body aircraft structure. *17th AIAA/ISSMO Multidisciplinary Analysis and Optimization Conference*, 2016.

[9] H. Mou, J Xie, and Z. Feng. Research status and future development of crashworthiness of civil aircraft fuselage structures: An overview. *Progress in Aerospace Sciences*, 119, 2020.

[10] M. Waimer. Development of a kinematics model for the assessment of global crash scenarios of a composite transport aircraft fuselage. *University of Stuttgart*, pages 1–274, 2013.

[11] Derek Gransden and René Alderliesten. Development of a finite element model for comparing metal and composite fuselage section drop testing. *International Journal of Crashworthiness*, 22:1–14, 01 2017.

[12] M. Desiderio. Flying-v crashworthiness: a preliminary assessment, 2023.

[13] G. Das, J. Gloyd, Y. Fu, G. Kennedy, and K. James. Topology optimization of crash-tolerant aircraft structures. 06 2023.

[14] J. Triller, R. Immel, and L. Harzheim. Topology optimization using diference-based equivalent static loads. *Structural and Multidisciplinary Optimization*, 65, 2022.

[15] A. Tovar, N.M. Patel, G.L. Niebur, M. Sen, and J.E. Renaud. Topology optimization using a hybrid cellular automaton method with local control rules. *Journal of Mechanical Design*, 128, 2006.

[16] P. Bandi, J.P. Schmiedeler, and A. Tovar. Design of crashworthy structures with controlled energy absorption in the hybrid cellular automaton framework. *Journal of Mechanical Design*, 135, 2013.

[17] W.J. Oosterom. Flying-v family design, 2021.

[18] W.J. Oosterom and R. Vos. Conceptual design of a flying-v aircraft family. *AIAA AVIATION 2022 Forum: June 27-July 1, 2022, Chicago, IL Virtual Article AIAA 2022-3200 (AIAA AVIATION 2022 Forum). American Institute of Aeronautics and Astronautics Inc. (AIAA)*, 2022.

[19] J. Benad. The flying v a new aircraft configuration for commercial passenger transport. *Deutscher Luft- und Raumfahrtkongress*, 2015.

[20] M. Nanninga. High-fidelity structural sizing method for weight estimation of a flying-v, 2023.

[21] J.-H. Zhu, W.-H. Zhang, and L. Xia. Topology optimization in aircraft and aerospace structures design. *Archives of Computational Methods in Engineering*, 23:595–622, 2016.

[22] R. Sturm and M. Hepperle. Crashworthiness and ditching behaviour of blended-wing-body (bwb) aircraft design. *International Journal of Crashworthiness*, 22:592–601, 2015.

[23] European Union Aviation Safety Agency. ertification specifications and acceptable means of compliance for large aeroplanes (cs-25) - amendment 27. 2021.

[24] D.B. Schwinn. Integration of crashworthiness aspects into preliminary aircraft design. *Applied Mechanics and Materials*, 598:146–150, 2014.

[25] A.I.H. Nasrullah, S.P. Santosa, and T. Dirgantara. Design and optimization of crashworthy components based on lattice structure configuration. *Structures*, 26:969–981, 2020.

[26] J. Fang, G. Sun, N. Qiu, N.H. Kim, and Q. Li. On design optimization for structural crashworthiness and its state of the art. *Structural and Multidisciplinary Optimization*, 55:1091–1119, 2017.

[27] N. Aullig, E. Nutwell, S. Menzel, and D. Detwiler. Preference-based topology optimization for vehicle concept design with concurrent static and crash load cases. *Structural and Multidisciplinary Optimization*, 57:251–266, 2018.

[28] N.M. Patel, B-.S. Kang, and J.E. Renaud. Topology synthesis of structures under impact loading using a hybrid cellular automaton algorithm. *11th AIAA/ISSMO Multidisciplinary Analysis and Optimization Conference*, 2006.

[29] J.D. Deaton and R.V. Grandhi. A survey of structural and multidisciplinary continuum topology optimization: post 2000. *Structural and Multidisciplinary Optimization*, 49:1–38, 2014.

[30] D. Yago, J. Cante, O. Lloberas-Valls, and J. Oliver. Topology optimization methods for 3d structural problems: A comparative study. *Archives of Computational Methods in Engineering*, 29:1525–1567, 2022.

[31] H-.A. Lee and G-.J. Park. Nonlinear dynamic response topology optimization using the equivalent static loads method. *Computational Methods in Applied Mechanics and Engineering*, 283:956–970, 2015.

[32] R. Behrou, R. Lotfi, J.V. Carstensen, F. Ferrari, and J.K. Guest. Revisiting element removal for density-based structural topology optimization with reintroduction by heaviside projection. *Computer Methods in Applied Mechanics and Engineering*, 380, 2021.

[33] A.A. Patel and A.N. Palazotto. Design methodology for topology optimization of dynamically loaded structure. *Journal of Dynamic Behaviour of Materials*, 5:59–64, 2019.

[34] Y.C. Bai, H.S. Zhou, F. Lei, and H.S. Lei. An improved numerically-stable equivalent static loads (esls) algorithm based on energy-scaling ratio for stiffness topology optimization under crash loads. *Structural and Multidisciplinary Optimization*, 59:117–130, 2019.

[35] N.M. Patel, B-.S. Kang, J.E. Renaud, and A. Tovar. Crashworthiness design using topology optimization. *Journal of Mechanical Design*, 131, 2009.

[36] M. Afrousheh, J. Marzbanrad, and D. Göhlich. Topology optimization of energy absorbers under crashworthiness using modified hybrid cellular automata (mhca) algorithm. *Structural and Multidisciplinary Optimization*, 60:1021–1034, 2019.

[37] P. Xue, L. Ding, F. Qiao, and X. Yu. Crashworthiness study of a civil aircraft fuselage section. *Latin American Journal of Solids and Structures*, 11.9:1615–1627, 2014.

Appendix A

Stress gradient with material interpolation: proof

The necessity of the stress gradient correction for material interpolation TO presented in subsection 3.4.2 will be shown in this Appendix.

A.1 Stress and strain linear-gradient approximation comparison

For the solution of L-IED-2 presented in Figure 4.19, the gradients have been computed for the shell model without material interpolation and the brick model with material interpolation.

For comparison, the bounds of the brick gradients (Figure A.2) are from the shell model bounds (Figure A.1).

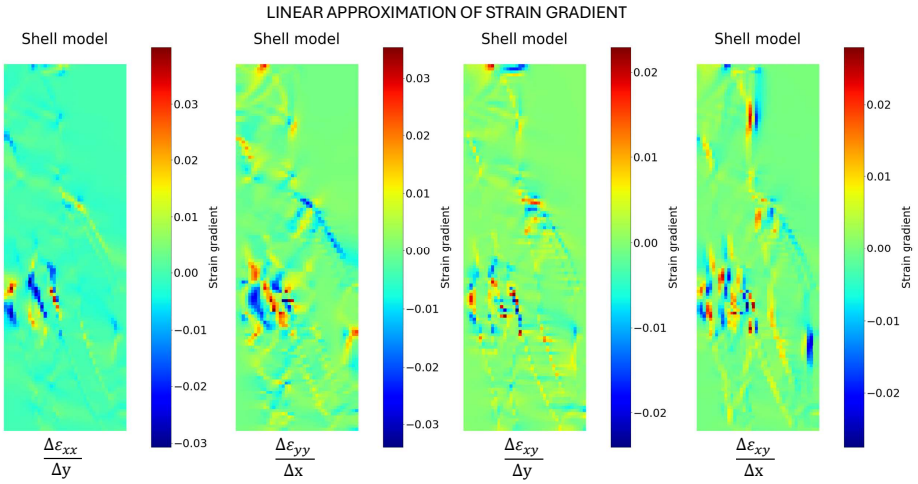

Figure A.1: Shell model (no material interpolation) linear strain gradient approximation at peak internal energy

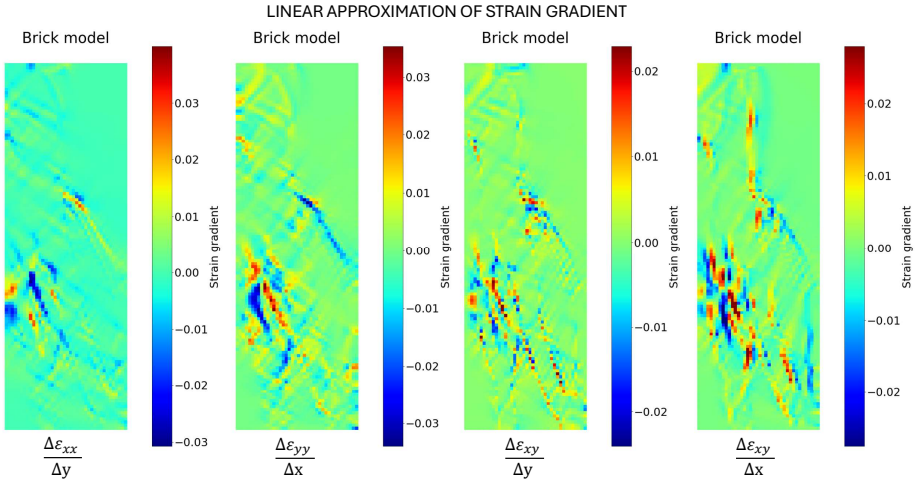

Figure A.2: Brick model (with material interpolation) linear strain gradient approximation at peak internal energy

As expected, the distribution of the strain gradient approximations are equal. The magnitudes of the brick model, with material interpolation are slightly larger due to the degraded stiffness

of intermediate densities.

Material interpolation results lower stress magnitudes, scaling the bending energy density for brick elements. In the shell model, the total energy is scaled through the thickness (Equation 3.37. Therefore, since the strains are considered identical, the shell thickness scaling is included in its stress gradient (see Figure A.3).

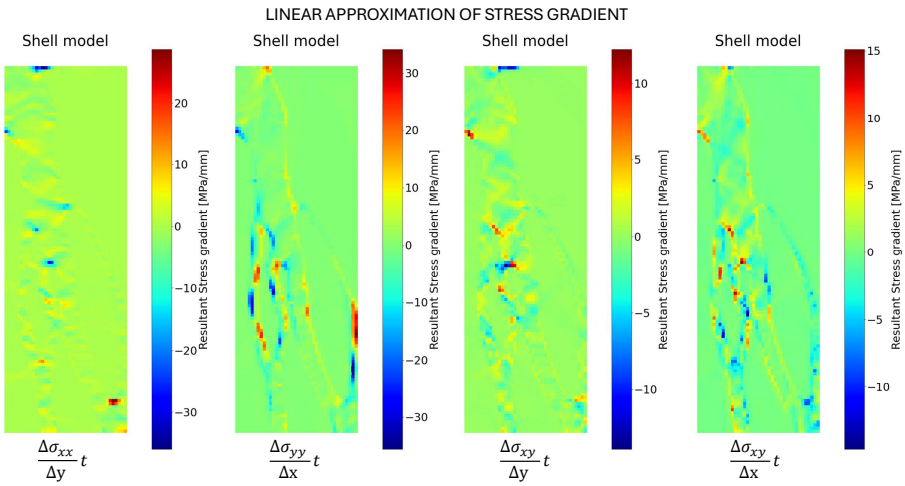

Figure A.3: Shell model (no material interpolation) linear stress gradient approximation at peak internal energy

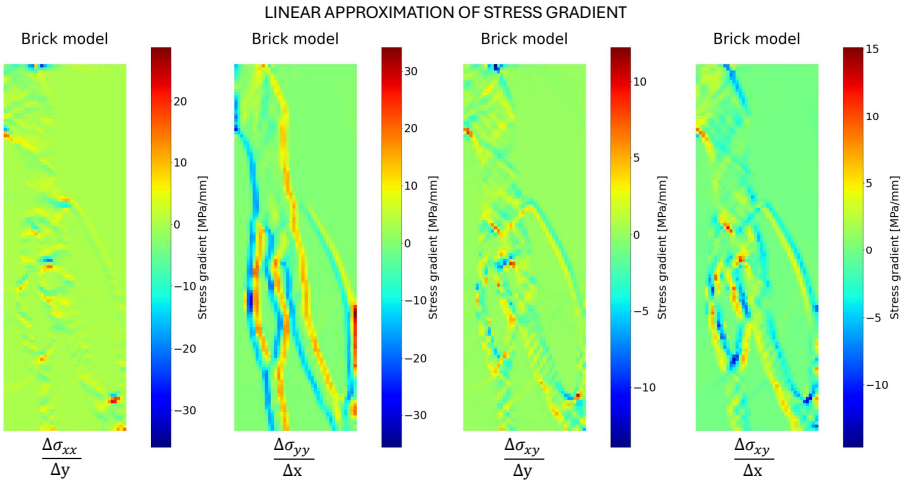

Figure A.4: Brick model (with material interpolation) linear stress gradient approximation at peak internal energy

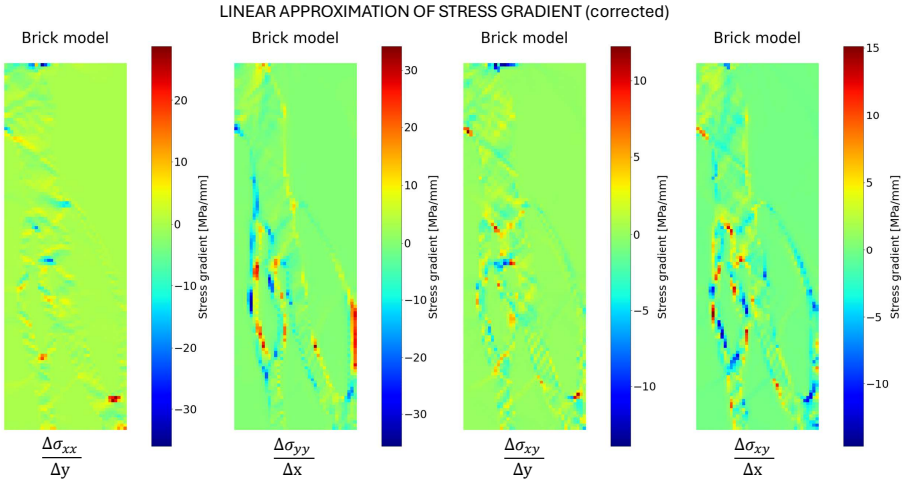

Figure A.5: Brick model (with material interpolation) corrected linear stress gradient approximation at peak internal energy

The uncorrected stress gradient approximations of the brick model (Figure A.4) clearly follow the outline of the design, hinting at correlation to the density gradients. These inconsistent

gradients induce increased non-physical bending energy, avoiding sharpening (black-white) of the design. Correction as presented in subsection 3.4.2 has been shown in Figure A.5. The inconsistent gradients along the boundaries are filtered and the peak gradients are equal to those in Figure A.3.

A.2 Result comparison

Below, in Figure A.6 in can indeed be seen that even after 117 iterations, the boundaries are not refined. With correction (Figure A.7), convergence can be reached.

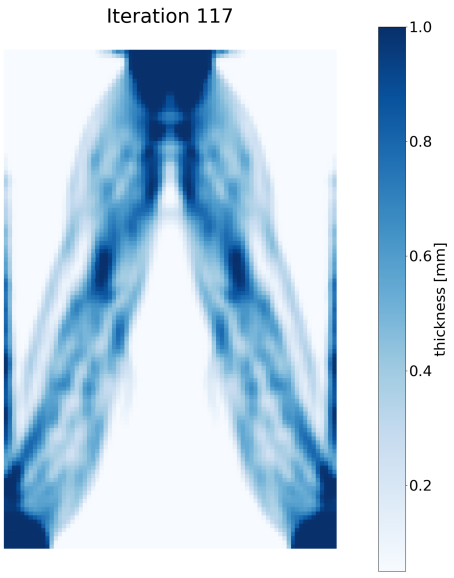

Figure A.6: Topology solution (not converged) for the brick model (with material interpolation) without stress gradient correction

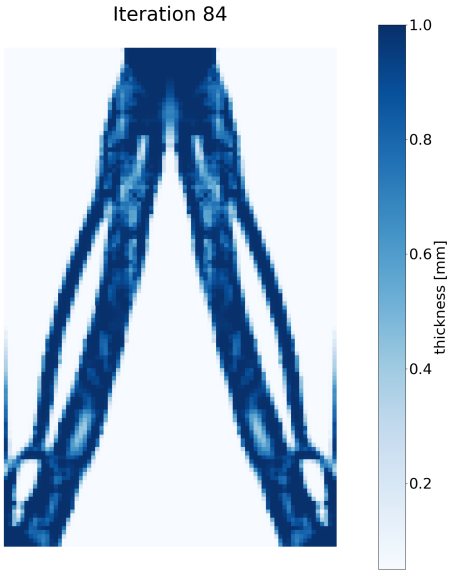

Figure A.7: Topology solution for the brick model (with material interpolation) with stress gradient correction

Appendix B

Shells thickness optimization without material interpolation: analysis

Shell thickness optimization as performed in this thesis has assumed that material interpolation is not necessary for the HCA algorithm, following the inability of shell material interpolation in Radioss. The algorithm is not gradient-based, rather local rules on the field variable (bending energy in this case) are used in optimization. However, minimum thickness elements could influence the response. This chapter compares brick elements with material interpolation with that of shell elements without material interpolation.

B.1 Comparison with brick model including material interpolation

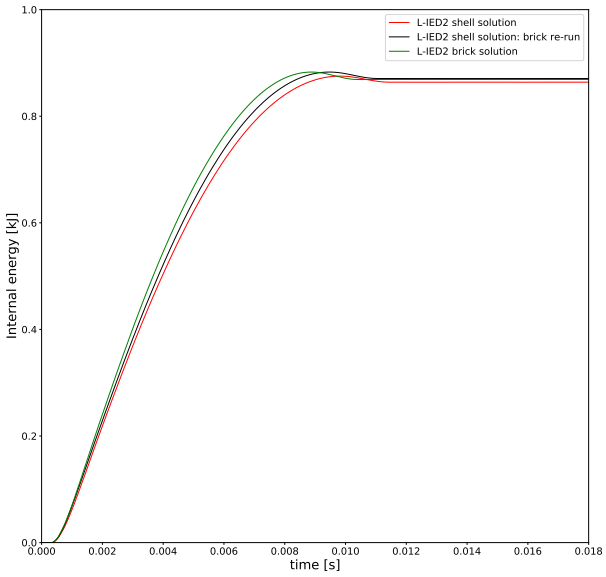

Figure B.1: Internal energy profiles of the L-IED2 (iteration 100) shell solution and its material-interpolated brick re-run

Comparing the shell analysis with the brick re-run of the same topology solution (**??**) in Figure B.1, it is visible that the thin elements with unaltered stiffness and yield strength do not absorb significantly deviating energy. In fact, at t= 0.018, 11.0% of the absorbed energy dissipated in the elements thinner than 10% of the maximum thickness. In the brick re-run, that is 11.6% composed by the same elements.

The brick-rerun has a little more elastic energy stored at peak internal energy, due to the reduced stiffness'. Furthermore, when looking at Figure B.2, material interpolation resulted in less indentation of the impactor, while increasing the peak load all the while. A potentional cause for this mismatch might be that the material interpolation (in Radioss) also includes scaling of the internal forces (besides scaling of the density, stiffness and yield strength), possibly slightly altering the load path. Other reasons could be the plane-stress simplification of the shells or the different forms of hourglass stabilization.

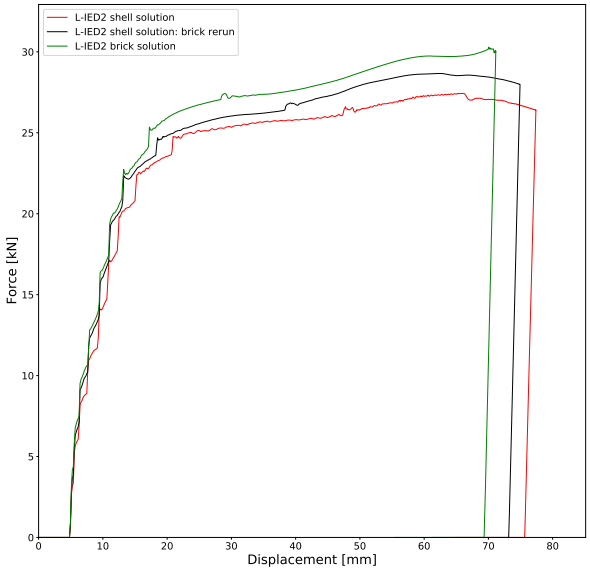

Figure B.2: Force-displacement curves of the L-IED2 (iteration 100) shell solution and its material-interpolated brick re-run

The solution of a full optimization run on the brick model with material interpolation had been presented in Figure A.7. Its results have been added to the plots, leading towards the conclusion that (for 2D cases) this HCA framework might work better using shells without material interpolation. The naturally continuous stress field, as opposed to correcting the stress gradients, might play a role in this.

B.2 conclusion

Altogether, material interpolation does indeed not necessarily need to be included in the HCA framework for shells since the thickness is incorporated in the total energy computation. However, the responses can differ, resulting in different topology solutions.

Appendix C

Intra-level strain gradient verification: Small-strain verification

Some inconsistencies were found with the intra-level deformation (see subsection 4.1.1) which require verification of the inter-level bending energies. A simplified model has been used to find the element strains along the edges, which neglects the geometrical non-linearities. This section verifies the simplified model by comparing the strains with the true (fully non-linear geometrical) strains from Radioss.

C.1 Verification case

An intermediate result of L-IED2 has been taken, experiencing large displacements and rotations due to the intermediate thicknesses. See Figure 4.10.

C.2 Strain comparison

The true strains for the analysis using full geometrical non-linearities is shown in Figure C.1. Reconstruction of the true strains using its displacement field and neglecting the non-linear terms and rotations is given in Figure C.2. Note that the bounds of the true strains are projected on the reconstruction.

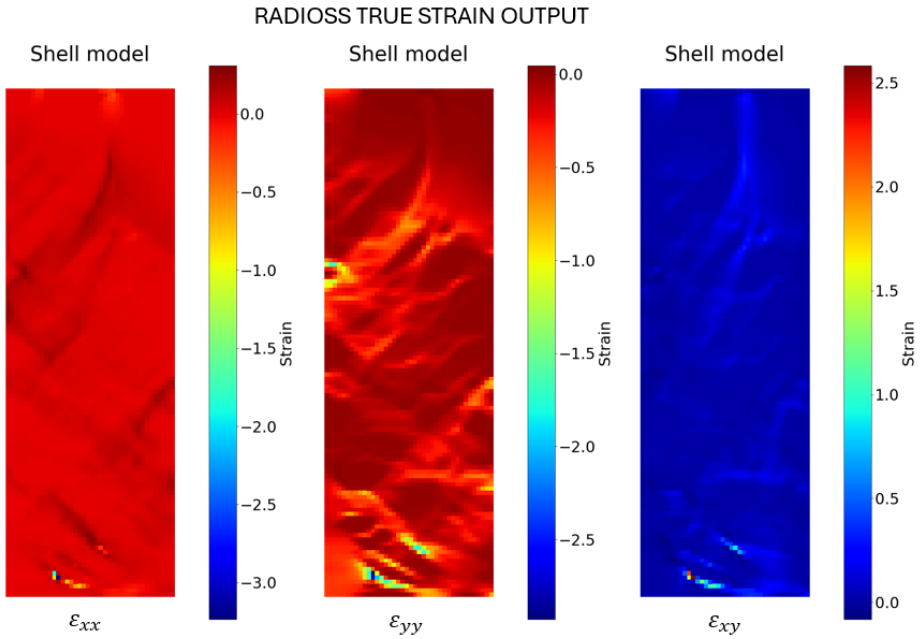

Figure C.1: Strains at peak energy using full geometrical non-linearity

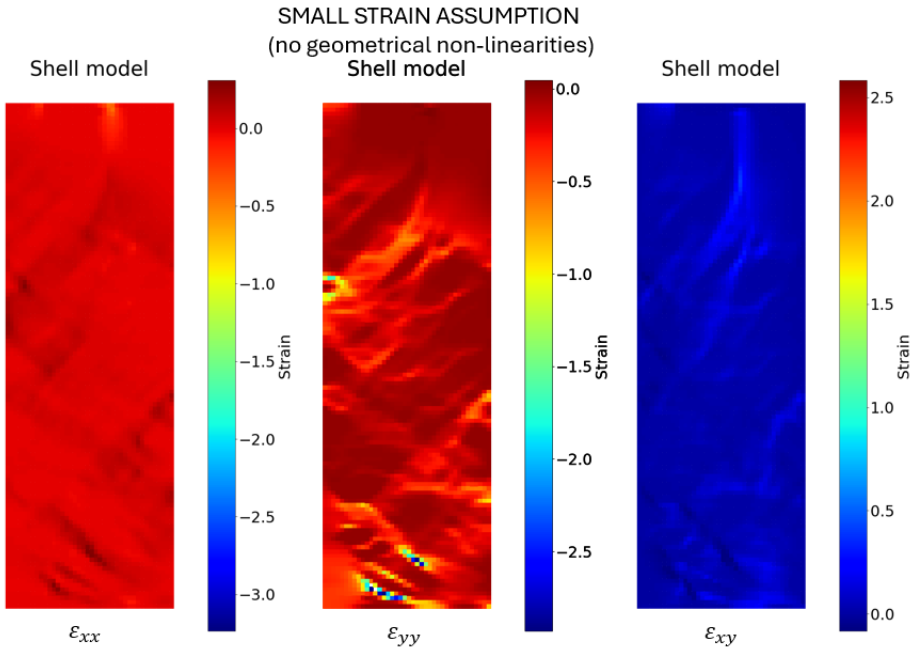

Figure C.2: Strain reconstructing from the true strain displacement field at peak energy using small strains on global reference

The figures show good agreement, while only the regions with excessive distortion (Figure C.3) are significantly different.

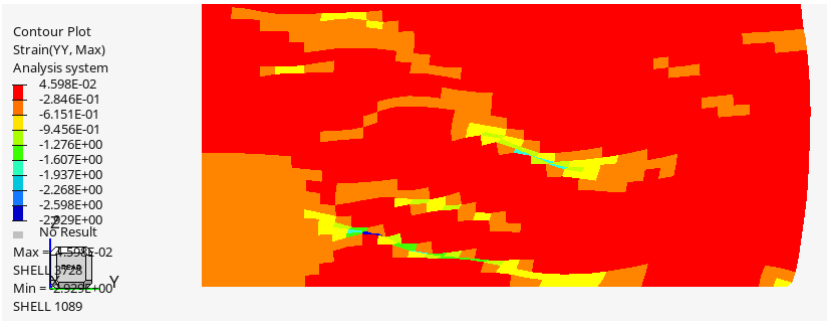

Figure C.3: Distorted elements visible in the ε_{yy} plot

Appendix D

Alternative stress-gradient approximation

To avoid using the stress states of plastically deformed thinner adjacent neighbors, the internal stress gradient of the center element can be reconstructed from the strain gradients.

The stress state of a plane stress shell element in Radioss is computed using explicit time integration using the strain rate. This elastic stress is presented in Equation D.1.

$$\boldsymbol{\sigma}^{el}(t+\Delta t) = \boldsymbol{\sigma}(t) + \mathbf{L}\dot{\boldsymbol{\varepsilon}}\Delta t \tag{D.1}$$

Here, $\boldsymbol{L}$ is the plane stress stiffness matrix:

$$\mathrm{L} = \begin{bmatrix} \frac{E}{1-\nu^2} & \frac{\nu E}{1-\nu^2} & 0 \\ \frac{\nu E}{1-\nu^2} & \frac{E}{1-\nu^2} & 0 \\ 0 & 0 & \frac{E}{1+\nu} \end{bmatrix} \tag{D.2}$$

Suppose for a small enough value of delta t, $\mathbf{L}\dot{\varepsilon}\Delta t = \boldsymbol{L}\Delta\boldsymbol{\varepsilon}$.

The element von-mises stress for a plane stress shell element is given Equation D.3. The yield stress is calculated using the Johnson-cook plasticity model presented in Equation D.4, where a is the material yield stress, b is the hardening modulus, ε_p the true plastic strain and n the hardening exponent.

$$\sigma^{VM} = \sigma_{xx}^2 + \sigma_{yy}^2 - \sigma_{xx}\sigma_{yy} + 3\sigma_{xy}^2 \tag{D.3}$$

$$\sigma^{yield}(t) = a + b\varepsilon_p^n(t) \tag{D.4}$$

Once an element starts yielding ($\sigma^{VM} > \sigma^{yield}$), its (elastic) von-mises stress needs to be brought back to the yielding surface called the plastic admissible stress (σ^{pa}. This turns Equation D.1 in:

$$\boldsymbol{\sigma}_{i+1}^{pa} = \frac{\sigma_{i+1}^{yield}}{\sigma_{i+1}^{VM}}(\boldsymbol{\sigma}_i + \boldsymbol{L}\Delta\boldsymbol{\varepsilon}) \tag{D.5}$$

Now, when we want to compute the top or bottom stress, we simply have:

$$\boldsymbol{\sigma}_{i+1}^{TOP} = \frac{\sigma_{i+1}^{yield}}{\sigma_{i+1}^{VM}}(\boldsymbol{\sigma}_{i}^{TOP} + \boldsymbol{L}\Delta\boldsymbol{\varepsilon}^{TOP}) \tag{D.6}$$

Then the gradient of Equation 3.39 becomes:

$$\frac{\boldsymbol{\sigma}_{i+1}^{TOP} - \boldsymbol{\sigma}_{i+1}^{BOTTOM}}{2h} = \frac{\sigma_{i+1}^{yield}}{\sigma_{i+1}^{VM}}\left(\frac{\boldsymbol{\sigma}_{i}^{TOP} - \boldsymbol{\sigma}_{i}^{BOTTOM}}{2h} + \boldsymbol{L}\frac{\Delta\boldsymbol{\varepsilon}^{TOP} - \Delta\boldsymbol{\varepsilon}^{BOTTOM}}{2h}\right)$$

or:

$$\frac{\boldsymbol{\sigma}_{i+1}^{TOP} - \boldsymbol{\sigma}_{i+1}^{BOTTOM}}{2h} = \frac{\sigma_{i+1}^{yield}}{\sigma_{i+1}^{VM}}\left(\frac{\boldsymbol{\sigma}_{i}^{TOP} - \boldsymbol{\sigma}_{i}^{BOTTOM}}{2h} + \boldsymbol{L}\frac{(\boldsymbol{\varepsilon}_{i+1}^{TOP} - \boldsymbol{\varepsilon}_{i}^{TOP}) - (\boldsymbol{\varepsilon}_{i+1}^{BOTTOM} - \boldsymbol{\varepsilon}_{i}^{BOTTOM})}{2h}\right)$$

Grouping the strain terms to gradients:

$$\frac{\boldsymbol{\sigma}_{i+1}^{TOP} - \boldsymbol{\sigma}_{i+1}^{BOTTOM}}{2h} = \frac{\sigma_{i+1}^{yield}}{\sigma_{i+1}^{VM}}\left(\frac{\boldsymbol{\sigma}_{i}^{TOP} - \boldsymbol{\sigma}_{i}^{BOTTOM}}{2h} + \boldsymbol{L}\frac{(\boldsymbol{\varepsilon}_{i+1}^{TOP} - \boldsymbol{\varepsilon}_{i+1}^{BOTTOM}) - (\boldsymbol{\varepsilon}_{i}^{TOP} - \boldsymbol{\varepsilon}_{i}^{BOTTOM})}{2h}\right) \tag{D.7}$$

As can be seen, Equation D.7 is an accumulating function which is in-line with the change in strain gradient. The change in strain gradient is the bending deformation direction. However, this function is sensitive to the considered time-step, where a too large interval could result in big jumps in the von-mises stress requiring heavy returns to the yielding surface and thus non-representative stress gradients.

However, all of the above is based on a linear stress distribution as shown from the starting equation Equation 3.39. While for plastic deformation, the stress distribution is non-linear.